Investigation of a laser-driven neutron source with respect to different fields of application

Untersuchung der Einsetzbarkeit einer laserbasierten Neutronenquelle für verschiedene Anwendungsbereiche
Zur Erlangung des Grades eines Doktors der Naturwissenschaften (Dr. rer. nat.)
genehmigte Dissertation von M.Sc. Annika Kleinschmidt aus Erfurt
Tag der Einreichung: 16.05.2017, Tag der Prüfung: 10.07.2017
September 2017 — Darmstadt — D 17

1. Gutachten: Professor Dr. Markus Roth
2. Gutachten: Professor Dr. Oliver Boine-Frankenheim

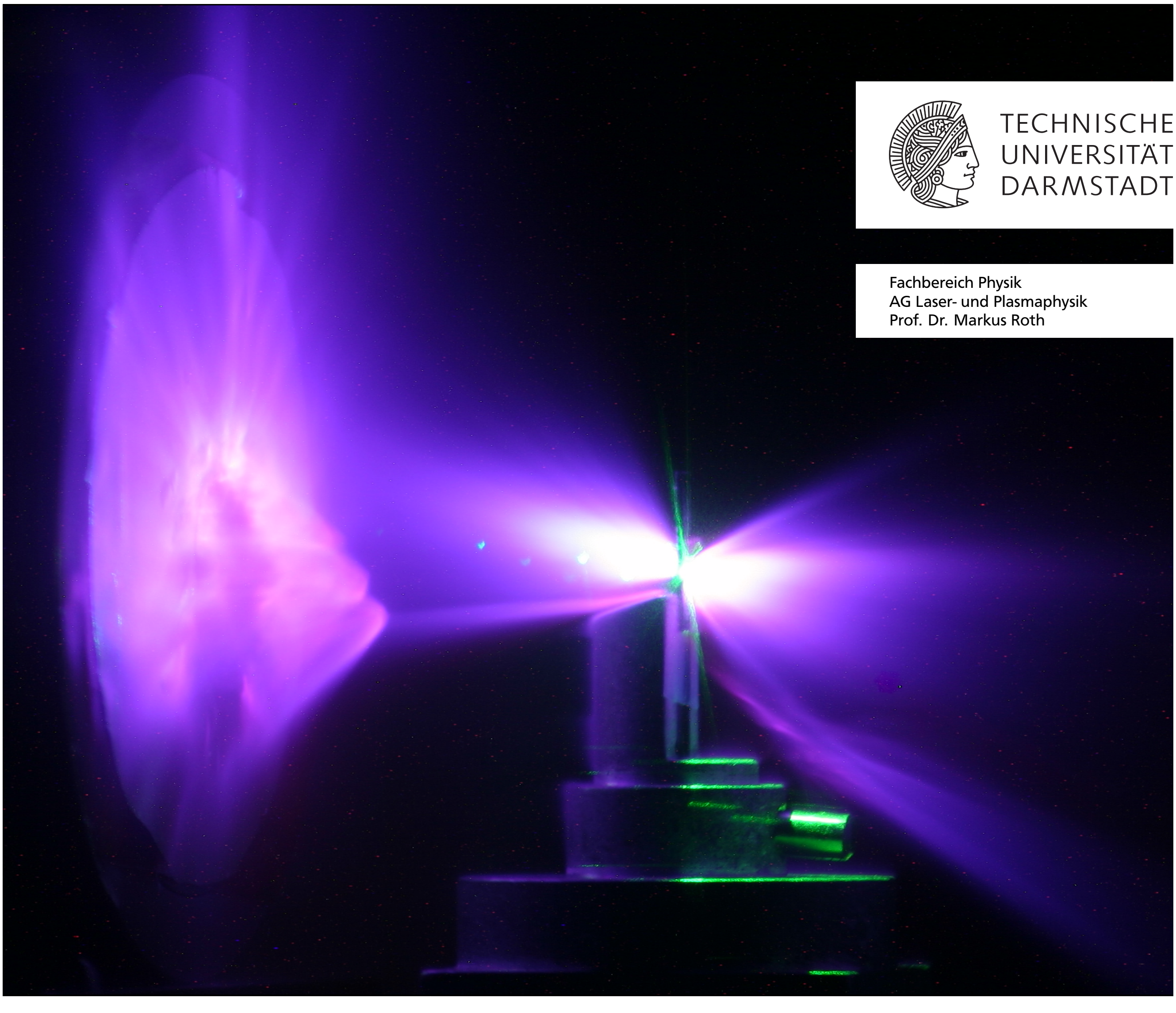

TECHNISCHE
UNIVERSITÄT
DARMSTADT

Fachbereich Physik
AG Laser- und Plasmaphysik
Prof. Dr. Markus Roth

Investigation of a laser-driven neutron source with respect to different fields of application
Untersuchung der Einsetzbarkeit einer laserbasierten Neutronenquelle für verschiedene Anwendungsbereiche

Genehmigte Dissertation von M.Sc. Annika Kleinschmidt aus Erfurt

1. Gutachten: Professor Dr. Markus Roth
2. Gutachten: Professor Dr. Oliver Boine-Frankenheim

Tag der Einreichung: 16.05.2017
Tag der Prüfung: 10.07.2017

Darmstadt — D 17

Erklärung zur Dissertation

Hiermit versichere ich, die vorliegende Dissertation ohne Hilfe Dritter nur mit den angegebenen Quellen und Hilfsmitteln angefertigt zu haben. Alle Stellen, die aus Quellen entnommen wurden, sind als solche kenntlich gemacht. Diese Arbeit hat in gleicher oder ähnlicher Form noch keiner Prüfungsbehörde vorgelegen.

Darmstadt, den September 1, 2017

(Annika Kleinschmidt)

Zusammenfassung

Die Wechselwirkung von Neutronen mit Materie weicht sehr stark von der geladener Teilchen ab, was sie für viele Einsatzgebiete im Bereich der Forschung und Industrie interessant macht. Um Neutronen für die unterschiedlichsten Anwendungen zur Verfügung zu stellen, müssen sie durch Kernreaktionen erzeugt werden. Dies kann zum Beispiel in beschleunigerbasierten Spallationsquellen oder in Kernreaktoren geschehen, wo sehr hohe Neutronenflüsse erreicht werden können.

Herkömmliche Neutronenquellen könnten in Zukunft durch eine neue Art der Neutronenerzeugung ergänzt werden. Diese beruht auf dem Prinzip der nuklearen Wechselwirkung laserbeschleunigter Ionen mit einem Konvertermaterial, einem sogenannten *Catcher*. Je nach Art der Wechselwirkung werden die Neutronen isotrop, oder mit einer Tendenz in die Propagationsrichtung der einfallenden Ionen (im Folgenden *Vorwärtsrichtung* genannt) abgestrahlt. Die Winkelverteilung der emittierten Neutronen ist demnach eine Überlagerung der isotropen Verteilung mit einem vorwärts gerichteten Neutronenstrahl.

Das Energiespektrum einer lasergetriebenen Neutronenquelle zeigt ein exponentiell abfallendes Verhalten mit Maximalenergien im Bereich von einigen 10 MeV bis hin zu über 100 MeV. Jedoch ist für einige Anwendungen ein erhöhter Neutronenfluss im epithermischen Energiebereich von etwa 0.1 eV bis 100 keV wünschenswert. Dazu gehört beispielsweise die Neutronenresonanzspektroskopie, da viele Elemente ausgeprägte Resonanzen bei diesen Energien aufweisen. Um das Energiespektrum einer laserbasierten Neutronenquelle für diese Anwendungen anzupassen, wird ein Zusatzmaterial eingesetzt, welches den hochenergetischen Teil des Spektrums moderieren und so den Neutronenfluss im epithermischen Bereich erhöhen soll.

Die vorgelegte wissenschaftliche Arbeit beschäftigt sich mit der Einsetzbarkeit einer lasergetriebenen Neutronenquelle bezüglich gebräuchlicher Anwendungen für Neutronen im hoch- und niederenergetischen Bereich. Zunächst wird die für Anwendungen unabdingbare Erzeugung konstant hoher Neutronenflüsse mit dieser Quelle untersucht. Dafür wird der Neutronenfluss in die Vorwärtsrichtung erhöht und die Gesamtzahl der Neutronen für mehrere Laserschüsse gemessen. Auf dieser Basis wird anschließend anhand einer statischen Indiumprobe die Anwendbarkeit der Neutronenquelle für Neutronenresonanzspektroskopie überprüft. Wie auch viele andere Elemente, besitzt Indium Resonanzen im epithermischen Energiebereich. Aus diesem Grund schließt die Studie, neben der eigentlichen Auswertung des Neutronenspektrums nach Durchlaufen der Indiumprobe, zunächst eine Moderierung des Neutronenspektrums und dessen Analyse mit ein.

Der Nachweis der Schuss-zu-Schuss Reproduzierbarkeit einer laserbasierten Neutronenquelle wurde am PHELIX Laser (engl. **P**etawatt **H**igh-**E**nergy **L**aser for Heavy **I**on E**X**periments) am GSI Helmholtzzentrum für Schwerionenforschung GmbH in Darmstadt durchgeführt. Der Laser wies eine Energie von 200 J, eine Pulslänge von 500 fs und eine Intensität im Bereich von 10^{20} W/cm^2 auf. Er wurde auf dünne Polymerfolien mit Dicken zwischen 400 und 1200 nm

fokussiert. Zur Neutronenerzeugung wurde ein Berylliumkonverter verwendet. Mit dieser Konfiguration konnte eine mittlere Gesamtneutronenzahl von $(5.25 \pm 0.77) \cdot 10^{10}$ Neutronen pro Laserschuss erzielt werden. Die räumliche Verteilung der Neutronen wurde mit bis zu 30 speziellen Neutronendosimetern (sogenannten *Bubbledetektoren*) gleichzeitig vermessen, um eine hohe Auflösung zu erreichen. Das Ergebnis dieser Messungen zeigt einen gerichteten Neutronenstrahl in die Vorwärtsrichtung, der einen Öffnungswinkel von $(100 \pm 2)^\circ$ aufweist. Die höchste gemessene Neutronenzahl in Vorwärtsrichtung beträgt $(1.42 \pm 0.25) \cdot 10^{10}$ Neutronen pro Steradiant, was einen Anstieg von 40 % gegenüber dem höchsten bisher publizierten Wert darstellt.

Der zweite Schwerpunkt dieser Arbeit liegt auf der Moderierung des Energiespektrums einer lasergetriebenen Neutronenquelle und dessen anschließender Anwendung für Neutronenresonanzspektroskopie an einer Indiumprobe. Das zugehörige Experiment wurde an der Trident laser facility am Los Alamos National Laboratory (LANL) in den USA durchgeführt. Die Kurzpulskonfiguration dieses Systems bietet eine maximale Laserenergie von 80 J auf dem Target und eine Pulslänge von 500 fs mit einer Intensität von 10^{20} W/cm^2. Für die Beschleunigung der Ionen wurden dünne Polymerfolien verwendet, deren Dicken im Bereich von einigen 100 nm lagen. Der Konverter war in einen Block aus hochdichtem Polyethylen eingelassen, der als Moderator eingesetzt wurde. Zur Detektion des Neutronenspektrums wurde eine mit Bor dotierte Mikrokanalplatte (engl. microchannel plate, MCP) eingesetzt. Nach erfolgreicher Moderierung der Neutronen, die im Bereich der Indiumresonanz einen Faktor 3 höhere Neutronenzahlen ergab, wurde eine Indiumprobe direkt vor der MCP platziert. Das Ergebnis der Vermessung des Transmissionsspektrums bei einem einzelnen Laserschuss zeigt eine Resonanz mit einer Energie von (1.61 ± 0.19) eV und einer Breite von (0.25 ± 0.16) eV. Diese Werte stimmen sehr gut mit denen der Indiumresonanz bei 1.46 eV überein.

Im Rahmen der vorgelegten Arbeit wird gezeigt, dass eine laserbasierte Neutronenquelle dem Anspruch konstant hoher Neutronenflüsse genügt, was maßgeblich für aussagekräftige und verlässliche Messungen in verschiedenen Anwendungen ist. Außerdem kann erstmalig die erfolgreiche Moderierung des Energiespektrums und die Einsetzbarkeit einer lasergetriebenen Neutronenquelle für Resonanzspektroskopiemessungen an statischen Objekten verifiziert werden.

Abstract

Due to their unique interaction with matter, neutrons are an interesting research and diagnostic instrument for various applications. To be able to utilize neutrons for the different applications, they have to be generated by nuclear reactions. This can for instance be done in accelerator-based spallation sources or fission reactors, which provide the possibility of generating high-flux neutron beams. However, they could be complemented by a novel and compact neutron source which is based on the conversion of laser-accelerated ions into neutrons inside a converter material, a so-called *catcher*. The angular distribution of the emitted neutrons is a superposition of an isotropic emission from generated compound nuclei in the catcher material and a forward directed neutron beam originating from special reactions such as pre-equilibrium emission and deuteron break-up.

Neutrons from a laser-driven neutron source show an exponentially decaying energy spectrum with cut-off energies in the range of a few 10 MeV up to over 100 MeV. Nevertheless, for applications such as *neutron resonance spectroscopy* (NRS), neutrons in the epithermal energy range (0.1 eV - 100 keV) are preferable because many nuclei have distinct resonances in this regime. To maximize the neutron yield at epithermal energies, a moderating material is used to slow down the high-energy component of the neutron spectrum.

The presented scientific thesis will focus on the applicability of a laser-based neutron source regarding established neutron applications in the high- and low-energy regime. In a first step, the for applications indispensable reproducability of such a source will be investigated. For that purpose, the neutron yield in the direction of the incoming ion's flight path (henceforth called *forward direction*) will be increased and the total neutron yield will be measured for several shots. In a second step, the applicability of a laser-driven neutron source for neutron resonance spectroscopy on a static sample will be studied. As many elements have resonances in the epithermal region, the emitted neutron spectrum has to be moderated to increase the neutron flux in the desired energy range. Therefore, the study includes the analysis of the moderated neutron spectrum itself and its alteration after the NRS sample.

The verification of reproducable neutron numbers and a detailed measurement of the angular distribution were conducted at the PHELIX laser (**P**etawatt **H**igh-**E**nergy **L**aser for Heavy **I**on E**X**periments) at GSI Helmholtzzentrum für Schwerionenforschung GmbH in Darmstadt, Germany. The 200 J and 500 fs short-pulse laser beam was focused onto thin deuterated polymer foils with thicknesses between 400 and 1200 nm. During the experiment, intensities of the order of 10^{20} W/cm^2 on target were achieved. The accelerated ions impinged a beryllium catcher yielding mean maximum neutron numbers of $(5.25 \pm 0.77) \cdot 10^{10}$ per shot. For a detailed measurement of the angular distribution, up to 30 bubble neutron dosimeters were used simultaneously. The result shows a forward pointing neutron beam with an opening angle of $(100 \pm 2)^\circ$ at full width half maximum. The highest measured neutron yield in the forward direction was $(1.42 \pm 0.25) \cdot 10^{10}$ neutrons per steradian which is an increase of 40 % compared to the highest reported neutron numbers so far.

The second key aspect of this thesis is the moderation of laser-driven neutrons and their subsequent application for a neutron resonance spectroscopy measurement on a static sample. This experiment was conducted at the Trident laser facility at Los Alamos National Laboratory (LANL), USA. The short-pulse configuration provides a maximum laser energy of 80 J on target within a pulse length of 500 fs, yielding maximum intensities above 10^{20} W/cm^2. Ions were accelerated from thin polymer foils with thicknesses in the range of a few 100 nm. The catcher was surrounded by a block of high density polyethylene to slow down high-energy neutrons and thus maximize the epithermal yield. This could successfully be achieved by an increase of a factor 3 more neutrons in the energy range of the indium resonance compared to shots without a moderator.

For the NRS measurement, a 5 mm indium sample was placed directly in front of the boron-doped microchannel plate (MCP) detector, which was used to measure the time of flight (ToF) transmission spectrum of the sample. The result of a single shot measurement shows a distinct resonance with a central energy of (1.61 ± 0.19) eV and a width of (0.25 ± 0.16) eV. These values are in good agreement with those of the indium resonance at 1.46 eV. During this experiment, we could sucessfully demonstrate a single shot neutron resonance spectroscopy measurement on a static sample.

In summary, in the framework of the presented thesis it will be demonstrated, that a laser-driven neutron source satisfies the requirement of constantly high neutron fluxes, which is very important for significant and reliable measurements during applications. In addition, the effective moderation and the feasibility of laser-driven neutrons for neutron resonance spectroscopy on a static sample will be confirmed for the first time.

Contents

1 Introduction

The interaction of neutrons with matter is highly different from that of charged particles or electromagnetic waves. This enables complementary measurements of matter and provides an insight into the structure of materials and objects from a new perspective. As neutrons penetrate matter easily and have rather week interactions with high-Z solids, it is possible to probe the bulk of a sample material, even if it is stored in an environment inaccessible to other diagnostics, for example in a container or behind massive shielding. These unique interaction properties are especially useful in the field of fusion research, where the fuel, consisting of light elements such as deuterium or tritium, is embedded in a capsule consiting of a heavier element (e.g. [1]). Neutrons provide an in-situ measurement of the fuel conditions. Other applications for neutrons reach from various fields in physics research [2, 3], to material science [4, 5], biology [6] and medical sciences [7, 8] to archeology [9, 10].

Conventional neutron sources are for example large reactors based on fission processes [11, 12] or accelerator-based spallation sources [13–15]. Fission reactors isotropically emit neutrons with energies around 2 MeV and provide peak fluxes of the order of $10^{15}\,\mathrm{cm^{-2}s^{-1}}$. Accelerator-based spallation sources provide the highest fluxes of the order of $10^{16}\,\mathrm{cm^{-2}s^{-1}}$ with neutron energies up to several 100 MeV. In addition, they emit pulsed neutron bunches in the microsecond regime down to several 100 ns, which not only allows measurements of static objects, but also of quickly changing processes in a material.

A very promising alternative to conventionally used neutron sources has gradually become more important during the last 15 years. Laser-driven neutron sources are based on the conversion of laser-accelerated ions into neutrons via nuclear reactions inside a secondary target. With the development of high-intensity short-pulse lasers in the last decades, it is now possible to accelerate ions from thin target foils or gas jets to energies ranging from several MeV/u [16–18] up to several 10 MeV/u [19–22] depending on the acceleration mechanism and the ion species. The most investigated laser-acceleration mechanism is *Target Normal Sheath Acceleration* (TNSA) [19,23]. During the interaction of a high-intensity laser with a solid material, the laser heats electrons at the surface and accelerates them into the target. They propagate through the target into the vacuum and form a sheath on the rear surface. Ions get accelerated by the generated electrostatic field. Another possibility is the acceleration in the *relativistic transparency regime* [24], where at some point the laser can propagate into the target and thus interacts with the whole target volume. As a result, in contrast to TNSA, ions are accelerated from the bulk material.

For neutron generation, the accelerated ions impinge a secondary target and excite the nuclei of the material, which in turn emit neutrons and other particles or radiation. These novel laser-based neutron sources provide high peak fluxes, short pulses below one nanosecond [25], and a compact design compared to fission reactors or accelerator-based spallation sources. The pulse length of the neutron bunch allows the visualization of processes on very short time scales. The size of the source is determined by the dimensions of the laser system, which in the future could enable the possibility to transport such a neutron source. This opportunity would greatly expand the field of applications. Regarding these properties, laser-driven neutron sources could complement common accelerator-based spallation sources or fission reactors.

One of the applications in which epithermal neutrons are required is *neutron resonance spectroscopy*. This technique is based on the resonance structure of neutron capture and scattering reactions, which is unique for every element and allows the identification of materials and their elemental composition [26]. Many isotopes have pronounced resonances in the epithermal regime, which requires a high neutron flux at these energies.

Laser-driven neutron sources provide an exponentially decaying energy spectrum with cut-off energies from several 10 MeV [27] up to more than 100 MeV [25]. To adapt this spectrum to applications where thermal or epithermal energies are advantageous, the neutrons have to be moderated in a suitable material. Such a material should possess a high possibility to scatter neutrons, but at the same time have a low possibility for neutron capture reactions. Common materials used as moderators are hydrogen, deuterium, and carbon [28].

In the framework of this thesis, the capability of a laser-driven neutron source for different high- as well as low-energy neutron applications will be investigated and optimized.

1.1 Thesis structure

The requirements that have to be fulfilled for applications of a laser-based neutron source are the reproducability of the generated neutrons as well as a high neutron yield in the energy range needed for the specific application. The focus of the present thesis will be the moderation of the high-energy component of the neutron spectrum and the experimental verification of the feasibility of laser-driven epithermal neutrons for resonance spectroscopy.

The following chapter will give an overview of the interaction of high-intensity short-pulse lasers with a solid target material, starting from the first interactions at early times and ending with different ion acceleration schemes. The first section will give a brief description of the behaviour of a single particle in the presence of a laser field, including a first approach to treat this interaction with a realistic spatial laser profile. The laser-generated plasma on the target surface and its influence on the laser are described in section 2.2. The following sections introduce different schemes of relativistic electron generation due to the laser and two different ion acceleration mechanisms.

Chapter 3 describes the generation of laser-driven neutrons. Each step of the generation chain is introduced seperately. The material of the target, from which ions get accelerated by the laser, and the neutron converter as well as the nuclear reactions are discussed in sections 3.1 to 3.3. Afterwards, the state of the art of laser-driven neutron sources up to the year 2014 and a comparison to conventional sources are following. The last section of this chapter gives a short insight into the theory of neutron moderation and neutron resonance spectroscopy.

The difficulties of neutron detection will be introduced in the fourth chapter. It will discuss primary neutron reactions in a converter material and their cross sections. In addition, different types of passive and active detectors and their behaviour in the environment of a laser-driven neutron source will be presented.

The last two chapters will describe the conducted experiments at the PHELIX laser [29] at GSI Helmholtzzentrum für Schwerionenforschung GmbH in Darmstadt, Germany, and the Trident laser facility at Los Alamos National Laboratory in New Mexico, USA. The experiment on the PHELIX laser was dedicated to the maximization of the total neutron yield and the reproducability of a laser-driven neutron source. Furthermore, a detailed study of the angular neutron distribution was carried out. The results of this campaign are presented in section 5.2. During the experimental campaigns at the Trident laser described in chapter 6, the key aspect was to moderate the emitted neutrons and to verify their applicability for neutron resonance spectroscopy. Achievements and conclusions resulting from these experiments are presented in section 6.2.1.

A comprehensive summary and final remarks will be given in chapter 7 followed by future prospects in chapter 8. The latter includes different aspects from the optimization for high-energy neutron applications to improvements on laser-based neutron resonance spectroscopy and future experiments as well as detector development.

2 Interaction of high-intensity short-pulse lasers with matter

Ever since the method of *chirped pulse amplification* [30] (CPA) was introduced by Strickland and Mourou in 1985, it has been possible to amplify short laser pulses with pulse lengths below 1 ps to energies of a few 100 J. This enables laser intensities of $10^{18}\,\mathrm{W/cm^2}$ and more, which is sufficient to accelerate ions from thin target foils.

When a high-intensity short-pulse laser interacts with a solid material, it starts to ionize the atoms at the surface. One possible ionization mechanism is *multiphoton ionization* [31] inside the laser field, which starts to become important at laser intensities above $10^{12}\,\mathrm{W/cm^2}$. During this non-linear process, two or more photons are absorbed simultaneously. Another mechanism called *avalanche ionization* is dominant at laser intensities between 10^9 and $10^{12}\,\mathrm{W/cm^2}$ [31]. As this process is based on collisions between electrons, the material needs to provide free electrons for this mechanism to occur. The question on how the first electron is generated in a non-metal, such as a polymere, is still topic to current research. One explanation is the existence of defects inside the material leading to loosely bound or unbound electrons that are able to further ionize the material by collisions. Thermal excitation due to the heating of the laser is another process that can provide free electrons.

The following chapter considers the interaction of laser pulses with matter. Due to the above mentioned ionization of the material, unbound electrons start to interact with the laser. Section 2.1 discusses the motion of a single particle in a laser field. During the interaction of the laser with the material, the rapid ionization leads to the expansion of a plasma from the target surface into the vacuum. General properties of laser propagation in a plasma and important parameters of the plasma state are described in section 2.2. The following sections cover the acceleration of particles by the laser starting from electron heating processes inside a solid target in section 2.3. Afterwards, two different laser-ion acceleration mechanisms are introduced in section 2.4.

2.1 Single particle motion in a laser field

The interaction of an electromagnetic field with a single particle can be described by the Lorentz force given by the equation of motion

$$\vec{F}_\mathrm{L} = m\frac{\mathrm{d}\vec{v}}{\mathrm{d}t} = q\left(\vec{E} + \vec{v} \times \vec{B}\right) \tag{2.1}$$

with mass m, velocity $\vec{v}$, and charge q of the particle as well as the electric and magnetic fields $\vec{E}$ and $\vec{B}$.

In the non-relativistic case, the influence of the magnetic field can be neglected. The interaction with a homogeneous and slowly varying electric field $\vec{E} = \vec{E}_0 \cos(\omega t)$, where $\vec{E}_0$ represents the amplitude and ω the laser frequency, leads to an oscillation with the quiver velocity [32]

$$v_{\mathrm{os}} = \frac{qE_0}{m\omega}. \tag{2.2}$$

However, laser pulses, especially when they have high intensities above 10^{18} W/cm^2 and ultrashort pulse length in the picosecond regime, do not fulfill the condition of homogeneous and slowly varying fields. Focusing down the laser to several micrometer in diameter causes strong radial intensity gradients over the spatial pulse profile. In addition, ultrashort few-cycle pulses are highly dispersive and can not be treated adiabatically [32]. The following part presents one possibility to treat the first of these cases in a more realistic way.

Considered is the effect of a non-uniform laser profile on an electron. The intensity of a laser is given by $I = 1/2c\varepsilon_0 \left|\vec{E}\right|^2$ [33] with the speed of light c and the vacuum permittivity ε_0. An intensity gradient can be introduced by a radial slowly varying electric field that is assumed to be y-directed: $E_{\mathrm{y}}\left(\vec{r}\right) = E(y)\cos\phi$ with $\phi = \omega t - kx$, where k represents the wave number. In the non-relativistic case, where $v/c \ll 1$ is valid, the equation of motion (2.1) reduces to

$$\frac{\partial v_{\mathrm{y}}}{\partial t} = -\frac{e}{m_{\mathrm{e}}} E_{\mathrm{y}}(\vec{r}) \tag{2.3}$$

with the electron mass m_{e} and charge e.

A Taylor expansion of the above given electric field and a subsequent cycle average yield to the *ponderomotive force*

$$F_{\mathrm{P}} = -\frac{e^2}{4m_{\mathrm{e}}\omega^2}\frac{\partial E_0^2}{\partial y}. \tag{2.4}$$

This expression shows, that an electron in an area of high intensity will be pushed to areas with lower intensity. Thus, considering a Gaussian shaped laser focus on target, the ponderomotive force expels electrons from the focal spot. The effect gets stronger with increasing intensity gradient.

The fully relativistic equation of the ponderomotive force has been obtained by Bauer *et al.* [34] and is given by

$$\vec{F}_{\mathrm{p}} = -\frac{c^2}{\gamma}\left(\vec{\nabla} m_{\mathrm{eff}} + \frac{\gamma - 1}{v_0^2}\left(\vec{v}_0 \cdot \vec{\nabla} m_{\mathrm{eff}}\right)\vec{v}_0\right), \tag{2.5}$$

where m_{eff} represents a space and time dependent effective mass and $\gamma = \left(1 - v_0^2/c^2\right)^{-1/2}$ the relativistic gamma factor. At relativistic intensities, the electron not only gets pushed away from the laser axis, but also experiences a drift in the laser forward direction as it is displayed in Figure 2.1 [32]. The emission angle can be derived to $\cos\theta = \sqrt{(\gamma - 1)/(\gamma + 1)}$.

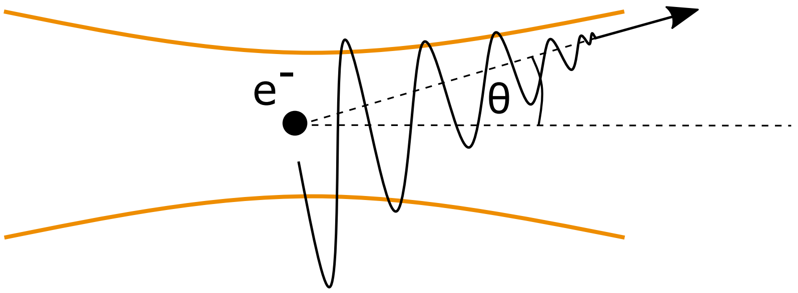

Figure 2.1.: Electron motion in a finite laser focus due to the relativistic ponderomotive force. Adapted from [32].

2.2 Laser propagation in a plasma

A plasma is defined as a partially or fully ionized quasineutral gas of unbound charged and uncharged particles that show collective behavior [35, 36]. On a global scale the plasma is neutral, which is expressed by equal particle densities of ions n_i and electrons: $n_\mathrm{e} \approx \sum_j Z_j \cdot n_{i,j}$, where j labels different ion species. Nevertheless, as the particles of a plasma move, they generate local accumulation of charges, which results in the build-up of electric potentials. The ability to reduce the thus generated electric field is represented by the Debye potential with the characteristic Debye length

$$\lambda_\mathrm{D} = \sqrt{\frac{\varepsilon_0 k_\mathrm{B} T_\mathrm{e}}{n_\mathrm{e} e^2}}, \tag{2.6}$$

where k_B represents the Boltzmann constant and T_e the electron temperature. An equivalent expression can also be obtained for the ions. To ensure the characteristic of quasi-neutrality, the plasma density scale length defined as $L = n_e/|\nabla n_e|$ [33] has to be much larger than the Debye length $L \gg \lambda_\mathrm{D}$ [35, 36].

As a result, the interactions between the particles are described by a Coulomb potential that is screened by the Debye potential [33]

$$\Phi(r) = \frac{q}{4\pi\varepsilon_0 r} \exp\left(-\frac{r}{\lambda_\mathrm{D}}\right) \tag{2.7}$$

with distance r. In comparison to the van der Waals force, which is dominant in neutral gases and decreasing with $1/r^6$, the dependency of (2.7) proportional to $\exp(-r)/r$ represents a long-range screened Coulomb force, that not only effects particle motion on local scales, but results in a collective behavior of the plasma state. This also enables the response of a plasma to an external perturbation, like an electromagnetic or an electrostatic field, to be described by collective behavior. If the perturbation represented by the potential Φ_{per} is small compared to the thermal energy of the plasma $|e\Phi_{per}| \ll k_\mathrm{B}T$, the electron energy is only slightly changed and the movement of the ions can be neglected. The response time is thus given by $\tau \approx \lambda_\mathrm{D}/v_\mathrm{e}$

with the thermal electron velocity $v_\mathrm{e} \approx (k_\mathrm{B}T_\mathrm{e}/m_\mathrm{e})^{1/2}$. The reciprocal of the response time defines the plasma frequency

$$\omega_\mathrm{P} = \sqrt{\frac{n_\mathrm{e}e^2}{\varepsilon_0 m_\mathrm{e}}}. \tag{2.8}$$

In the following, the perturbations are assumed to originate from a laser field that interacts with the plasma. In this case, the dispersion relation can be written as $\omega^2 = \omega_\mathrm{P}^2 + c^2|\vec{k}|^2$. First assumptions on how a laser propagates in a plasma can be made by closer consideration of this equation. The interaction of a laser with a frequency $\omega > \omega_\mathrm{P}$ with a plasma results in a real wave vector $\vec{k}$. In this case, the plasma is transparent to the laser. The latter can propagate into the plasma, which is then called *underdense*. If the laser frequency equals the plasma frequency $\omega = \omega_\mathrm{P}$, the wave vector equals zero, hence, the laser is not able to propagate further into the plasma than to a certain density, the so-called *critical density*

$$n_\mathrm{c} = \frac{\varepsilon_0 m_\mathrm{e}\omega^2}{e^2} \tag{2.9}$$

derived from (2.8) under the given condition.

In the remaining case, where the laser frequency is smaller than the plasma frequency $\omega < \omega_\mathrm{P}$, the wave vector reaches imaginary values. Under this condition the critical density is lower than the electron density $n_\mathrm{c} < n_\mathrm{e}$ and the plasma is called *overdense*. Because the spatial dependence of the laser field contains the term $\mathrm{e}^{\mathrm{i}\vec{k}\vec{x}}$, imaginary wave vectors $\vec{k}$ lead to an exponential attenuation of the field inside the plasma [36]. As a result, the laser can penetrate the plasma to a specific skin depth δ, which can be expressed as $\delta = |\vec{k}|^{-1}$:

$$\delta = \frac{c}{\sqrt{\omega_\mathrm{P}^2 - \omega^2}}. \tag{2.10}$$

In the case of relativistic electrons inside the plasma, the plasma frequency in equation (2.8) can decrease to values below the laser freuquency due to the relativistic mass increase. In this case, the plasma stays classically overdense, but becomes *relativistically transparent* to the laser. This effect is discussed in detail in section 2.4.2.

2.3 Electron acceleration in solid targets

When a laser is focused on the surface of a solid target in vacuum, a part of its energy is transferred to the material which is subsequently heated. From intensities above $10^9\,\mathrm{W/cm^2}$ [31], this leads to rapid ionization of the atoms in the interaction region and gives rise to an expanding plasma from the target with an initial density much higher than the critical density. As a result, this plasma is opaque to the laser (see section 2.2). There are a variety of absorption and heating mechanisms depending on the laser intensity, pulse length, and focus profile as well as the density gradient of the target surface or the expanding plasma, respectively. Due to the complexity of the influence of these parameters, electron heating in solid materials is far from being fully understood and therefore is still subject to current research.

The following section will focus on absorption mechanisms at high intensities above $10^{15}\,\mathrm{W/cm^2}$ and short pulses on a sub-picosecond time scale. As a first approach, the ions can be assumed to be fixed because the oscillation period of the laser is too short for them to react to the electromagnetic field. However, they are still influenced by the rapid displacement of the electrons due to the ponderomotive force (2.5) [32] or other electron acceleration mechanisms.

For smaller intensities below $10^{16}\,\mathrm{W/cm^2}$ and long pulses in the nanosecond regime collisional absorption, such as inverse bremsstrahlung, is the dominant process for laser-target interactions [32, 33, 37]. However, its importance gets smaller when reaching higher intensities and shorter pulses. In this case the plasma temperature due to heating from the laser rises fast enough for collisions to become ineffective during the interaction [38] because of the rapid decrease of the electron-ion collision frequency with temperature $\nu_{ei} \propto T^{-3/2}$ [35]. Absorption is then determined by collective behavior, for instance the conversion of laser energy into plasma waves that heat the electrons. These collisionless absorption mechanisms are based on absorption as a result of driving electron oscillations along a density gradient [39]. There are multiple propositions that were studied theoretically as well as experimentally during the last decades [40–51]. However, laser absorption in a plasma and coupling to the electrons remains a topic of research because of the complex processes taking place during the interaction between the laser, the electrons, and the ions.

In the non-relativistic case (intensities below $10^{18}\,\mathrm{W/cm^2}$ [33]) and assuming small density gradients, *resonance absorption* [52] seems to be the dominant process. In this scenario a p-polarized laser with an incident angle larger than $0\,^{\circ}$ to the normal of the critical surface stimulates an electron plasma wave at the critical density, which is resonantly amplified over a few laser cycles and afterwards damped by wave breaking [32], generating relativistic electrons.

However, the absorption mechanism changes when it comes to steep density profiles where the scale length L of the plasma is of the order of the laser wavelength λ. In this case, the electrons near the critical surface interact directly with the laser field and get pulled out into the vacuum during the first half of the laser cycle [38, 53]. In the second half of the laser cycle, the field is reversed and the electrons get pushed back into the target behind the critical density in an overdense region of the plasma. Because the laser can only penetrate to a certain skin depth given in (2.10), the electron is out of the interaction region and can propagate further into the plasma undisturbed by the electric field of the laser. During this process, which was

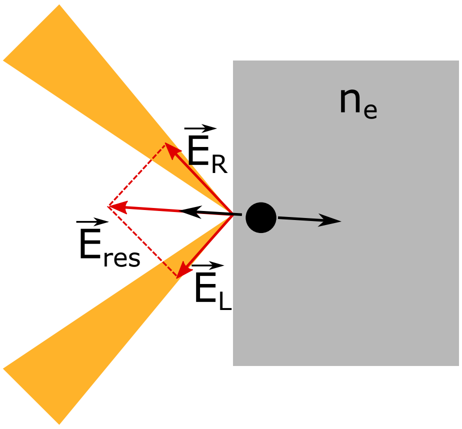

Figure 2.2.: Electron acceleration at the critical density at high intensities. During the first half of the laser cycle, electrons are pulled out of the overdense target. When the laser field reverses during the second half of the cycle, the electron gets accelerated back into the overdense region of the material.

first introduced by F. Brunel [54] as *not so resonant, resonant absorption*, conversion efficiencies from laser energy into hot electrons of more than 70 % are possible [38]. The electrons can be accelerated to energies of several MeV [53], especially when the electron undergoes several oscillation periods before returning into the plasma [44]. In this case, the mechanism has to be treated relativistically, which requires a relativistic expression of the critical density

$$n_{\mathrm{C,rel}} \approx n_{\mathrm{C}} \sqrt{1 + \frac{I\lambda^2}{f \cdot 10^{18}\,\mathrm{W/cm^2 \mu m^2}}} \tag{2.11}$$

with the non-relativistic critical density n_{C} from equation (2.9), that can be written as $n_{\mathrm{C}} \approx 1.1 \cdot 10^{21}\,(\lambda/\mu\mathrm{m})^{-2}\,\mathrm{cm}^{-3}$ [37], and f a factor between 1 and 3 introduced by J. R. Davies [39] as a solution to the non-ideal polarization of the laser that is influencing the electron mass distribution and thus the electron density in the plasma.

At even higher intensities above $10^{18}\,\mathrm{W/cm^2}$ another absorption mechanism called *jxB heating* [42, 55–57] starts to become more important. In this intensity regime the magnetic component of the laser field, and thus the magnetic term of the Lorentz force in (2.1), is no longer negligible. The oscillating ponderomotive force in equation (2.4), defined by an oscillating electric field, together with the magnetic field induce a $\vec{v} \times \vec{B}$ term, which accelerates the electrons into the overdense region of the plasma, resulting in a kinetic energy given by the ponderomotive potential $\Phi_{\mathrm{P}} = -1/q \int \vec{F}_P \mathrm{d}\vec{r}$ with $\vec{F}_P$ given in equation (2.5). Simulations done by Wilks *et al.* [55] considering a Gaussian pulse profile with a peak intensity of $I\lambda^2 = 1.2 \cdot 10^{19}\,\mathrm{W\mu m^2/cm^2}$ have shown a conversion efficiency of 50 % into hot electrons for p-polarization. Furthermore, in comparison to resonance absorption or the Brunel mechanism, jxB heating is not restricted to a p-polarized laser because of the presence of a perpendicular magnatic field. Simulations for a s-polarized field resulted in a conversion efficiency of about 30% [55].

Through interaction of the relativistic electrons with the ions, these can gain energy and get accelerated. The following section will concentrate on two different ion acceleration mechanisms.

2.4 Ion acceleration in solid targets

When considering laser-ion acceleration, it is important to note that lasers nowadays are not able to transfer energy directly to the ions and accelerate them to relativistic energies because the ions are too heavy to couple to the laser field. Considering the ion quiver velocity $v_{\mathrm{i,os}}$ (cf. equation (2.2)), it is possible to estimate the laser intensity which would be needed for direct laser-ion acceleration:

$$\frac{v_{\mathrm{i,os}}}{c} = \frac{ZeE}{m_{\mathrm{i}}\omega c} = \frac{Zm_{\mathrm{e}}a_0}{m_{\mathrm{i}}}, \tag{2.12}$$

where m_{i} represents the ion mass, Z the atomic number, and a_0 the normalized field amplitude of the laser [58]

$$a_0 = \frac{v_{\mathrm{e,os}}}{c} = 0.85 \cdot \sqrt{\frac{I\,[\mathrm{W/cm^2}]\,\lambda^2\,[\mu\mathrm{m}^2]}{10^{18}}} \tag{2.13}$$

with $v_{\mathrm{e,os}}$ equivalent to equation (2.2), the laser intensity I, and the laser wavelength λ. To accelerate ions to relativistic energies $v_{\mathrm{i,os}}/c \approx 1$, a_0 would take values of the order of 10^3 corresponding to intensities above 10^{24} W/cm^2. Currently operating laser systems provide maximum intensities between 10^{21} and 10^{22} W/cm^2 [59].

Energy from the laser can only be transferred indirectly to the ions by coupling to the electrons. In the intensity regime above 10^{18} W/cm^2, the fields generated by the rapid collective displacement of the electrons due to the laser incidence are well above 1 GVm^{-1} [32] and thus strong enough to induce a collective ion motion. As a result, the ions can be accelerated to energies of several MeV/u to tens of MeV/u depending on the acceleration mechanism and the ion species.

The detailed processes behind the coupling of electrons and ions are still not fully understood, not only because of the complex physics behind these acceleration mechanisms, but also because of the variety of influencing parameters like target material and thickness as well as laser pulse length, intensity, polarization, and contrast. The following sections require a basic knowledge of the pulse shape of a realistic laser pulse as it is generated in high-energy laser systems. For a short introduction to that topic, the reader is referred to the appendix of this thesis.

2.4.1 Target normal sheath acceleration

Early experiments on laser-ion acceleration from solid targets [60–63] showed maximum ion energies in the keV range up to 1.5 MeV, for example explained by acceleration due to the ponderomotive force [60] or from the target front side due to $\vec{j}\times\vec{B}$ accelerated electrons pulling the ions out of the target [63]. In 2000, Snavely *et al.* [19] reported an ion maximum energy of 58 MeV which is well above everything known before. This new and more efficient acceleration

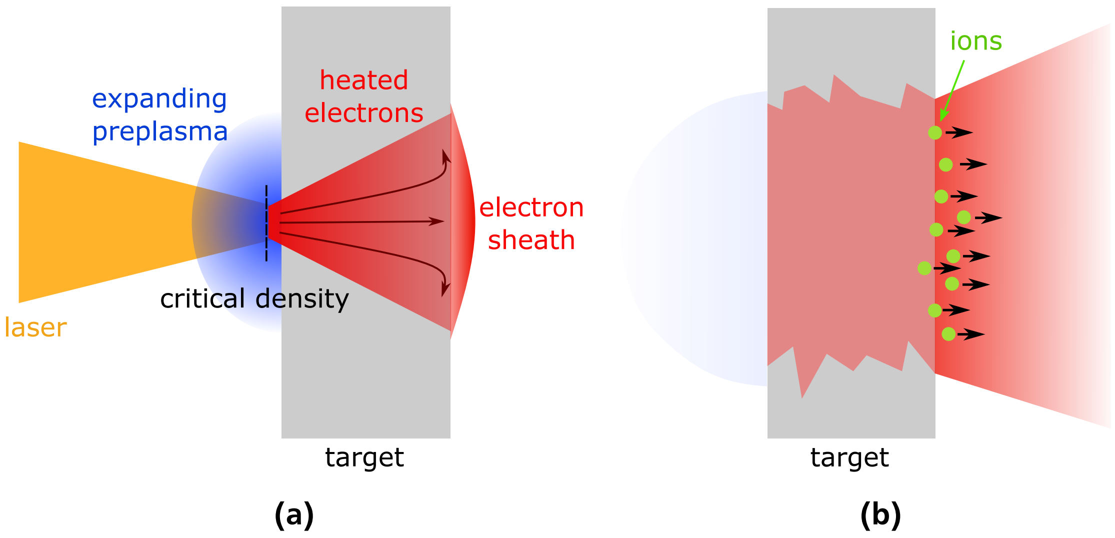

Figure 2.3.: Scheme of the TNSA mechanism. (a) The main pulse of the laser accelerates electrons in the region of the critical density. They propagate through the target and build up a sheath at the rear surface, which causes an electrostatic field. (b) This field ionizes the atoms at the target rear side, which subsequently get accelerated.

mechanism is called *target normal sheath acceleration (TNSA)* and proved to be able to accelerate protons from polymer targets to energies of more than 85 MeV [20].

The principle of the TNSA mechanism was introduced theoretically by Wilks *et al.* [23] and is schematically shown in Figure 2.3. The laser is focused on the surface of a solid target with typical thicknesses between 1 and 100 µm. The prepulse ionizes the target front side, causing a plasma to expand spherically in the direction of the incoming laser into the vacuum. This generates a shock wave to propagate into the material to the target rear side.

When the main pulse arrives at the target front side, the laser partly penetrates the underdense regions of the expanding preplasma until it gets reflected at the critical density. There, a part of the laser energy is transferred to the electrons via various absorption mechanisms depending on laser intensity, pulse length, and polarization as introduced in section 2.3. The electrons are heated to relativistic energies and accelerated through the target to the rear surface. A return current consisting of *cold* electrons compensates the rapid motion of relativistic electrons [64, 65]. At the target rear side, the latter propagate into the vacuum and build up a Debye sheath. This induces an electrostatic field of the order of $\mathrm{TV\,m^{-1}}$ [19] that ionizes the atoms at the rear surface. The thereby generated ions are accelerated in the electric field and pulled out of the target. Ions at the surface of the target are accelerated most efficiently because they reduce the electric field for ions which are not directly located at the surface but deeper inside the target. The acceleration drops as the ions catch up with the electrons. The result is a target normal directed beam of electrons and ions expanding into the vacuum.

The acceleration can be lessened, if the shock wave, which is generated at the beginning of the laser-matter interaction, is fast enough to propagate through the target to the rear side and perturbs the electrostatic field [66, 67]. In addition, a large prepulse of the laser could create a plasma at the rear side of very thin targets and thus reduce the accelerating field.

The dominant ion species accelerated with the TNSA mechanism is protons. This can be explained by two reasons: First, the target rear surface basically consists of hydrogen, carbon, nitrogen, and oxygen regardless of the main target material. This is due to the fact, that materials stored or handled under atmosphere will eventually get contaminated, which leads to layers of hydrocarbon and other atmospheric components adding to the target surfaces. As TNSA only accelerates the surface regions of the target, this mainly leads to acceleration of the contamination layer. Second, protons are the ions with the highest charge to mass ratio $q/m = 1$ with $e = 1$ and m in units of u. Compared to other ion species, this leads to the most efficient acceleration. Typical conversion efficiencies from laser energy into proton energy are of the order of a few percent [19, 68]. The conversion efficiency into heavier ions is two orders of magnitude less [21]. Typical maximum energies for heavier ions are in the range of a few MeV/u [16–18].

Ions accelerated through the TNSA mechanism show an exponentially decaying energy spectrum [19, 68] with sharp cut-off energies in the range of several 10 MeV. The beam consisting of electrons and ions is highly divergent. Ions with higher energy are located near the target normal, whereas ions with lower energies were found to be off-axis with a higher divergence. This results in a conoidally distributed ion beam around the target normal [19, 69].

A recently conducted experiment at the PHELIX laser [20] has shown, that the maximum ion energy from polymer targets between 500 and 1200 nm obtained with the TNSA mechanism is constant over a target thickness range of a few 100 nm. Nevertheless, early experiments on the topic of target thickness scan [70, 71] and recent simulations [20] indicate a rapid increase of maximum ion energy for certain laser parameters when using thinner targets well below 500 nm. These observations were explained by an ion acceleration mechanism based on relativistic transparency.

2.4.2 Ion acceleration in the transparency regime

As explained above, the interaction of a short-pulse laser with a thin target leads to relativistic heating of the electrons that subsequently propagate through the target. However, the acceleration of electrons to relativistic energies leads to a relativistic mass increase and thus to an increase of the critical density given in equation (2.11). If the target is thin enough, namely in the sub-micrometer regime, the laser heating additionally causes a rapid expansion of the target volume which is connected to a decrease of the electron density. These two effects yield a decrease of the plasma frequency that eventually drops below the laser frequency. At that point the plasma is no longer opaque and the laser can propagate into the material [72], which allows coupling of the electrons to the laser inside the target volume. Because the target stays classically overdense during this stage of the acceleration mechanism, it is called *relativistically transparent*. At late times, due to the expansion of the target, the electron density drops below the critical density and the target gets classically underdense, which marks the end of the acceleration.

This kind of acceleration mechanism is a quite new topic in research and leaves many open questions to this day. One of the most interesting subjects is the problem how exactly the energy of the electrons is transferred to the ions. One possibility could be the interaction via instabilities, while the electrons regain their lost momentum through interaction with the laser field.

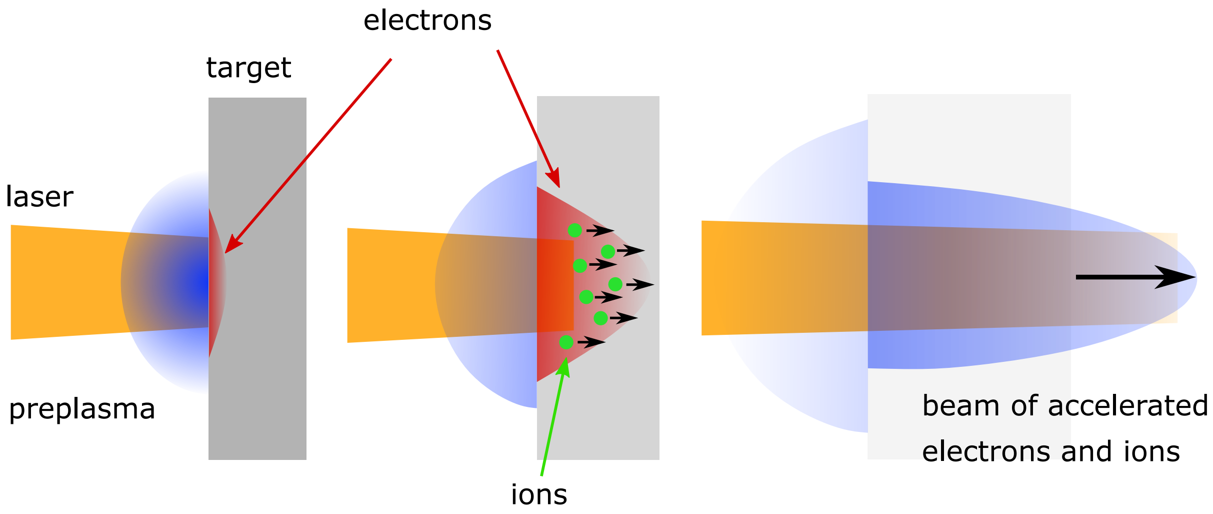

Figure 2.4.: Sketch of ion acceleration in the relativistic transparency regime. (left) The main pulse of the laser accelerates the electrons at the critical density to relativistic energies. (center) Due to the relativistic mass increase as well as the expansion of the target, the target gets relativistically transparent to the laser. Inside the target volume, the electrons transfer their energy to the ions which are accelerated, while themselves regain their energy by interaction with the laser field. (right) The target expands to the point where it gets classically underdense and the acceleration stops.

In 2006 Yin *et al.* [24] introduced 1D particle in cell (PIC) simulations proposing a mechanism called *laser break-out afterburner (BOA)*, where the Buneman instability is responsible for the coupling of the electrons to the ions. An analytical description was given by Albright *et al.* [73] resulting in a good agreement with the simulations. However, the role of the Buneman instability still needs to be verified as there is no successful experimental confirmation of this theory to this day.

Another widely discussed matter is the ability to efficiently accelerate not only light ions to higher energies than possible with the TNSA mechanism, but also the acceleration of heavy ions due to the interaction of the laser with the target volume during the transparency regime. Several simulations [24,74,75] of the interaction of short-pulse as well as long-pulse lasers with thin carbon targets resulted in carbon energies in the range of 100 MeV up to several GeV. First experiments [21,22,66] with laser intensities above $10^{19}\,\mathrm{W/cm^2}$ indicate enhanced acceleration of carbon ions up to 700 MeV. A possible explanation is given by the higher conversion efficiency from laser energy into ion energy predicted in [24] and experimentally reported in [21,22,76], which is independent of the q/m ratio because of the volumetric laser-matter interaction which prevents shielding of heavier ions from the electric field due to the accelerated light ions.

The ion energy spectrum is predicted to be quasi-monoenergetic at early stages of the acceleration mechanism and evolves in a distribution that is decreasing to higher energies at late times ($t \cdot \omega_\mathrm{P} \gtrsim 5000$) [24]. Experimentally, the ion spectra show an exponential decay with a sharp cutoff [21,22]. Improvements towards monoenergetic beams have been obtained by using a circular polarized laser or a larger focal spot [22]. Another possibility could be the use of double-foil targets [77,78] where the laser is stopped at the surface of an overdense secondary target foil avoiding further heating of the co-moving electrons, which corrupts the ion beam quality at late times of the acceleration. Nevertheless, the theoretical predictions on the ion energy spectrum could not be verified until now.

In contrast to TNSA, the radial ion distribution of the BOA mechanism shows that ions of higher energy are found to be off-axis in what Yin *et al.* called *lobes* [74], that tend to be symmetrically located around the laser propagation direction. Hegelich *et al.* [79] undertook an extensive experimental study of the properties of ions accelerated from plastic and carbon foils in the range of 40 nm to 2 μm to verify some of the main characteristics of the BOA mechanism. Amongst other things, they measured the ion distribution on-axis (0 °) and off-axis at 8.5 °. By comparing the ion energy spectra it could be found that ions of higher energies were measured in the 8.5 ° direction, which is in agreement with the theoretical predictions.

Due to the usage of very thin targets, acceleration in the transparency regime comes with high requirements for the laser. As intensities well above 10^{19} W/cm^2 are needed for that mechanism to play a role [21, 66], a high contrast is required to prevent significant expansion of the target prior to the arrival of the main pulse. Then again, this implies that an optimum target thickness depending on the laser parameters could exist. On the one hand, if the target is too thin, it gets transparent too early. This would for example be the case, if there was a considerable pre-expansion of the target. As a consequence, the energy of the laser would not be transferred effectively to the electrons and the acceleration would be inefficient. On the other hand, a thick target would remain classically overdense during the interaction time resulting in an acceleration in the TNSA regime. Therefore, the most efficient coupling of the laser to the electrons in this regime is supposed to take place when the temporal overlap of the laser peak intensity and the transparency phase of the acceleration is the highest. Experiments with carbon foils have shown such a thickness optimum with an energy increase of a factor between 2 and 4 [79] and an increase in conversion efficiency of a factor 2 to 3 [21].

Laser-based ion acceleration in the transparency regime has the potential to further improve the acceleration process. However, there are many open questions and challenges that need to be studied and verified. The difficulty lies in the measurement methods as well as the low number of laser systems in the world that are able to provide the above described parameters and thus fulfill the requirements for ion acceleration in the transparency regime.

3 Neutron generation with laser-accelerated ions

Early observations of neutron generation in a solid material directly irradiated by a laser were made in the late 1960s and explained by D-D fusion and subsequent production of ^{3}He in a cryogenic deuterium target [80]. Later measurements of the neutron spectrum from cryogenic as well as solid foil targets with thicknesses in the range of 5 µm [81] to a few 100 µm [82–84] resulted in neutron energies of a few MeV.

With the advancements of short-pulse lasers in the recent years, they gradually became an alternative to large particle accelerators. This provides the possibility of using laser-accelerated ions as a source for neutron production, which is realized by interaction of the ions with a bulk material. Simulations on laser-induced neutron yields and angular distributions done by Davis *et al.* in 2010 [85] and Petrov *et al.* in 2013 [86] predicted high neutron numbers up to 10^8 neutrons per steradian and joule of laser energy with a pronounced increase of the neutron yield in the laser forward direction. In addition, number and spatial distribution of the neutrons were found to be highly dependent on laser parameters like intensity and pulse length as well as on target materials.

In 2011, Willingale *et al.* [87] studied D-D fusion neutron yields from bulk deuterated polyethylene targets at laser intensities of the order of 10^{19} W/cm^2 and compared it with the so-called *pitcher-catcher* configuration. In this scheme, a high intensity short-pulse laser is focused on a thin polymer foil (pitcher), where ions are accelerated for instance by the above described mechanisms (sections 2.4.1 and 2.4.2). They impinge a secondary converter target (catcher) and generate neutrons via nuclear reactions. Willingale *et al.* found a higher neutron yield for a 1.5 mm deuterated polyethylene bulk target compared to a 13 µm mylar foil with a 1 µm layer of deuterated polystyrene as pitcher target and a 0.5 mm deuterated polystyrene catcher. However, they pointed out the capability of the pitcher-catcher configuration to result in a higher and more collimated neutron flux than the bulk target when using higher laser intensities or other nuclear reactions. In addition, with respect to the new ion acceleration mechanism in the transparency regime, thinner targets could also be a solution to the observed suppression of deuteron acceleration from the plastic foil due to the contamination layer.

The neutron yield and angular distribution amongst others also depend on the chosen materials for the primary target and the catcher. The following sections will introduce different neutron production reactions as well as target and catcher materials going along the path of the neutron generation chain starting with the primary target foil, and motivate the combination used for the experiments conducted in the framework of this thesis.

3.1 Primary target material

Typical solid targets for laser-ion acceleration in the TNSA regime are thin metal foils with thicknesses in the micrometer range, like gold or aluminum, where mainly the contamination layer at the rear side, but also a part of the bulk material are accelerated. However, to keep the conversion efficiency from laser energy to ion energy (cf. section 2.4.1) as well as the possibility of capture reactions inside the catcher high, the use of light ions is advantageous compared to heavier ones. Hence, polymer foils with a high content of protons are an ideal choice because protons can not only be accelerated from the contamination layer, but also partly from the bulk material, especially in the transition regime from the TNSA mechanism to relativistic transparency.

The lightest ion species besides protons are deuterons. They can be accelerated by irradiating thin deuterated polymer foils, although the acceleration is less efficient due to the lower charge to mass ratio [21]. To compensate that, using thinner targets could be a solution. As described in section 2.4.2, targets with thicknesses of a few 100 nm irradiated with high laser intensity can get relativistically transparent during the acceleration phase. In this regime more efficient acceleration of heavier ions compared to TNSA and additional acceleration from the bulk material is predicted.

As the following sections will show, there are several advantages using deuterons regarding neutron yield and the generation of a directed neutron beam compared to an isotropic emission. In combination with the above described properties, thin deuterated polymer foils with thicknesses between 200 and 1200 nm were used during the experiments conducted in the framework of this thesis.

3.2 Reactions inside the catcher

Impinging the catcher, the protons and deuterons initialize (p,n) and (d,n) reactions. In these processes, the energy of the projectile is transferred to another nucleon, which then has enough energy to escape the potential of the nucleus. In a classical picture, these reactions can be described as a collision between the incoming ion and a nucleus of the catcher material [86] as it is sketched in Figure 3.1. Assuming, that the mass of the projectile is much smaller than those of the target nucleus and the product nucleus of the reaction, the maximum energy of the emitted neutron can be derived to $E_n^{\max} \approx E_{\text{ion}} + Q$ [86] with the energy of the projectile E_{ion} and the Q-value $Q = K_i - K_f$, which is defined as the difference of the kinetic energies before and after the reaction [88]. These compound reactions provide an isotropic neutron distribution.

A special (p,n) or (d,n) reaction is the pre-equilibrium emission [89–92], which occurs at high projectile energies. During this reaction the energy of the incoming particle is not fully transmitted to all degrees of freedom of the compound nucleus before a nucleon is emitted. Neutrons emitted by a pre-equilibrium reaction are strongly orientated in the forward direction of the incoming projectile and reach higher energies compared to neutrons emitted by an equilibrium emission [92].

If an incoming deuteron has a kinetic energy above its binding energy $E_B = 2.225$ MeV, an additional reaction called *deuteron break-up*, first described by Oppenheimer and Phillips [93],

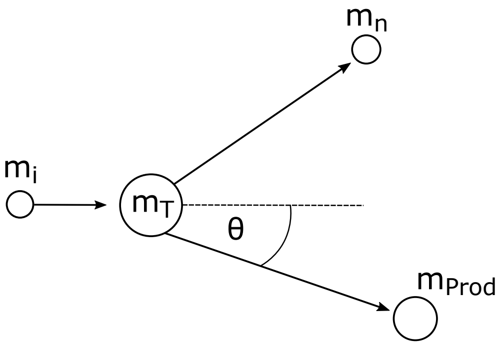

Figure 3.1.: Nuclear reactions described by a classical collision of the ion m_i with the target nucleus m_T yielding an emitted neutron m_n and the product patricle m_{Prod}.

can occur. During this process the deuteron splits up into a proton and a neutron. For reactions not involving absorption processes, the simplest physical picture can be described as follows [94]: as the deuteron with energy E_d approaches the nucleus, it is decelerated in the Coulomb field and has lost the energy $1/(4\pi\varepsilon_0)\ Ze^2/R$ when it disintegrates in the distance R from the nucleus. Assuming that the proton and the neutron both receive the same amount of energy, the final energy of the two particles can be expressed as:

$$\begin{aligned} E_n &= \frac{1}{2}\left(E_d - \frac{1}{4\pi\varepsilon_0}\frac{Ze^2}{R} - E_B\right), \\ E_p &= \frac{1}{2}\left(E_d + \frac{1}{4\pi\varepsilon_0}\frac{Ze^2}{R} - E_B\right) \end{aligned} \tag{3.1}$$

with the deuteron energy E_d. The change of sign in the deceleration term for the proton energy originates from the acceleration protons experience in the Coulomb field of the nucleus after the reaction.

By measuring the proton energy spectra of the deuteron break-up reaction and verifying the position of its maximum, the distance R, in which the reaction takes place, can be determined. Early experiments with deuterons in the range of 8 to 15 MeV interacting with mid- and high-Z elements showed that R is larger than the typical nuclear radius [95,96] and the interaction consequently is caused by the long-range Coulomb force. Contrary to that, high deuteron energies and low-Z materials result in a smaller radius and the break-up reaction is assumed to be due to nuclear forces. In this case, the reaction involves the interaction of one of the constituents with the nucleus, namely in stripping processes. After the break-up reaction, the remaining nucleons propagate further through the catcher and are able to take part in additional nuclear equilibrium or pre-equilibrium reactions, which results in an increased neutron yield.

Production of high energy neutrons through stripping of protons from a deuteron was first described by Serber in 1947 [97] and identified as the main contribution to the neutron yield for small scattering angles [86, 98, 99], which leads to an increase of the neutron yield in the forward direction of the incoming deuteron beam.

Based on these results, the nuclear deuteron break-up and the pre-equilibirum emission can be considered as the main reactions yielding the forward directed neutron beam of a laser-driven neutron source.

The type of reaction and thus the spectrum and angular distribution of the emitted neutrons not only depend on the projectile, but also on the target nucleus, hence the material of the catcher. As described in the previous section, a nuclear deuteron break-up was identified as the main contribution to the forward directed component of the angular neutron distribution. This reaction only can occur at close range to the nucleus, which requires high deuteron energies of at least several MeV and a catcher consisting of a low-Z material. In addition, the material should have high (d,n) and (p,n) reaction cross sections, whereas the cross section for neutron capture reactions should be low.

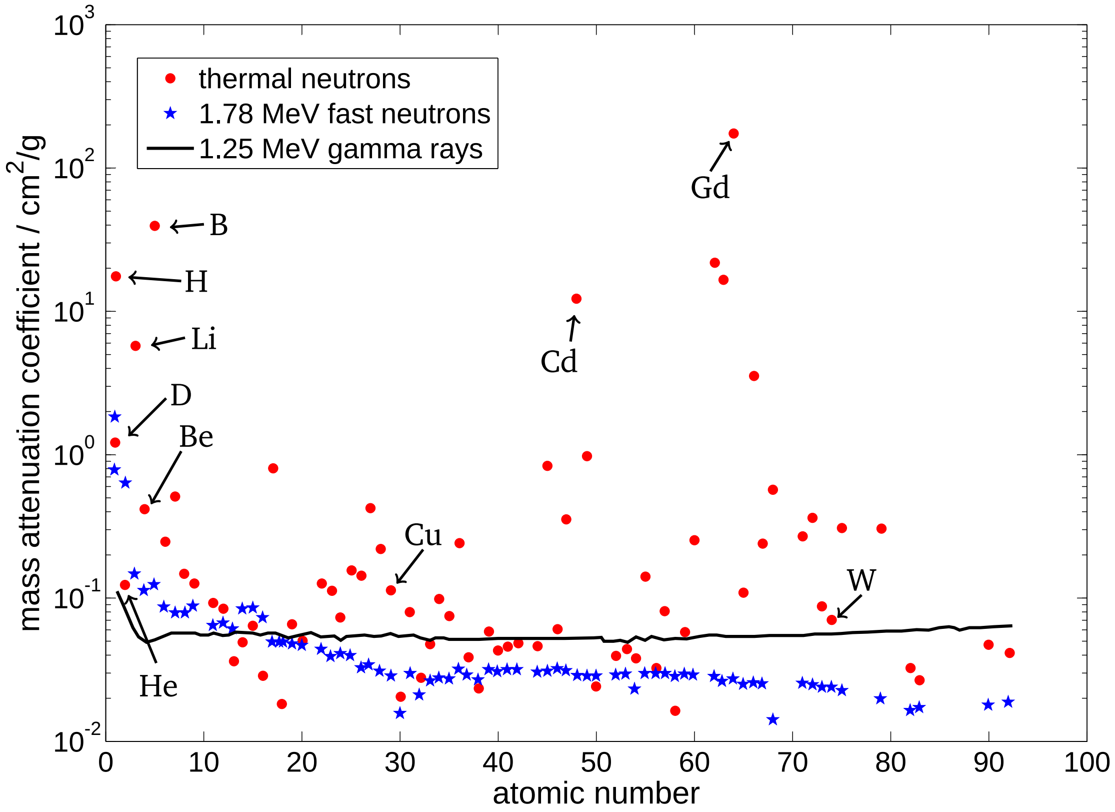

Figure 3.2.: Mass attenuation coefficient of fast (blue) and thermal (red) neutrons with 1.78 MeV and 25 meV, respectively. As a comparison, the attenuation coefficient of gamma rays with an energy of 1.25 MeV (solid line) is displayed. While the attenuation coefficient for gamma rays stays almost constant for different materials, the coefficient for thermal neutrons varies considerably. Fast neutrons show a similar behavior to gamma rays. The plot is adapted from [100] and is based on the NEA data base [101].

Considering these conditions, materials with a high hydrogen content and also boron for instance can not be used as a suitable catcher, as they have a high possibility for neutron capture reactions. However, cross sections depend on the neutron energy and thus the choice of material is also dependent on the energy range of neutrons that are to be generated. Figure 3.2 shows the mass attenuation coefficient for thermal neutrons (red dots) with an energy of 25 meV and fast neutrons with an energy of 1.78 MeV (blue stars) compared to gamma rays with an energy of 1.25 MeV (black line) [100, 101]. The graphs show that the attenuation of neutrons is considerably different for fast and thermal neutrons.

One material, which fulfills all the mentioned requirements, is beryllium. It has low mass attenuation coefficients for thermal as well as fast neutrons and high reaction cross sections for (p,n) and (d,n) reactions [102]. A disadvantage are the health hazards of beryllium, for instance the inhalation of its dust, and thus the handling of the material. Other materials commonly used in experiments are deuterated polymer (CD) and lithium catchers [27, 103–106]. CD is an interesting material because in addition to the above described reactions, fusion reactions can occur. These are D-D fusion where a neutron with a kinetic energy of 2.45 MeV is emitted, and D-T fusion which leads to the emission of 14.1 MeV neutrons. Lithium has high (p,n) and (d,n) cross sections, but also a high possibility for neutron capture reactions in the low-energy range up to 1 keV.

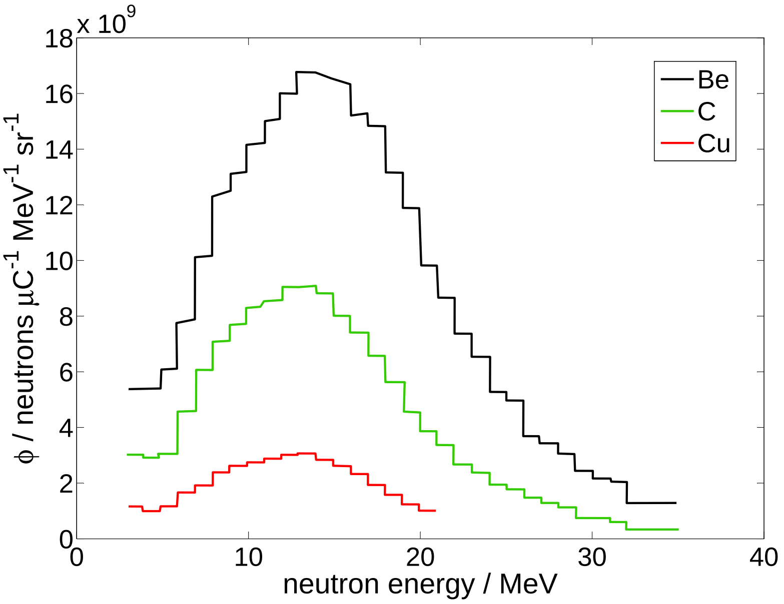

Figure 3.3.: Comparison of the neutron flux originating from different catcher materials. The data is taken from the experimental results of reference [107].

One of the first experimental comparisons of the neutron yield from different materials was done by Meulders *et al.* [107] in 1975, who investigated the neutron yield from deuterons of different incident energies. Their results are displayed in Figure 3.3, which shows the neutron energy spectra of copper, carbon, and beryllium for an initial deuteron energy of 33 MeV. The neutron yield of beryllium is the highest over the whole measured energy range. At the peak energy, beryllium results in 5.5 more neutrons than copper and in more than 1.5 times as many neutrons as carbon.

A comparison between lithium and beryllium was published by Lone [108] and shows a one order of magnitude higher neutron yield for beryllium for deuteron energies in the range of

10 to 50 MeV. However, the reaction thresholds of lithium for these reactions are lower compared to those of beryllium, which can be an advantage in practice.

Based on these results, the two materials chosen for the experiments conducted in the framework of this thesis were beryllium and lithium deuteride.

3.4 State of the art: characterization of a laser-driven neutron source

Over the last 20 years, numerous experiments to characterize laser-driven neutron sources have been conducted. Fields of study were the neutron yield from different generation processes, including various target and catcher materials as well as geometries, angular distribution, and energy spectrum. The following section will give an overview of the achievements and state of the art in literature up to the beginning of the author's work in 2014.

Table 3.1 shows a list of experiments done in the last two decades specifying the results regarding energy on target, used neutron detector, target-catcher configuration, and direction as well as value of the maximum neutron yield. As described in the previous sections, laser-driven neutron sources show a maximum emission in the direction of the initial ion's propagation path [27, 82, 87, 109, 110]. The highest neutron yield in this direction was achieved by Roth *et al.* in 2013 [25], who reached neutron numbers of $1 \cdot 10^{10}$ per steradian with a deuterated polymer foil as primary target and a beryllium catcher.

A comparison between different catcher materials impinged by deuterons from table 3.1 results in the highest neutron number, namely of the order of 10^8 per steradian and joule, for the beryllium catcher. Deuterated polymer yields numbers between $1.5 \cdot 10^5$ and $3 \cdot 10^6$ neutrons per steradian and joule and thus is comparable to a lithium or lithium flouride catcher, which all result in neutron numbers of the order of 10^6 per steradian and joule. These experimental results are in agreement with the explanations in the previous section.

The emitted neutron spectrum shows an exponential decay with cut-off energies from several MeV [87, 111] up to more than 10 MeV [112]. There are a few authors, who published measured neutron time of flight or raw energy spectra with preliminary curve progressions that do not show an exponential behavior, but reach even higher cut-off energies in the region of several 10 MeV [103] up to 100 MeV [25, 109].

On the basis of these achievements, several applications of laser-driven neutrons have been proposed. In 2004, Lancaster *et al.* [106] investigated the feasibility of fast neutron radiography with a laser-driven neutron source. They used the $^{7}\mathrm{Li}(p,n)^{7}\mathrm{Be}$ reaction and achieved a maximum yield of $3 \cdot 10^8$ neutrons per steradian. For an application in neutron radiography which requires much higher neutron yields (cf. table 3.3 in section 3.5), Lancaster *et al.* proposed using higher laser energies and a different catcher material and thus a different production reaction, namely $^{208}\mathrm{Pb}(p,n)^{208}\mathrm{Bi}$. In 2013, Roth *et al.* [25] could demonstrate the first radiograph of a structured object irradiated by laser-driven neutrons. They used the $^{9}\mathrm{Be}(p,n)^{9}\mathrm{B}$ and the $^{9}\mathrm{Be}(d,n)^{10}\mathrm{B}$ as well as deuteron break-up reactions and obtained a maximum neutron yield of $1 \cdot 10^{10}\,\mathrm{sr}^{-1}$.

Higginson *et al.* [114] studied the possibility of using laser-driven neutrons for temperature measurements of shocked materials with neutron resonance spectroscopy. He found that this application is in general feasible, but depending on the moderator material (cf. section 3.6).

year	Ref	energy on target [J]	detector	target configuration	direction	neutron yield [1/sr]	comments
1999	[82]	30	BF_3	bulk, DD fusion	forward	$1 \cdot 10^7$ scaled to 4π	
2004	[106]	80	CR39	CH→Li	backward	$3 \cdot 10^8$	$2 \cdot 10^8$ n/sr in forward direction
	[113]	300	Cu activation	Al→Li	not specified	$4 \cdot 10^9$	
2010	[103]	127	CR39	CD_2 →LiF	forward	$8 \cdot 10^8$	
2011	[87]	6	plastic scint.	bulk CD, DD fusion	forward	$5 \cdot 10^4$	CD→CD: $2 \cdot 10^4$ n/sr
2012	[110]	360	CR39	CD→LiF	forward	$8 \cdot 10^8$	
2013	[111]	6	BD	D_2O→CD	not specified	$9 \cdot 10^5$	
	[25]	80	BD	D→Be	forward	$1 \cdot 10^{10}$	
	[112]	1	BD	CH→Li	not specified	$1 \cdot 10^7$	CD→Li: $3 \cdot 10^6$ n/sr

Table 3.1.: Different experiments on the characterization of laser-driven neutrons conducted in the last two decades. The campaigns are listed chronologically and are compared regarding laser energy on target, the detector type used for neutron measurement, target-catcher configuration, and direction as well as value of the maximum neutron yield. The detector abbreviations are: BD - bubble detectors and BF_3 - boron triflouride detector. A detailed description of different neutron detectors is given in chapter 4.

To further optimize a laser-based neutron source for applications, Ellison and Fuchs [115] suggested a temporal narrowing of the broad neutron pulse after a certain distance to the source by a micrometer thin catcher and a microlens behind the primary target. This microlens was proposed as a hollow cylinder irradiated with a high-intensity short pulse laser which creates a radial electric field from hot electrons inside the cylinder [116]. As a compromise, a decrease in the neutron yield has to be accepted when applying this method. Nevertheless, this would be compensated by a higher initial ion flux, that could be achieved with new facilities reaching higher ion numbers and energies, such as *Extreme Light Infrastructure (ELI)* [117] for example.

3.5 Comparison with conventional neutron sources

This section will give an overview of different conventional neutron sources and compare them to a laser-based neutron source regarding maximum neutron flux, pulse duration, angular distribution, and energy spectrum.

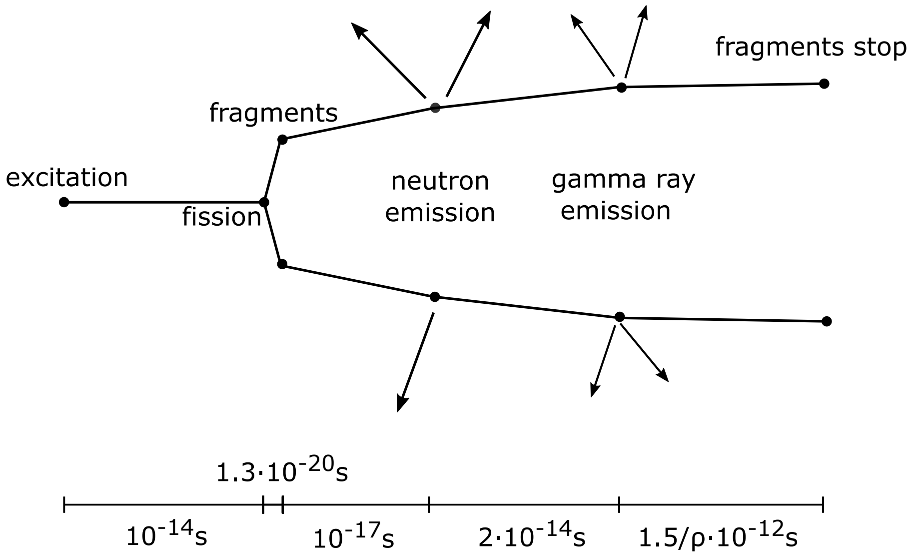

Figure 3.4.: Sketch of a fission process with corresponding time lines. ρ represents the density of the material. The scale below shows the different time steps. Adapted from [11].

Conventional neutron sources can be divided in three general classes: fusion, fission, and spallation sources. Neutron production via fusion is mostly achieved with the hydrogen isotopes deuterium and tritium:

$$\begin{aligned} D + D &\rightarrow {}^3\mathrm{He} + n\,(2.45\,\mathrm{MeV}) \\ D + T &\rightarrow {}^4\mathrm{He} + n\,(14.1\,\mathrm{MeV}). \end{aligned} \tag{3.2}$$

Both reactions emit high energy neutrons in the MeV range from a compound nucleus. However, for the fusion process to take place, kinetic energies in the range from 10 to 100 keV corresponding to temperatures of the order of 10^8 to 10^9 K are necessary to overcome the Coulomb repulsion of the two nuclei [118]. To meet these conditions and generate an efficient neutron source, the fuel has to be strongly compressed or heated. Proposed fusion schemes for different applications are for example magnetic confinement fusion (e.g. [119]), inertial confinement fusion (e.g. [120, 121]), and fast ignition [122, 123]. Neutron production in large fusion reactors or smaller tubes filled with deuterium and tritium gas results in a temporally continuous and isotropic neutron source.

In fission reactors, mostly containing ^{235}U, neutrons are generated via neutron capture and subsequent fission of the product into two fragments with nearly equal masses [124]. During this process, one or more neutrons with an average energy of about 2 MeV [11] are evaporated from the highly excited nuclei on a time scale of 10^{-14} s. Each neutron decreases the energy of the excited fragment by its kinetic and its binding energy $E_{\mathrm{kin}} + E_{\mathrm{B}}$. At the point where the leftover excitation energy of the fragment is smaller than the neutron's binding energy, the fragment further de-excites by emission of gamma rays. A sketch of the process with corresponding time scales is shown in Figure 3.4 [11].

Fission reactors provide spatially homogeneous, high neutron fluxes of the order of $10^{15}\,\mathrm{cm^{-2}s^{-1}}$ [115] with an energy spread of a few MeV, which can be seen in Figure 3.5.

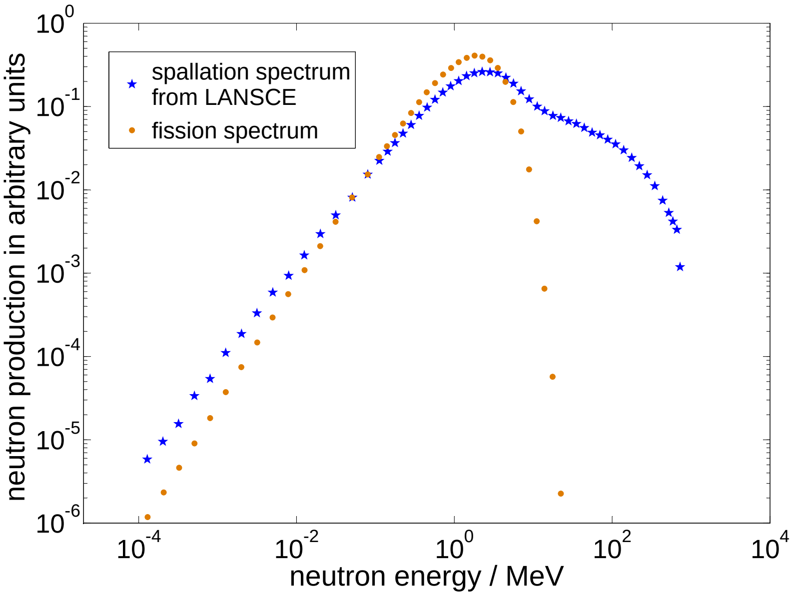

Figure 3.5.: Neutron spectrum from fission (orange) and spallation (blue). The curve integrals are normalized to unity. The data is taken from reference [14].

Accelerator-based spallation sources use high-energy particles that collide with a thick high-Z target. The reactions which follow can be divided into two stages [14]. In the first one, an intranuclear cascade of high-energy hadrons with energies greater than 20 MeV is created. During this stage some of the particles can escape the nucleus. In the second step, the so-called *nuclear de-excitation*, the excited nucleus relaxes and evaporates particles with energies below 20 MeV. The majority of the emitted particles is neutrons with energies in the range of 2 MeV [124]. In addition, high-energy neutrons up to several 100 MeV can be produced by direct interaction with accelerated particles (usually protons) that have a de Broglie wavelength shorter than the dimensions of the nucleus. In this case, the maximum energy of the neutron depends on the energy of the incoming proton. A neutron spectrum from spallation at the LANSCE facility at Los Alamos National Laboratory, USA, is shown in Figure 3.5.

Accelerator-based spallation sources provide the highest neutron fluxes in the range from 10^{15} to more than $10^{16}\,\mathrm{cm^{-2}s^{-1}}$ [13, 15]. Furthermore, due to the finite pulse duration of the accelerated particles, neutrons are emitted on a short time scale, usually of the order of several 100 ns to microseconds. However, it should be mentioned, that there is a continuous spallation source in the world, which is SINQ [125] in Switzerland.

The properties of conventional neutron sources compared to a laser-driven neutron source are summarized in table 3.2. Fusion and fission reactors are high-flux neutron sources with an isotropic angular distribution. However, due to their temporally continuous emission, they are only applicable to steady state measurements. For probing quickly changing processes, such as shock propagation inside a material [126–129], intense pulsed sources are inevitable. Up to now, accelerator-based spallation sources provide the highest neutron fluxes with pulse lengths between several 100 ns and a few microseconds, but require a large and expensive accelerator infrastructure. In addition, due to the high neutron energies and additional production of highly radioactive products during the reaction, these facilities need massive shielding.

	fusion	**fission**	**spallation**	**laser-induced**
neutron flux	$< 10^{10}\,\mathrm{cm^{-2}s^{-1}}$ [130]	$10^{15}\,\mathrm{cm^{-2}s^{-1}}$	$10^{16}\,\mathrm{cm^{-2}s^{-1}}$	max. $10^{10}\,\mathrm{sr^{-1}ns^{-1}}$
spectrum	exponential decay up to 14 MeV [130]	up to several 10 MeV with a maximum at 2 MeV	high energies up to several 100 MeV [14]	exponential decay [27] up to more than 100 MeV [25]
time scale	continuous		continuous or pulsed (several 100 ns to µs)	pulsed (ns)
angular neutron distribution	homogeneous		directed, depending on nuclear reactions	

Table 3.2.: Comparison of the properties of different conventional neutron generation processes and a laser-driven neutron source.

application	**required neutron yield**
diagnostics *fuel cells, hydro storage engineering*	10^{11} to $10^{12}\,\mathrm{s^{-1}}$
neutron cancer therapy	10^{12} to $10^{13}\,\mathrm{s^{-1}}$
fast neutron radiography	10^{10} to $10^{14}\,\mathrm{s^{-1}}$
material processing, nuclear material research and development	$> 10^{15}\,\mathrm{s^{-1}}$
neutron resonance spectroscopy	10^{11} to $10^{13}\,\mathrm{s^{-1}}$

Table 3.3.: List of applications for neutrons and the corresponding required source yield [131–134].

Laser-driven neutron sources are a very promising alternative. They provide peak neutron yields of the order of 10^{10} neutrons per steradian in the forward direction and an order of magnitude less in the sideward directions [25], which corresponds to a total neutron yield of 10^{11} per pulse. The temporal resolution in the sub-nanosecond regime [25] allows fast neutron in-situ measurements on very short time scales. Furthermore, due to the compact design, such a source provides the possibility of conducting close-coupled experiments, which greatly reduces the shielding requirements. Together with the low costs, this expands the accessibility for neutron applications from large facilities to smaller institutions, such as universities or industrial companies.

As a comparison, table 3.3 lists a few applications and the required neutron yield of the source.

3.6 Moderation and neutron resonance spectroscopy

High-energy neutrons are necessary for some applications, such as fast neutron radiography. However, there are applications, where epithermal or thermal energies are preferable. One of these is neutron resonance spectroscopy, which amongst others allows to identify the elemental composition of bulk materials which have pronounced resonances in this energy regime. To provide neutrons with these energies, they have to be slowed down in a dedicated material. In the framework of this section, two different approaches to theoretically describe neutron moderation will be discussed, followed by the concept of NRS related to the experimentally applied measurement method.

Moderation of fast neutrons is based on energy loss during scattering reactions. As a laser-driven neutron source already provides neutrons in the low-energy range due to the exponentially decaying spectrum (see section 3.5), the goal of moderating laser-generated neutrons is to maximize the neutron yield in the desired energy range for the specific application. This includes the appropriate choice of the moderator material as well as its geometry and the right combination with an adequate catcher material and geometry, respectively.

In contrast to charged particles, neutrons do not interact via the Coulomb force with the nuclei of the moderating material, but by the strong force [135]. In the following, only elastic interactions with a nucleus initially at rest will be considered for describing the slowing down of neutrons inside a material. In a kinematic approach, the final neutron energy E_n in the laboratory system can be derived from momentum and energy conservation:

$$E_n = \frac{E_0}{(A+1)^2}\left[\cos\Theta + \sqrt{A^2 - \sin^2\Theta}\right]^2 \tag{3.3}$$

with the initial energy of the neutron E_0, the mass of the scattering nucleus A and the scattering angle Θ in the laboratory system. For moderation in hydrogen, equation (3.3) can be rewritten in a simplified way [135]:

$$E_n = E_0 \cos^2\Theta. \tag{3.4}$$

The angular energy distribution of the scattered neutrons can be described with the following expression:

$$\frac{\mathrm{d}\sigma}{\mathrm{d}E} = \frac{\mathrm{d}\sigma}{\mathrm{d}\Omega}\frac{\mathrm{d}\Omega}{\mathrm{d}E} = \frac{\mathrm{d}\sigma}{\mathrm{d}\Omega}\cdot 2\pi\frac{\mathrm{d}(\cos\Theta)}{\mathrm{d}E} \tag{3.5}$$

with the differential cross section $\mathrm{d}\sigma/\mathrm{d}\Omega$, that can be expressed in terms of the differential cross section in the center of mass (CM) system by

$$\frac{\mathrm{d}\sigma}{\mathrm{d}\Omega} = \left(\frac{\mathrm{d}\sigma}{\mathrm{d}\Omega}\right)_{\mathrm{CM}}\frac{\mathrm{d}\Omega_{\mathrm{CM}}}{\mathrm{d}\Omega} = \left(\frac{\mathrm{d}\sigma}{\mathrm{d}\Omega}\right)_{\mathrm{CM}}\frac{\sin\Theta_{\mathrm{CM}}\mathrm{d}\Theta_{\mathrm{CM}}}{\sin\Theta\mathrm{d}\Theta} = \left(\frac{\mathrm{d}\sigma}{\mathrm{d}\Omega}\right)_{\mathrm{CM}}\cdot 4\cos\Theta \tag{3.6}$$

because the relation between the two scattering angles Θ and Θ_{CM} in the laboratory and the CM system for a neutron-proton collision can be expressed as $2\Theta = \Theta_{\mathrm{CM}}$.

Including (3.6) and the derivative of equation (3.4) in (3.5) leads to

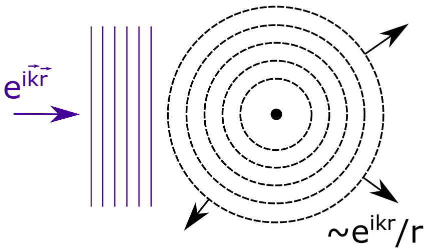

Figure 3.6.: Sketch of the quantum mechanical description of particle scattering. The incoming plane wave is shown in blue. The scattered wave is described by a circular wave expanding from the scattering center.

$$\frac{d\sigma}{dE} = \left(\frac{d\sigma}{d\Omega}\right)_{CM} \frac{4\pi}{E_0}. \tag{3.7}$$

It shows that the energy distribution of scattered neutrons in the laboratory frame is determined by the differential cross section in the CM system, which can be derived by applying the quantum mechanical scattering theory [88, 136]. As it is schematically shown in Figure 3.6, the incoming particle is described by a plane wave $\Phi_{in}(\vec{r}) = e^{i\vec{k}\vec{r}}$, whereas the scattered particle is described by an outgoing circular wave, which is expressed as $\Phi_{out}(\vec{r}) = f(\vartheta, \varphi)e^{\mathrm{ikr}}/r$. The scattering amplitude $f(\vartheta, \varphi)$ directly defines the differential cross section in the CM system

$$\left(\frac{d\sigma}{d\Omega}\right)_{CM} = |f(\vartheta, \varphi)|^2. \tag{3.8}$$

Moderators are designed to scatter neutrons without absorbing them. On the one hand, they should contain light elements, such as hydrogen, deuterium, carbon, and beryllium, to maximize the mean energy loss per collision. On the other hand, the materials are required to have low neutron capture cross sections to preserve a high neutron flux. In this regard, not only the composition of the moderator itself has an influence on the thermal neutron flux, but also possible shieldings or mounts. Thus, the whole moderating system contributes to the thermalization properties [137].

Moderators usually are enclosed inside a reflector material (e.g. beryllium or tungsten), which is to increase the neutron yield in the desired energy range by scattering fast neutrons back into the moderator. Additionally, moderators for pulsed sources contain a decoupling material (e.g. cadmium) which can be placed between the moderator and the reflector to absorb neutrons that are diffusing for a long time inside the moderating system. As a consequence, the additional temporal broadening of the neutron pulse inside the moderator is kept as narrow as possible [124].

As mentioned above, one of the applications for moderated neutrons is neutron resonance spectroscopy. It can be used to determine the elemental composition of a bulk material because it is a non-destructive method for sample probing [26] and provides a complementary diagnostic to measurement methods that are using charged particles or x-rays. Each element has a

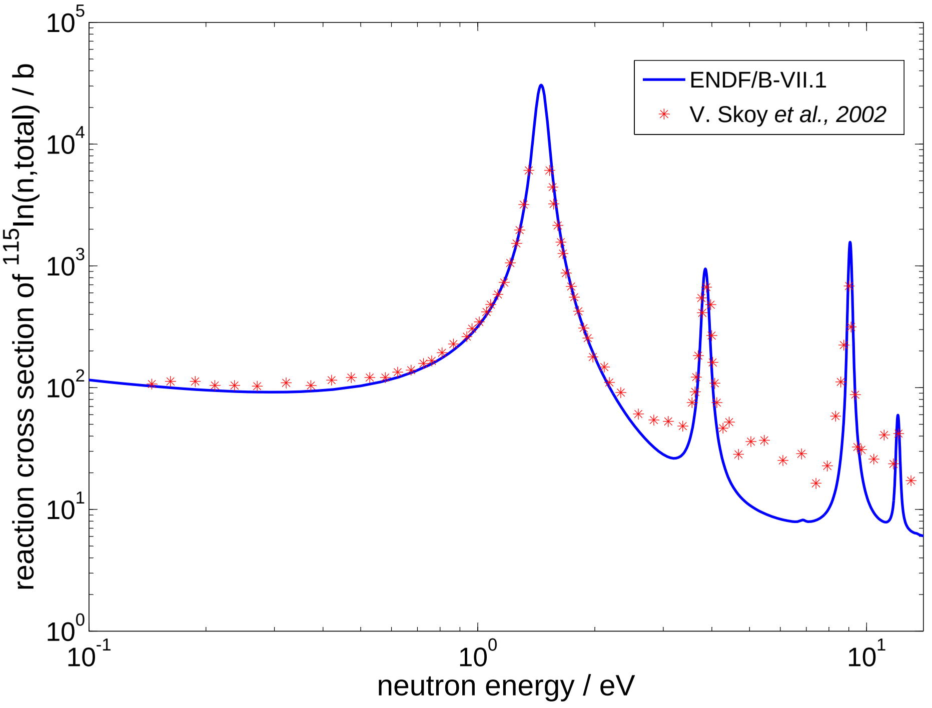

Figure 3.7.: Total reaction cross section of neutrons with ^{115}In within an energy interval from 0.1 to 15 eV. The solid line shows an ENDF/B-VII.1 calculation taken from reference [102]. The red dots are taken from reference [138].

unique energy-dependent signature of resonances, which can be used as a fingerprint to identify the material. Many mid- and high-Z elements have pronounced resonances in the epithermal energy region. Figure 3.7 shows exemplarily the resonance structure of indium for the total reaction cross section with neutrons.

Nuclear resonances occur, when the energy of an incoming neutron matches one of the energy level differences of the compound nucleus. They have a Lorentzian or Breit-Wigner shape [139, 140] given by

$$\sigma_i(E) = \pi \lambdabar g \frac{\Gamma_\mathrm{n}\Gamma_i}{(E-E_0)^2 + \Gamma^2/4} \tag{3.9}$$

with $\lambdabar = \lambda/(2\pi)$. The statistical factor g takes into account different angular momentum orientations of the particles, Γ describes the total width, and E_0 the resonance energy. Γ_n represents the partial width of the input channel of the reaction, labeled with the index n for incoming neutrons. Γ_i is the partial width of the reaction output which can be neutrons, protons, gamma rays or other radiation. The total cross section is derived by summation of all possible reaction cross sections.

Experimentally the measurement of the resonance can for example be conducted with a time of flight (ToF) detector behind the sample [26, 141]. As neutrons with an energy that matches the resonance are captured or decelerated within the material, the resonance is visible as a negative peak in the ToF transmission spectrum. The theoretical Breit-Wigner shape is affected by Doppler broadening and resolution broadening under experimental conditions [26, 141]. Doppler broadening originates from the thermal motion of the target nuclei. For metallic samples, this can be described by a Debye continuum [142], which results in a Gaussian shaped broadening [126, 140, 143] with a standard deviation

$$\Gamma_D = \sqrt{\frac{4k_\mathrm{B}TE_\mathrm{n}m_\mathrm{n}}{M}} \tag{3.10}$$

with the neutron mass m_n, the mass of the nuclei M, and the neutron energy E_n. This method can be used to determine the temperature of a bulk material [126, 144, 145].

Resolution broadening is caused by the experimental conditions. This includes the temporal resolution of the time of flight measurement itself as well as the temporal dispersion of the initial neutron pulse due to the distance to the sample and due to the moderator dimensions. Sample thickness or shielding geometries, which can cause multiple scattering or undesired moderation, are other examples that also add to resolution broadening.

A drawback of NRS is the high neutron flux needed for such a measurement [133], which lies between 10^{10} and $10^{12}\,\mathrm{sr}^{-1}\mathrm{s}^{-1}$ on target. Large facilities, such as accelerator-based spallation sources, provide the highest fluxes (cf. section 3.5) and successful measurements have been conducted in many experiments (e.g. [26, 126, 146, 147]). In 2010 Higginson *et al.* [114] proposed the feasibility of laser-driven NRS for temperature measurements with a neutron yield of $1.8 \cdot 10^9$ neutrons in a picosecond pulse on the condition that the moderator has to slow down fast neutrons and direct them towards the sample with an efficiency of more than $2.2 \cdot 10^{-5}$.

4 Neutron detection

The interaction of neutrons with matter in general is weak compared to charged particles or x-rays because they do not interact with the atomic shell, but only with the nuclei. Neutron detection thus is based on secondary reactions of generated charged particles inside the detection material. These charged particles can for example be produced by recoil reactions (elastic scattering) of the neutron with a nucleus or excitation and subsequent emission.

The highest energy transfer occurs between neutrons and particles of similar mass. Thus, hydrogen-rich materials or other light elements are commonly used for neutron detection. As high and low-energy neutrons interact differently with matter (cf. section 3.3), the detection method is depending on neutron energy.

In the environment of a laser-driven neutron source, the neutron detectors are additionally exposed to high gamma fluxes and electromagnetic pulses (EMP) from the laser-matter interaction. This background represents a special challenge and correlates with particular requiremets for a detector.

The following sections will present detection methods and materials for high- as well as low-energy neutrons and describe different detector types used in the experiments and these introduced in table 3.1. In addition, the treatment of the noisy background in high-intensity laser experiements will be discussed.

4.1 Primary reactions

Low-energy neutrons have high reaction cross sections with light elements, such as helium, lithium or boron. As mentioned above, their detection is based on secondary reactions of particles generated by the interaction of a neutron with the material. Those reactions can for instance be [148]:

$$\begin{aligned} \mathrm{n} + {}^{3}\mathrm{He} &\rightarrow \mathrm{p} + \mathrm{t} + \gamma + 767\,\mathrm{keV} \\ \mathrm{n} + {}^{10}\mathrm{B} &\rightarrow \alpha + {}^{7}\mathrm{Li} + \gamma + 2312\,\mathrm{keV} \\ \mathrm{n} + {}^{6}\mathrm{Li} &\rightarrow \alpha + \mathrm{t} + 4780\,\mathrm{keV}. \end{aligned} \tag{4.1}$$

For high-energy neutrons in the range of 10 MeV and above, these reactions get highly inefficient because the reaction cross sections decrease dramatically with increasing neutron energy $\sigma \propto 1/\sqrt{E}$. In this case, neutron detection is based on the generation of a recoil proton [149]:

$$\mathrm{n} + \mathrm{p} \rightarrow \mathrm{n}' + \mathrm{p}'. \tag{4.2}$$

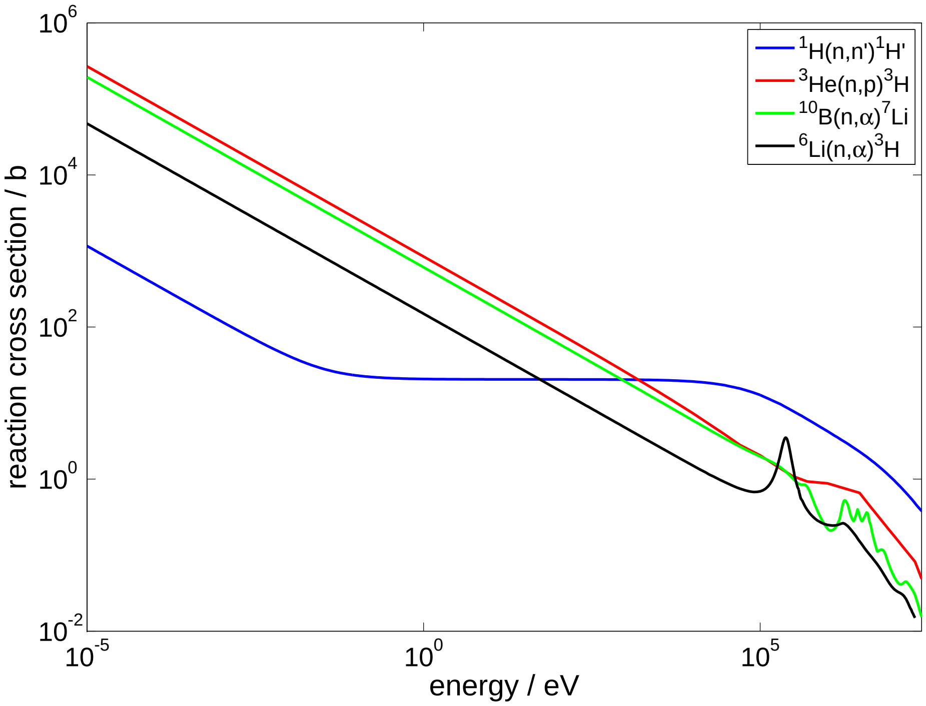

Figure 4.1.: Comparison of the neutron reaction cross sections given above. The data was obtained from references [102] and [150].

A comparison of the corresponding reaction cross sections for the above given isotopes can be seen in Figure 4.1. ^{3}He and ^{10}B have the highest cross sections, which are very similar for neutron energies up to 10 keV and thus are both suitable detection materials for thermal and epithermal neutrons. The reaction cross section of ^{6}Li is one order of magnitude below that of helium and boron, but shows a slight increase from a few barn to above 10 barn for neutrons in the range of a few 100 keV. The proton recoil reaction has the lowest cross section for low-energy neutrons, but starts to become more important at energies of a few keV.

4.2 Detection methods

The emitted secondary particles from neutron reactions inside the material can be detected by ionization processes, that lead to free electrons which can be measured in different ways. Possible detection methods are scintillators coupled to photomultiplier tubes (PMTs), microchannel plates (MCPs) with coated channels, and gas chambers. The detection methods of these systems are very similar. Neutrons induce the emission of a charged particle, namely a proton or an alpha particle, which then ionizes the material. The thus generated free electrons are multiplied either in the material itself or with an electrical device and subsequently impinge an anode.

Other possibilities are activation measurements and particle track detection. A very special neutron detector is the so-called bubble detector, which will be introduced in the following.

4.2.1 Bubble detectors

This type of neutron detector consists of a polycarbonate tube filled with a polymer gel, which is interspersed with several ten thousand super-heated halogen- and hydrocarbon droplets with diameters of 100 μm and below [149,151,152]. The pressure inside the detector can be decreased with a screw, which causes the droplets to reach the border of instability against growing. This is given by the critical radius $R_c = 2\sigma_s/(p_g - p_f)$ with the surface tension σ_s and the difference in pressures of the gas inside the bubble p_g and the fluid outside p_f [153]. When neutrons strike a droplet, they produce recoil ions that interact with the electrons of the molecules and thus deposit their energy inside the droplet [154]. As a consequence, the droplet instantly vaporizes and forms a visible bubble in the range of a millimeter in diameter. The number of bubbles is proportional to the neutron dose [155]. Figure 4.2 shows two photographs of a bubble detector irradiated with a low neutron dose (left) and one irradiated with a high neutron dose (right).

The bubbles can be counted by eye or with a specially developed readout system. It consists of an optical camera and a mirror system, which allow a view onto the bubble detector from two different perspectives. A special software analyses the photographs and displays the number of bubbles.

Figure 4.2.: Photograph of a bubble detector irradiated with a low neutron dose (left) and one irradiated with a high neutron dose (right).

Nevertheless, for the vaporization process to take place, a certain threshold of energy deposition has to be overcome which on the one hand causes the efficiency of a bubble detector to decrease at low energies (cf. Figure 4.3). On the other hand, this results in an insensitivity to gamma rays because they produce electrons whose energy deposition is below the threshold. In combination with the insensitivity to electromagnetic pulses (EMP) due to the solely kinetic detection principle, the use of bubble detectors is a great advantage in the environment of a laser-driven neutron source. The detector does not rely on a directly coupled electronic readout and the bubbles do not vanish until the detector is set back under pressure by hand. This avoids the necessity of on-shot data handling and allows to place the bubble reader as well as the computer with the analyzing software far away from the neutron source. Another benefit of bubble detectors is their reusability. After setting a detector back under pressure, the bubbles vanish and it can be prepared for the next measurement.

The sensitivity of bubble detectors was measured for neutron energies between 100 keV and 100 MeV and is shown in Figure 4.3 [151, 152] for a bubble detector with an efficiency of one bubble per mrem (or 10 μSv) of exposed neutron dose. In the energy range from 300 keV to 30 MeV the response of a bubble detector is approximately constant. However, outside of this interval the sensitivity drops dramatically by one order of magnitude.

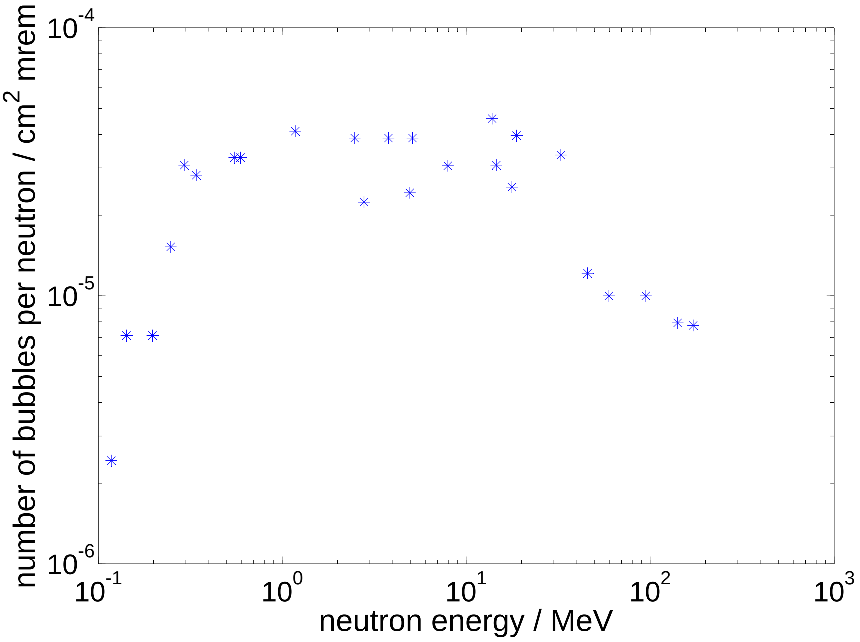

Figure 4.3.: Sensitivity of a bubble detector with a response of one bubble per mrem. The data was taken from references [151, 152].

4.2.2 Photomultiplier tubes

For the measurement with a photomultiplier tube, a scintillating material has to be coupled to the tube. As the detection of fast neutrons is mainly based on reactions of the recoil proton, organic scintillators, such as plastic scintillators, are an adequate choice. For the detection of low-energy neutrons, these materials can be doped with Li or B [156]. Inside an organic scintillator, the secondary particles generate electrons that excite molecular states, which emit ultraviolet (UV) light when they disintegrate [157]. As shown in Figure 4.4, the UV light impinges the photocathode of the PMT, which itself emits electrons via photoionization. These get multiplied by a dynode system and subsequently hit the anode, where the signal is detected. The dynodes consist of a material with a high coefficient for secondary electron emission, such as BeO and MG-O-Cs [157, 158]. With a system of 10 to 14 dynodes, a total gain of up to 10^7 can be obtained [156]. A disadvantage of a PMT is the high deviation in the transit time of each

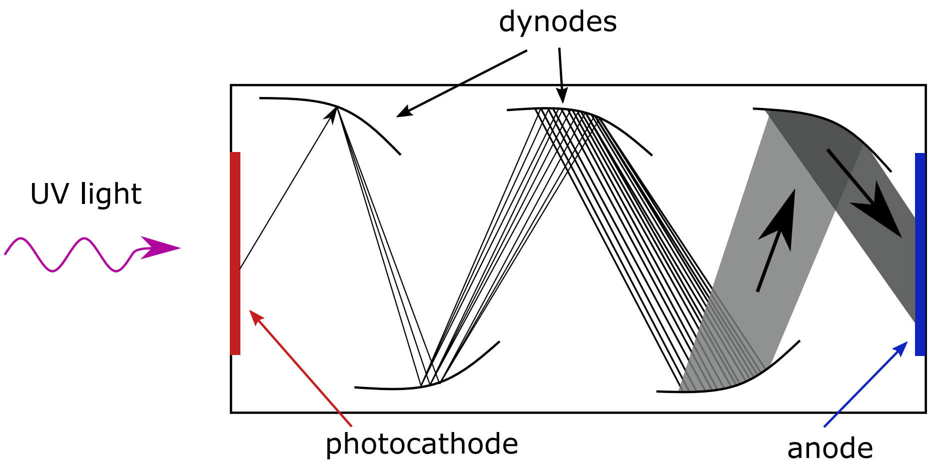

Figure 4.4.: Scheme of the electron multiplication in the dynode system of a photomultiplier tube.

electron, so-called *time jitter*, resulting mainly from the path length difference from the edges of the photocathode to the first dynode and the different electron velocities.

Photomultiplier tubes coupled to fast plastic scintillators were used as neutron time of flight detectors (nToF) during the experimental campaigns in the framework of the author's work. One of the PMT types utilized was a Hamamatsu R1250 PMT with 14 dynodes. However, this detector system's sensitivity to the high gamma flux from a laser-driven neutron source is a major problem for an experiment. It leads to saturation of the PMT and causes an overlap of the gamma peak with the high-energy component of the neutron signal in the time of flight measurement. An example can be seen in Figure 4.5 (blue).

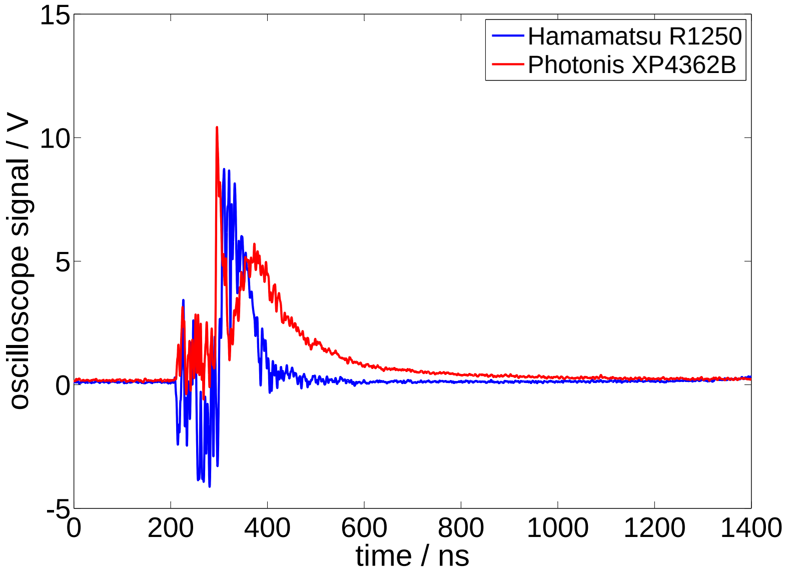

Figure 4.5.: Raw oscilloscope signals of the R1250 (blue) and XP4362B (red) PMTs. Both detectors were placed next to each other at a distance of 4.2 m to the target in the forward direction. It is clearly visible, that the gamma peak can be discriminated from the neutron signal using the XP4362B PMT, whereas both signals merge in the measurement with the R1250 PMT.

To avoid this problem, an additional new Photonis XP4362B PMT was used for the measurements in the forward direction. Compared to the other one, it has only six dynodes which strongly reduces the total gain from $1.4 \cdot 10^7$ to 10^4 [159, 160] and thus lessens saturation effects caused by the gamma flux. A time of flight spectrum measured with this configuration is displayed in Figure 4.5 (red) and enables a good discrimination of the gamma peak and the neutron signal. In the framework of a supervised bachelor's thesis, Simone Aumüller proposed the use of a faster scintillator with shorter rise- and decay times to further improve the discrimination [161](cf. chapter 8).

4.2.3 Microchannel plates

A possibility to reduce the transit time difference mentioned above is the use of a microchannel plate, which consists of a glass plate with 10^4 to 10^7 holes, so-called channels [156, 158, 162]. These channels typically have diameters between 10 and 100 μm and are arranged parallel to each other, either in the direction of the incoming particle beam or with a certain angle to it. The channel walls are treated with a semiconductor material, which emits secondary electrons. In addition, a potential difference is applied along the channels. For low-energy neutron detection, these channels can be coated or doped with an additional material, for instance boron or lithium, to at least several percent [163]. When a neutron hits the wall of one of the channels, it produces a secondary particle, which ionizes one or more atoms inside the channel wall. Another possibility is the use of a conventional photocathode in front of the MCP. The generated electrons get accelerated and multiplied by interaction with the channel walls and thus create a strong output pulse [162]. Figure 4.6 illustrates the electron multiplication inside one of the channels.

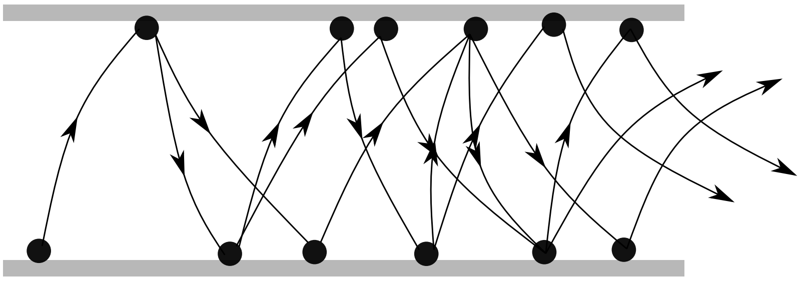

Figure 4.6.: Sketch of the electron multiplication in a MCP channel. Adapted from [149] and [162].

The total gain of a single MCP yields 10^3 to 10^4, but can be extended to 10^7 with a system of two or three MCPs. Thereby, the total gain is comparable to that of a dynode-based PMT. However, due to the electron multiplication inside the narrow channels, the difference in transit times is reduced dramatically from a few nanoseconds to less than 100 ps [156, 157], which is a great advantage. Another benefit of a microchannel plate compared to a PMT with a coupled scintillator is the possibility of a spatially resolved measurement by applying a seperate readout unit to every channel.

To avoid that ions generated by the electron cascade are accelerated to high energies in the opposite direction and for instance create additional electrons inside the chamber walls or at

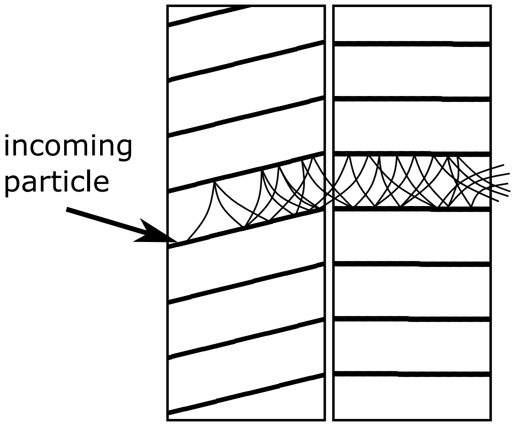

Figure 4.7.: Sketch of two MCPs in chevron configuration. The channels of the MCPs have an angle relative to each other avoiding the generation of secondary electrons by accelerated ions. Adapted from [149].

the photocathode, two MCPs can be used in the so-called *chevron configuration* [149, 156]. In this scheme, the MCPs are oriented in a way that their channels have a certain angle to each other, as it is shown in Figure 4.7. Thus, ions propagating through the channel get stopped inside the channel wall.

4.2.4 Gas chambers

Another method for the detection of particle radiation is the use of gas chambers. Typically, they are designed cylindrically with a wire in the center serving as the anode and the cylinder walls serving as a cathode. The electrons generated by the incoming radiation create an avalanche by collisions and thus cause a so-called *gas multiplication*.

The operation mode of a gas chamber depends on the applied voltage. Within a certain voltage range, the gas multiplication is linear and the detected signal is proportional to the number of electrons generated by the incoming radiation. One of the most commonly used gases for slow neutron detection is ^{3}He. Another possibility is the use of boron triflouride (BF_3). The gas usually is enriched with ^{10}B to increase the neutron detection efficiency. Such a detector serves as a neutron converter and a proportional counter at the same time [149]. The detection is limited by the *wall effect*, where a part of the incoming particles energy is deposited inside the cylinder walls instead of the gas.

4.2.5 Track-etch detectors

Plastic track etch detectors [164], such as CR-39, are another possibility to detect ionizing radiation. The charged particles (for neutron detection generated e.g. by proton recoil) leave a trace of radicals when propagating through the material by transferring their energy to the electrons. These traces can be made visible under a microscope by etching the material in a base solution [149], as the damaged tracks react more effectively than the parts which are intact [158]. After the etching process, the particle tracks have a diameter of about 10-20 μm [149].

As the particles need to have an energy loss above a certain threshold to produce a damage significant enough to generate an etchable track, these kind of detectors are insensitive to gamma rays or electrons. Light ions, such as protons or alpha particles, can only be detected by certain materials [149, 165]. However, as the measurement method of such a detector is non-electronical, it is insensitive to EMP. Together with its insensitivity to gamma rays, this is a great advantage for laser-driven neutron experiments.

4.2.6 Activation measurements

Neutron detection by activation is based on the formation of excited states after a neutron capture reaction and subsequent disintegration of the nucleus [149]. The emitted radiation can again be detected for example by one of the particle detectors mentioned in the previous sections. To achieve a high detection efficiency, chosen materials commonly have high neutron reaction cross sections to maximize the amount of generated secondary radiation. Materials with high (n,γ) cross sections are often used for the detection of slow neutrons because this reaction is more probable at low energies. Common examples are cobalt, rhodium, and gold. Reactions such as (n,α) or (n,p) can be used for high-energy neutrons because they usually have a reaction threshold in the range of 100 keV to several MeV [102]. Typical materials are copper, indium, and aluminum.

For the choice of an adequate detection material, the half-life of the excited state also is of importance. Very short half-lifes have the disadvantage of needing very fast read-out, whereas a long half-life leads to the difficulty of the sample or activation foil not having decayed to a sufficient degree before the start of the next measurement.

5 Maximization of the neutron yield and angular characterization

The experiments conducted over the last years have shown a maximum neutron yield of $1 \cdot 10^{10}$ n/sr [25] from a deuterated polymer target in combination with a beryllium catcher (cf. table 3.1) obtained at the Trident laser facility at Los Alamos National Laboratory (LANL), NM, USA. To verify the reproducibility of this result not only regarding the pitcher-catcher setup, but also concerning laser parameters, the first laser-driven neutron experiment at the PHELIX laser [29] at GSI Helmholtzzentrum für Schwerionenforschung, Darmstadt, Germany was conducted. The goal of this campaign was to study the reproducability of a laser-driven neutron source as well as to increase the maxmimum neutron yield. Another aim was the execution of an extensive study of the angular neutron distribution.

5.1 Experimental setup

The PHELIX laser at GSI is a high-energy short-pulse Nd:glass system providing a maximum energy of 250 J within minimal pulse lengths in the range of 500 fs. During the experiment, energies in the range of 173 to 220 J measured after the last amplifier were used. The maximum intensity on target can be calculated by the formula

$$I_{\max} = \frac{2E_{\mathrm{amp}} \cdot \eta_{\mathrm{tr}} \cdot \eta_{\mathrm{ab}} \cdot \eta_{\mathrm{foc}}}{\pi \omega_0^2 \Delta\tau} \tag{5.1}$$

with the pulse energy after the last amplifier E_{amp}, the transport efficiency from the amplifier to the target η_{tr}, a correction factor for on-shot abberations η_{ab}, the energy fraction within the beam waist η_{foc} as well as the radius of the beam waist ω_0 and the pulse length $\Delta\tau$. In reference [166], Wagner *et al.* give the following values for the PHELIX short-pulse configuration: $\omega_0 = 3.7\,\mu\mathrm{m}$, $\eta_{\mathrm{tr}} = 0.8$, $\eta_{\mathrm{foc}} = 0.25$, and $\eta_{\mathrm{ab}} = 0.62$. Together with the above given energy and pulse length during the experiment, this yields to intensities around $2 \cdot 10^{20}\,\mathrm{W/cm^2}$.

Figure 5.1 shows the setup of the experiment. With a f#1.5 off-axis parabola, the laser was focused on the polymer target accelerating ions from the foil. The incident angle of the laser on target was 10 ° (not shown in the sketch). In the first half of the experiment, ions from targets of different thicknesses were measured with a stack of RadioChromic Films (RCF) [167] and copper and nickel foils, respectively. In the second half of the experiment, the RCF stack was exchanged by a beryllium catcher to generate neutrons. The angular distribution of the neutrons was measured with bubble dosimeters (cf. section 4.2.1) fabricated by Bubble Technology Industries (BTI) [155]. They were placed at the outer target chamber wall (Figure 5.2 left) as well as at the shielding wall at about 1 m distance to the PHELIX vacuum chamber (Figure 5.2

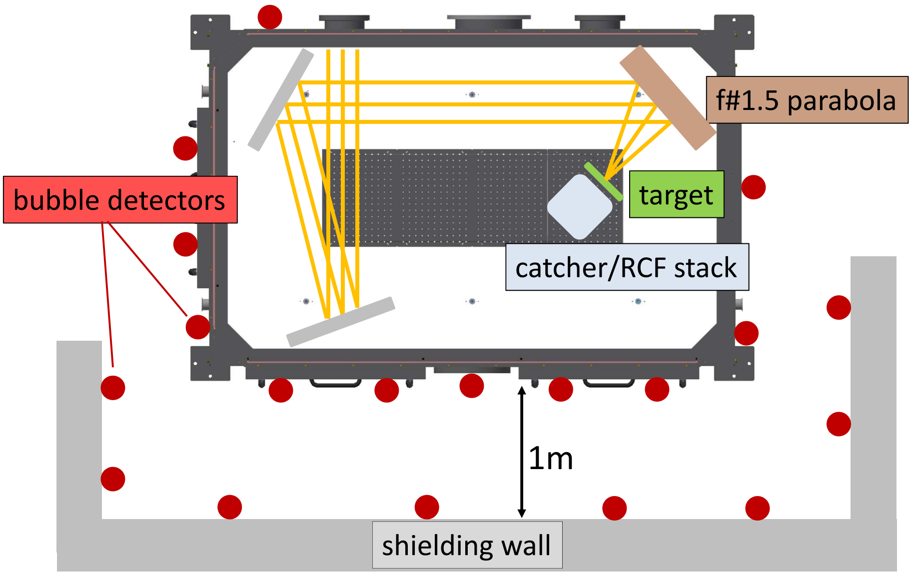

Figure 5.1.: Sketch of the experimental setup at the PHELIX laser. The laser was focused with a f#1.5 off-axis parabola onto a polystyrene target. The accelerated ions impinged a RCF stack for ion characterization or a cylindrical beryllium catcher from where neutrons were emitted. The angular distribution was measured with up to 30 bubble detectors placed at the outer target chamber wall and a steel shielding wall at 1 m distance to the vacuum chamber.

right). To be able to measure a detailed angular distribution, up to 30 bubble detectors were used simultaneously.

To measure the energy spectrum of the emitted neutrons, three time of flight detectors, each consisting of a liquid scintillator coupled to a photomultiplier [168], were positioned at different angles around the target chamber. However, despite considerable shielding of the detector and the readout device, the system was too sensitive to EMP and could not provide analyzable data.

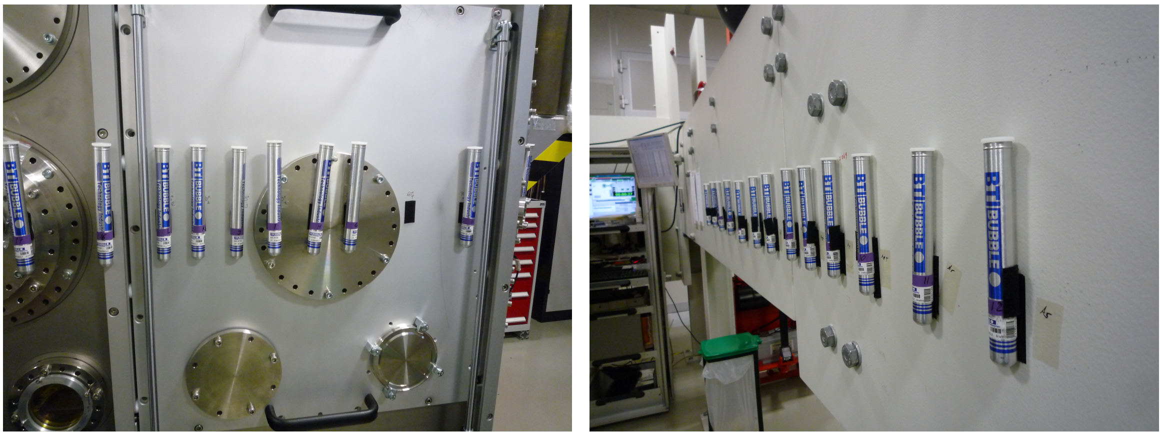

Figure 5.2.: Photographs of the bubble detector setup around the PHELIX vacuum chamber at the outer target chamber wall (left) and at the shielding wall (right).

The following sections will introduce several components of the experiment in more detail.

5.1.1 Targets and RCF stack

The laser was focused on thin deuterated polystyrene (CD) foils with approximate thicknesses between 400 and 1200 nm. To improve the accuracy of the thickness measurements for the individual targets, they were characterized by means of alpha energy loss with an ^{241}Am source. This technique was automated with a special setup at the target laboratory at Technische Universität Darmstadt. It provides the possibility of characterizing every individual target manufactured for an experiment compared to the interferometric method at TU Darmstadt that is only applicable while the foil is still on the substrate and not cut into single targets [169]. The interferometric method thus can only serve as a reference measurement, that is conducted on one foil of each manufactured batch. However, a disadvantage of the characterization by energy loss of alpha particles is that it does not provide any information about the surface structure of the target and presupposes that the thickness of the target does not change significantly over the measured area.

Due to the special granulated structure of the deuterated polystyrene supplied by the manufacturer that can be seen in Figure 5.3, the determination of a density proves to be very difficult as the measurement of the volume is very complicated. Furthermore, the manufacturer could not provide the chain lengths of the polymer. In addition, the target fabrication process with dissolving and spin-coating the solution could also effect the density of the deuterated polystyrene foil. These circumstances impede an accurate calculation of the target thickness from the alpha energy loss measurement. The most reliable possibility is thus a comparison of the targets in units of keV. For more detailed information on this subject, the reader is referred to references [169–171].

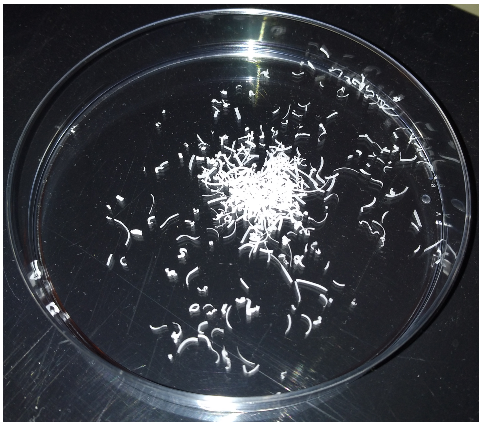

Figure 5.3.: Photograph of the polystyrene granulate supplied by the manufacturer.

Behind the deuterated polystyrene target, the accelerated ions were measured with a stack consisting of RCF as well as copper and nickel foils with thicknesses from 20 to 2000 μm. RCF are thin polymer dosimetry films that change their color from green to blue by the interaction with ionizing radiation, which results in an image of the radial ion beam profile on the RCF. Furthermore, the stack configuration allows to deconvolute an energy spectrum due to the energy loss of the ions in the individual films [172]. The copper and nickel foils were used for Nuclear Activation-based Imaging Spectroscopy (NAIS) [173] to complement the RCF measurement.

During the experiment at the PHELIX laser, the RCF stack was used to determine the maximum ion energy. A reconstruction of seperate deuteron or proton spectra from this diagnostic was not possible in this case because both ion species color the RCF and can not be distinguished afterwards. The calculated ion spectrum would thus contain both constituents.

5.1.2 Catcher

In the course of the experiment, the RCF stack was replaced by a beryllium catcher to convert the laser-accelerated ions into neutrons. As mentioned in section 3.3, beryllium has high cross sections for the conversion of protons into neutrons as well as (n,2n) reactions [102]. The catcher consisted of beryllium disks with thicknesses of 3, 6, and 12 mm with RCF and thin copper foils in between to simultaneously measure the maximum ion energy. It should be noted, that the energy resolution of the converter stack is much lower compared to the RCF stack especially designed for ion measurements. To minimize the number of ions that are not converted into neutrons, the stack was calculated to stop protons with energies up to 90 MeV and deuterons with energies up to 130 MeV.

To further increase the neutron yield in the forward direction, the beryllium was put inside a tungsten cylinder as can be seen in Figure 5.4. Tungsten is a material with high elastic scattering cross sections for neutrons of the order of several barn as well as high (n,xn) reaction cross sections in the range of 500 mb to 2 b for neutron energies of a few MeV up to several 10 MeV [102]. These processes lead to reflection and neutron emission back into the converter material. Thus, the number of high-energy neutrons which are laterally scattered out of the catcher decreases and the neutron yield of the forward directed beam is increased. Another material used for this purpose is brass. Copper and zinc both have high neutron scattering cross sections of a few barn, but compared to tungsten about an order of magnitude lower (n,xn) reaction cross sections with a higher threshold [102]. Nevertheless, brass is a suitable material to optimize the neutron yield in the forward direction.

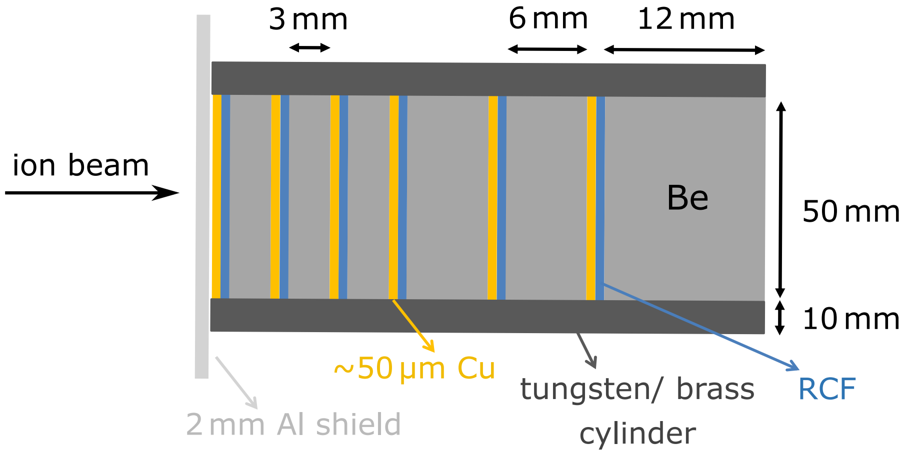

Figure 5.4.: Sketch of the sandwich-type catcher with beryllium disks of 3, 6, and 12 mm thickness and RCF for simultaneous ion energy measurements. The order of the beryllium disks serves as an example and was changed for different shots. The catcher was placed inside a cylinder made of either tungsten or brass with 1 cm wall thickness to increase the neutron yield in the forward direction.

Additionally, the catcher was shielded with a 2 mm aluminum plate and a 50 µm copper foil in the direction of the incoming ion beam to avoid a direct impact of the plasma from the laser-target interaction on the front beryllium disk and subsequent contamination of the vacuum chamber with beryllium dust or debris.

5.2 Experimental results

In the first half of the experiment, maximum ion energies were measured with a RCF stack. Ions accelerated from the deuterated polystyrene foils can possibly be protons, deuterons, carbon, and other constituents of the contamination layer on the backside of the target. As protons are the lightest ion species and the energy loss in a material according to the Bethe-Bloch formula (e.g. [174]) is proportional to the square of the charge number Z^2, their energy loss inside the RCF stack is lower compared to other ions. In addition, due to the more efficient acceleration of protons (cf. section 2.4), their maximum energy can be expected to be the highest. Thus, it can be assumed, that the maximum energy shown in the RCF corresponds to protons.

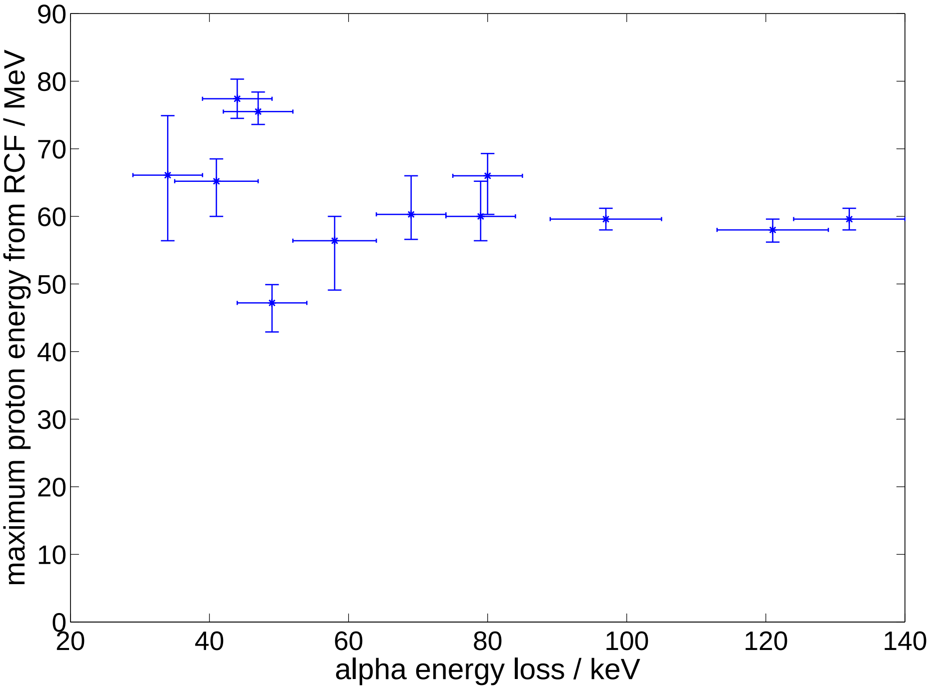

Figure 5.5.: Maximum proton energy from the RCF stack over alpha energy loss. The vertical error bars are given by the energy resolution of the particular RCF stack for each shot. The uncertainty of the energy loss is determined by the measurement during the target characterization.

Figure 5.5 shows the result of the ion characterization for different target thicknesses corresponding to the given values of alpha energy loss in units of keV. It can be seen, that the maximum proton energies lie mainly between 50 and 70 MeV and remain almost constant over the whole thickness range with a mean energy of (62.6 ± 7.9) MeV. The accuracy of the measurement is limited by the energy resolution of the RCF stack. In addition, uncertainties can originate from shot to shot variations of the laser energy or pulse length for example, that influence the ion acceleration from the target in complex processes (e.g. [175]), but are not included in the error bars of Figure 5.5.

These results indicate, that it is possible to achieve reproducible ion beams with the PHELIX laser, which is the basis for a dependable and stable laser-driven neutron source.

The neutrons originate from ion induced ^{9}Be(p,n)^{9}B and ^{9}Be(d,n)^{10}B reactions as well as from deuteron break-up inside the beryllium catcher. The angular distribution was measured with bubble detectors. The analyzing software displays the number of bubbles b, which can be transferred to neutron number per steradian N with the following formula:

$$N\left[\frac{1}{\mathrm{sr}}\right] = \frac{b\,(d[cm])^2}{cs} \tag{5.2}$$

with the calibration for each detector c given in bubbles per mrem and the bubble detector sensitivity s for a detector with a calibration of 1 bubble per mrem displayed in Figure 4.3. Because the neutron spectrum is unknown, s was set to a mean value of $(3 \pm 0.4) \cdot 10^{-5}$ bubbles per neutron and cm^2 for 1 bubble per mrem over the whole energy range.

As the distances and angles of the bubble detectors were measured with respect to the deuterated polystyrene target, they had to be corrected to match the position of the neutron source, which was assumed to be in the center of the beryllium catcher.

A detailed measurement of the angular neutron distribution is exemplarily displayed in Figure 5.6. It shows a strong maximum in the forward direction with $(1.35 \pm 0.24) \cdot 10^{10}$ n/sr, which is up to an order of magnitude more than the neutron yield in the sideways and backward directions. This directed neutron beam originates from pre-equilibirum reactions and deuteron break-up (cf. section 3.2) as well as the special catcher design with a tungsten cylinder around the beryllium. In addition to the neutron yield, the detailed measurement with 27 bubble detectors simultaneously allows to identify an opening angle of the neutron beam, which is $\vartheta/2 = (50 \pm 2)^\circ$ at half maximum (HWHM).

During the experiment, a neutron yield of $(1.42 \pm 0.25) \cdot 10^{10}$ n/sr in the forward direction corresponding to a measured dose of (43 ± 5) mrem or (430 ± 50) μSv could be achieved, which is an increase of 40 % compared to the highest neutron numbers from a laser-driven neutron source reported so far [25].

The total neutron yield of Figure 5.6 adds up to $\left(6.55 \cdot 10^{10} \pm 7.97 \cdot 10^{7}\right)$. It was calculated by integration over the solid angle Ω, which was split into two steps. First, the integration over all angles ϑ relative to the laser forward direction, resulting in a horizontal angular neutron distribution in the laser plane. Second, the rotation of the obtained distribution. The integration over ϑ was realized by applying a linear interpolation to the data with a step width of $\Delta\vartheta = 0.01^\circ$. As the interpolation values are discrete, the integral transforms into a sum:

$$N_{\mathrm{tot}} = \int N(\vartheta)d\Omega = \int_0^{2\pi}\int_0^{\pi} N(\vartheta)\sin\vartheta\, d\vartheta\, d\varphi = \int_0^{2\pi}\sum_{\vartheta_i=0}^{\vartheta_i=\pi} N(\vartheta_i)\cdot\Delta\vartheta\sin\vartheta_i\; d\varphi. \tag{5.3}$$

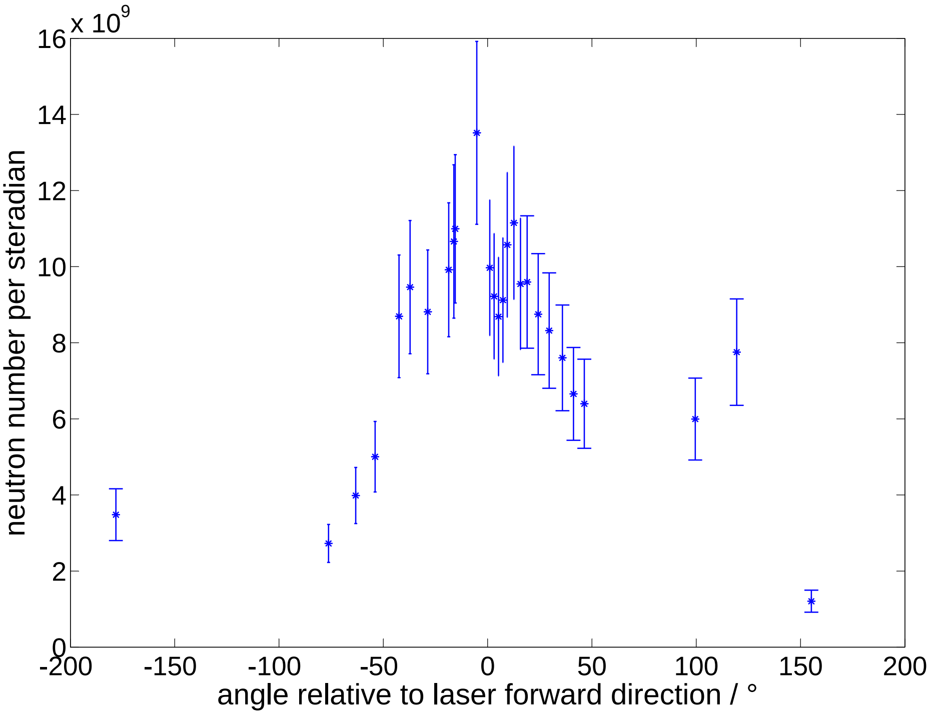

Figure 5.6.: Detailed angular neutron distribution from a CD target and a beryllium catcher measured with 27 bubble detectors simultaneously at the PHELIX laser system. For clarity reasons, the angle uncertainty of 2 ° is not shown in the graph.

Assuming that the neutron distribution is rotationally symmetric and thus independent of φ, the corresponding integral can easily be solved. However, the measured neutron distribution shows an asymmetry around the rotation axis (laser forward direction). To account for that, the angular distribution was only summed on one side of the rotation axis at a time and divided by 2. The total neutron number yields from the summation of the results for both sides

$$\begin{aligned} N_{\text{tot}} &= \frac{1}{2}\left[2\pi\Delta\vartheta \cdot \sum_{\vartheta_i=-180^\circ}^{\vartheta_i=0^\circ} N(\vartheta_i)|\sin\vartheta_i| \;+ 2\pi\Delta\vartheta \cdot \sum_{\vartheta_i=0^\circ}^{\vartheta_i=180^\circ} N(\vartheta_i)\sin\vartheta_i\right] \\ &= \pi\Delta\vartheta \sum_{\vartheta_i=-180^\circ}^{\vartheta_i=180^\circ} N(\vartheta_i)\cdot|\sin\vartheta_i|. \end{aligned} \tag{5.4}$$

As can be derived from Figure 5.6, the uncertainty of the neutron number per steradian is about 20 %. Thus, the uncertainty of the total neutron number can be calculated with

$$\Delta N_{\text{tot}} = \sqrt{\sum_i \left(\frac{\delta N_{\text{tot}}}{\delta N_i}\Delta N_i\right)^2} = 0.2\pi\Delta\vartheta\sqrt{\sum_{\vartheta_i-180^\circ}^{\vartheta_i=180^\circ}\left(N(\vartheta_i)\cdot|\sin\vartheta_i|\right)^2} \tag{5.5}$$

and is of the order of 10^7. Figure 5.7 displays the calculated total neutron yield of every shot with a catcher behind the target. It shows, that nearly constant neutron numbers around a mean value of $5.25 \cdot 10^{10}$ neutrons per shot with a standard deviation of $0.77 \cdot 10^{10}$ could be obtained during the whole experiment. The uncertainties of the single shot measurements are three orders of magnitude less and thus not displayed in the diagram.

The results of the experiment at the PHELIX laser demonstrate the reliability and reproduciblity of a laser-driven neutron source with constantly high neutron numbers and a distinctly forward directed neutron beam. Both characteristics form the basis for the feasibility of different laser-driven neutron applications in the future.

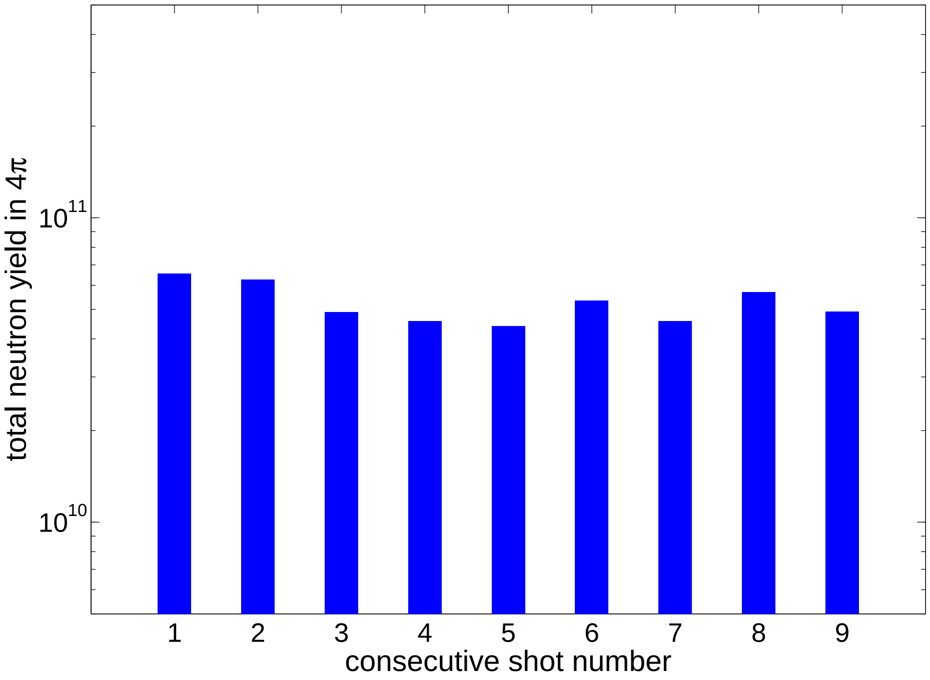

Figure 5.7.: Total neutron yield for every shot of the experiment with a catcher behind the primary target.

6 Experiments on neutron moderation and neutron resonance spectroscopy

As already mentioned, a laser-driven neutron source provides an exponentially decaying energy spectrum (cf. section 3.4) with cut-off energies of several 10 MeV depending for example on different laser parameters, such as intensity or contrast, target and catcher materials as well as the geometry of the experimental setup. Nevertheless, applications like neutron resonance spectroscopy require a high neutron flux at epithermal energies in the range between 0.1 eV and 100 keV [114, 156].

Based on the explanations and conclusions in section 3.6 as well as the promising experimental results shown in the last chapter, several experimental campaigns were conducted to measure the moderated neutron spectrum from a laser-driven source and test its feasibility for NRS. The experiments were executed at the Trident laser facility at Los Alamos National Laboratory (LANL), NM, USA. The Trident laser is a Nd:glass system that provides a short-pulse CPA beam with an energy up to 120 J corresponding to about 80 J on target within a pulse length of 500 fs. Due to the small focus at Trident, this yields to intensities of more than 10^{20} W/cm^2.

6.1 First measurements on neutron moderation

As a first step to applications with low-energy neutrons, the successful moderation of a laser-driven neutron spectrum is to be shown. First measurements with a very simple geometry were conducted at target area north (TA North) at Trident. The experimental setup is illustrated in Figure 6.1a. The laser was focused on sub-micrometer deuterated polystyrene foils, which were characterized with an ^{249}Am source by means of alpha energy loss, as it is described in section 5.1.1. The accelerated ions (mainly protons and deuterons) impinged a cylindrical lithium deuteride catcher with a diameter of 5 cm and a length of 5 cm. A graphite moderator shown in Figure 6.1b with a total length of 17.8 cm was placed directly behind the catcher to moderate neutrons in the forward direction. Neutron time of flight (nToF) as well as bubble detectors (cf. section 4.2.1) were arranged at different angles around the target chamber.

The nToF detectors were operated with NE-102 plastic scintillators coupled to fast photomultiplier tubes (PMT). For the two detectors placed in the backward and sideward directions, a Hamamatsu R1250 PMT was used. However, as mentioned in section 4.2.2, this detector system is very sensitive to gamma rays, causing an overlap with the neutron signal. For that reason, the nToF detector in forward direction contained a Photonis XP4362B PMT, which resulted in well distiguishable neutron spectra.

The result of a moderated nToF spectrum (red) compared to a reference measurement without a moderator (blue) is displayed in Figure 6.2a. Both spectra were obtained with the Photonis XP4362 PMT placed at a distance of 6 m from the neutron source in the forward direction. It is

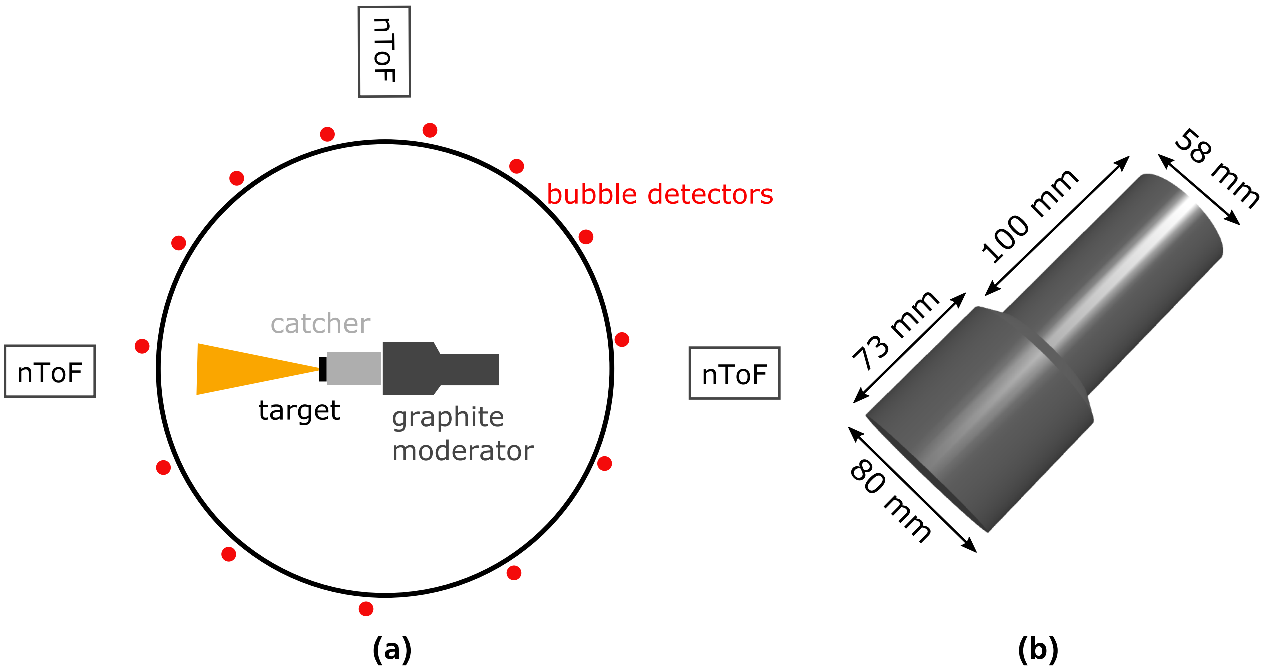

Figure 6.1.: (a) Sketch of the experimental setup of the first moderation measurements conducted at Trident TA North at LANL. A 17.8 cm long graphite moderator was placed directly behind the lithium deuteride catcher. Bubble detectors (red dots) and neutron time of flight (nToF) detectors were placed at different angles around the target chamber. (b) Geometry and dimensions of the used graphite moderator.

apparent, that the neutron numbers up to energies around 25 MeV are lower when a moderator is placed into the beam. However, high-energy neutrons above 30 MeV are not affected by the moderator as can be seen by the two curves merging at the mentioned energy. Moderated neutrons are scattered to the sideward directions, which is confirmed by the angular neutron distribution measured with bubble detectors displayed in Figure 6.2b. Compared to a shot without moderator (cf. e.g. fig. 5.6), it is clearly visible that the forward pointing neutron beam is directed sideways due to the moderating material in the beam path. The angular distribution shows a local minimum in the forward direction and pronounced maxima at ±45 °.

The shown results were obtained with detectors that are sensitive to high-energy neutrons. However, they indicate two important behaviors: first, neutrons that are moderated get scattered away from the laser axis to the sideward directions and second, neutrons with very high energies of the order of several 10 MeV are not affected by the moderator and remain on-axis. From these points, it can be derived that it is advantageous to set up a detector for NRS measurements in one of the sideward directions. As moderated neutrons are scattered in these directions, the low-energy neutron flux will be higher. Furthermore, the moderator thickness causes a temporal spread of the neutron pulse, which can more easily be kept narrow in the sidward directions compared to the forward direction. In addition, the latter can simultaneously be used for high-energy neutron measurements or even be shielded to reduce the radiation exposure during the experiment, which is a great advantage especially in small facilities where space for shielding is limited.

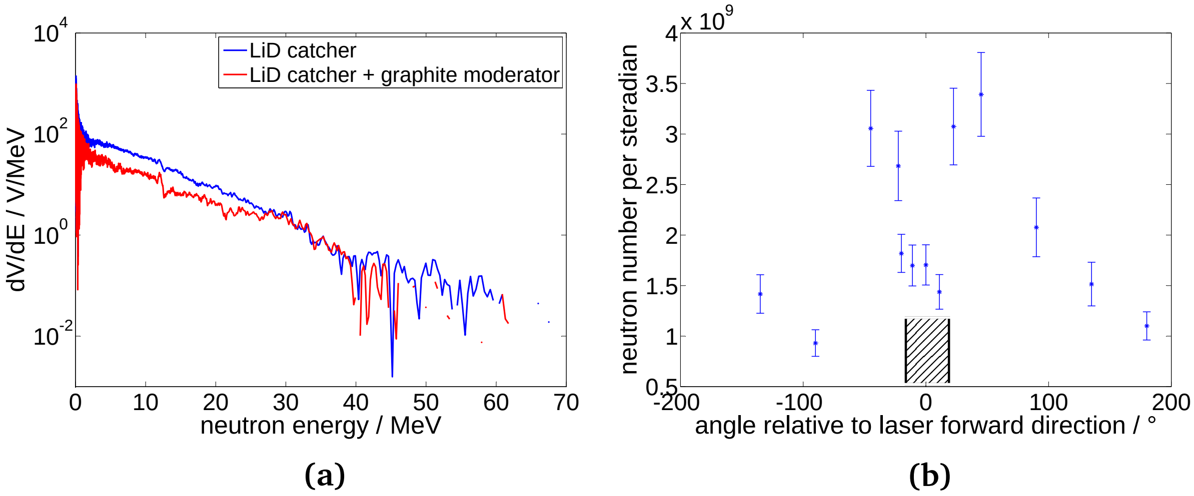

Figure 6.2.: (a) Comparison of nToF spectra from a reference shot without moderator (blue) and a shot with a graphite moderator (red). The measurements were conducted in the forward direction. (b) Angular neutron distribution with the graphite moderator behind the catcher measured with bubble detectors. As a guide for the eye, the shaded area marks the angular range covered by the moderator.

6.2 Optimization of the moderator and proof of principle NRS measurements on a static ^{115}In sample

After the first measurements of high-energy neutrons with a moderator behind the catcher, a dedicated experiment on neutron moderation and resonance spectroscopy was conducted at the new target area west of the Trident laser facility. During this campaign, the laser-generated neutrons were moderated to thermal and epithermal energies and measured with a set of different high-energy as well as low-energy detectors. One of the main diagnostics was a boron-doped microchannel plate (MCP) detector, that was set up to measure neutrons at epithermal energies and especially the 1.46 eV resonance of a thin indium sample (cf. Figure 3.7).

Indium was chosen for the low central energy and the broad width of the resonance as well as its high neutron reaction cross section with a maximum of more than 30 kb at 1.46 eV. These requirements are important for the detection efficiency and resolution. The efficiency of the boron-doped MCP decreases rapidly with increasing energy and at 1 eV has already lost more than one order of magnitude compared to the efficiency at 25 meV [176]. This can be counterbalanced by a high reaction cross section of the resonance and a central energy as low as possible. The temporal resolution of the detector as well as due to experimental conditions requires the choice of a resonance with a width above the resolution limit.

A sketch of the experimental setup is shown in Figure 6.3. The short-pulse CPA laser was focused onto a thin deuterated polystyrene target by a f#1.5 off-axis parabola to accelerate intense proton and deuteron beams. The CD targets with thicknesses corresponding to an alpha energy loss between 33 and 80 keV, were characterized with a ^{241}Am source as it was described in section 5.1.1.

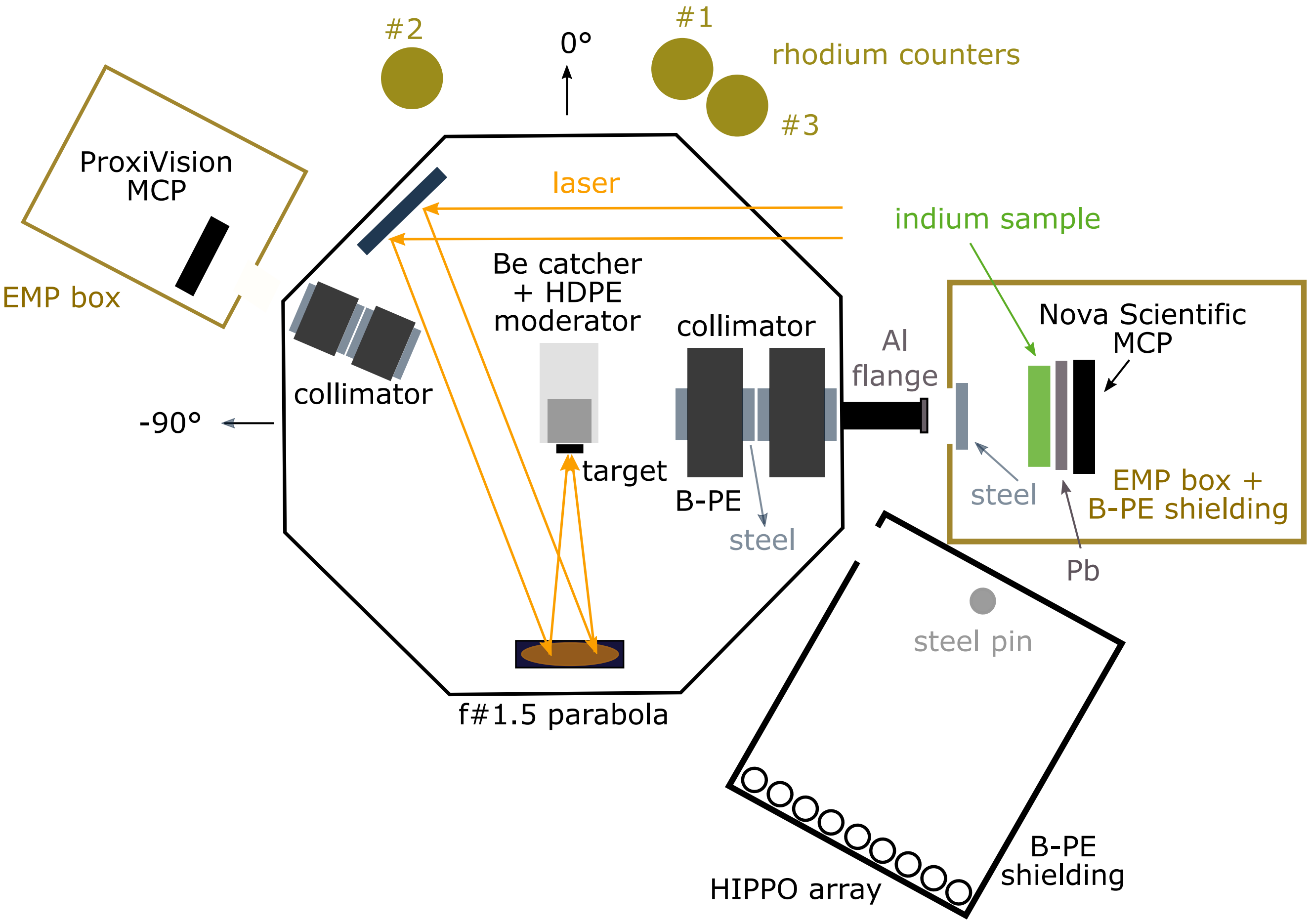

Figure 6.3.: Sketch of the fractional setup for the NRS measurement with corresponding angles. Shown are the two boron-doped MCP detectors from ProxiVision at -67.5 ° and from Nova Scientific at 90 °. In addition, rhodium counters in the forward direction and a ^{3}He detector array (HIPPO) were installed for reference measurements of thermal and epithermal neutrons.

After a distance of 30 mm, the accelerated ions impinged the front surface of a beryllium catcher, that was shielded with 25 μm aluminum and 15 μm kapton to avoid direct impact of plasma from the laser-target interaction. Additionally, the catcher had a 15 mm deep and 15 mm wide hole drilled into the surface facing the incoming ion beam. Thus, neutrons scattered into the backward directions could partially be reflected at the inner walls of the beryllium cylinder and contribute to the total neutron yield usable for the planned measurements of this campaign.

The beryllium catcher was placed inside a high density polyethylene (HDPE) block to moderate the emitted neutrons. Compared to the experimental setup introduced in the previous section, where the moderator was placed behind the catcher, the configuration used in this experiment has the advantage of a much higher neutron number entering the moderator. Its design was planned to be long in the direction of the incoming ions flight path to moderate as many high-energy neutrons as possible. However, as described in the previous section, even with moderator thicknesses of a few 10 cm the most energetic neutrons of the spectrum will not be slowed down enough to reach thermal or epithermal energies, but remain in the high-energy region. In addition, the moderator dimensions in line of sight to the sample have to be small because a thick moderator would cause a wide temporal spread of the neutron pulse. Thus, if the sample

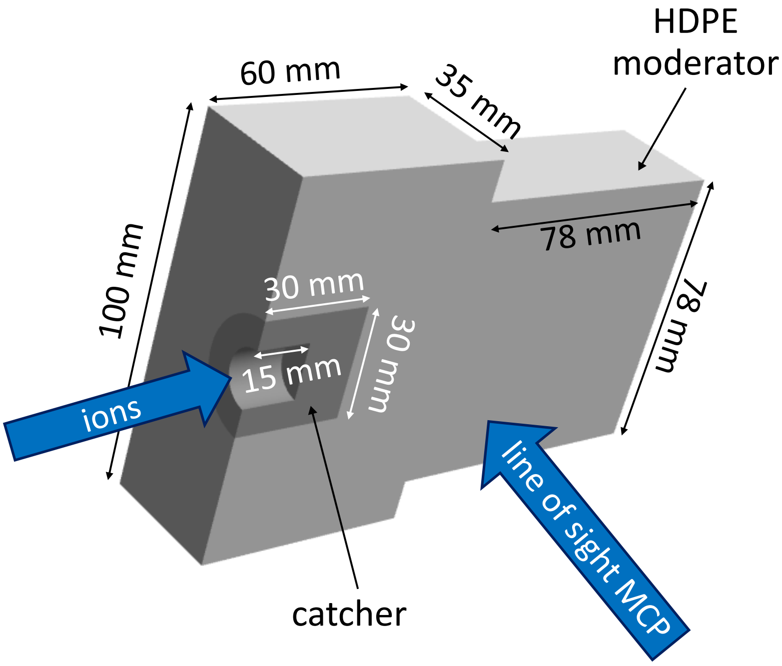

Figure 6.4.: Sketch of the HDPE moderator and the beryllium catcher, which had a hole drilled into it to reflect backscattered neutrons.

would be placed in the forward direction, the epithermal neutron pulse would be very long, if a considerable amount of high-energy neutrons is to be moderated. For these reasons, the resonance measurement of the indium sample was arranged to be perpendicular to the forward direction.

Figure 6.4 shows the design of the catcher and HDPE block. The moderator thickness in line of sight to the indium sample was 7 cm. The flight path difference of two neutrons to the detector is maximal, when considering the neutrons starting from opposite surfaces of the moderator in line of sight to the detector. Assuming no further scattering, this yields to a maximum temporal spread of 4.2 µs on the detector corresponding to an energy spread of 0.11 eV, which has a significant influence on the width of the ^{115}In resonance of approximately 0.01 eV [102, 177].

To collimate the produced neutrons, a stack of alternating steel and boron-treated polyethylene (B-PE) layers with a hole in the middle for neutrons on-axis to the sample to pass was placed inside the target chamber between the indium sample and the neutron source. Steel has constantly high neutron scattering cross sections of 13 b in an energy range from 5 meV to 200 eV and thus scatters low-energy neutrons not passing through the hole either further away from the axis or back into the beam. The following boron-doped polyethylene block captures the scattered neutrons with a (n,α) reaction. Hence, only neutrons with a small divergence directly on-axis between the neutron source and the detector can pass the collimator. The vacuum chamber in line of sight to the indium sample was closed with a 3 mm aluminum flange instead of the standard 5 mm steel flange to reduce the interaction with the neutron beam.

The main diagnostics for measuring the ^{115}In resonance were two boron-doped MCP detectors at 90 ° and -67.5 ° with respect to the laser forward directon, which is defined as 0 °. The detector at 90 ° was a boron and gadolinium-doped MCP from Nova Scientific [178] with a sensitive area of 28 mm in diameter [146, 163]. The system had a temporal resolution of 640 ns. It was placed at a distance of (1.67 ± 0.1) m to the neutron source, which was assumed to be in the center of the moderator, inside a brass box to shield it from EMP. The entrance hole of the box was in line with the collimator holes as well as the aluminum flange and was surrounded by steel with a thickness of 2.5 cm reaching roughly 10 cm in radial direction. Furthermore, the MCP was shielded by thick boron-treated polyethylene to all sides, except the line of sight to the neutron source, to avoid detection of neutrons scattered from the building walls or from other components inside the target area. The electronics were shielded with 5 cm of lead. In addition, a 3 mm lead foil was placed directly in front of the microchannel plate because of its high sensitivity to low-energy gamma rays in the range of a few hundred keV. When the indium sample in front of the detector is activated with neutrons, an In(n,γ) reaction with gamma energies of several 100 keV occurs [179]. The use of a thin lead foil reduces the distortion of the neutron spectrum by gamma rays, whereas the influence on the neutron spectrum itself is kept comparably low.

The boron- and gadolinium doped MCP detector at -67.5 ° was provided by ProxiVision GmbH [180] and had a sensitive area of 40 mm diameter, which is larger compared to the Nova Scientific MCP. It could digitally be set to temporal resolutions between 1 and 10 µs. Like the other detector, it was shielded with thick blocks of boron-treated polyethylene to all directions except the one of interest and placed inside an EMP shielding box. The MCP had a distance of (1.52 ± 0.05) m from the neutron source.

In addition, several other detectors were arranged around the vacuum chamber to provide a number of different reference measurements. For a comparison of the high-energy neutron yield and the analysis of the angular neutron distribution, bubble detectors (cf. section 4.2.1) were placed at the outer target chamber wall in different directions as well as next to important diagnostics. A neutron time of flight detector was placed in the forward direction at a distance of 6 m to the source. The detector was a Photonis XP4362B PMT coupled to a NE-102 plastic scintillator and thus gave a reference of the high-energy neutron spectrum.

A set of three rhodium counters [181] was used to determine the neutron flux for high as well as low energies in different directions. The measurement of different energy intervals was realized by a cadmium shielding around two of the detectors, that efficiently captures low-energy neutrons up to several 10 eV and thus provides an estimate of the high-energy component of the neutron spectrum. By correlation of the three counters, it is possible to analyze the number of low-energy neutrons. The detectors are based on the activation of a Rh foil by neutrons and subsequent detection of electrons with a PMT after a β^- decay.

Another reference for the number of thermal and epithermal neutrons was the HIPPO detector consisting of a steel pin and an array of ^{3}He tubes aligned to detect neutrons scattered by the pin and thus not directly in line of sight to the neutron source (cf. Figure 6.3). Like all low-energy neutron detectors, it was surrounded by massive boron-treated polyethylene shielding.

6.2.1 Results and discussion

To evaluate the efficiency of the moderator, several measurements with the moderator inside the vacuum chamber were compared to a spectrum obtained without the moderator. Neutron time of flight spectra could be obtained with the two boron-doped MCP detectors without an indium sample in front of the detector. This configuration will henceforth be called *open beam*.

For the analysis of the results from the Nova Scientific MCP, the recorded time of flight data was converted to energy and devided by the reaction propability of a neutron with the boron atoms in the MCP obtained with the following formula:

$$W_{\mathrm{R}} = 0.01 \cdot \frac{\sigma}{A} \cdot N_{\mathrm{R}} = 0.01 \cdot \frac{\sigma \rho \, d \, N_{\mathrm{A}}}{M}. \tag{6.1}$$

Here, σ represents the total reaction cross section of ^{10}B with neutrons, d the MCP thickness corresponding to pure boron, A is the surface of the interaction region, and $N_{\mathrm{R}} = \rho \, V \, N_{\mathrm{A}}/M$ represents the number of reacting boron atoms with mass density ρ, volume V, the Avogadro constant N_{A}, and molar mass M. The calculation of the detector efficiency based on the boron reaction cross section is a good approximation, because the cross section is one order of magnitude higher compared to that of gadolinium in the energy interval of interest. In addition, the fraction of gadolinium inside the MCP is much lower than the one of boron.

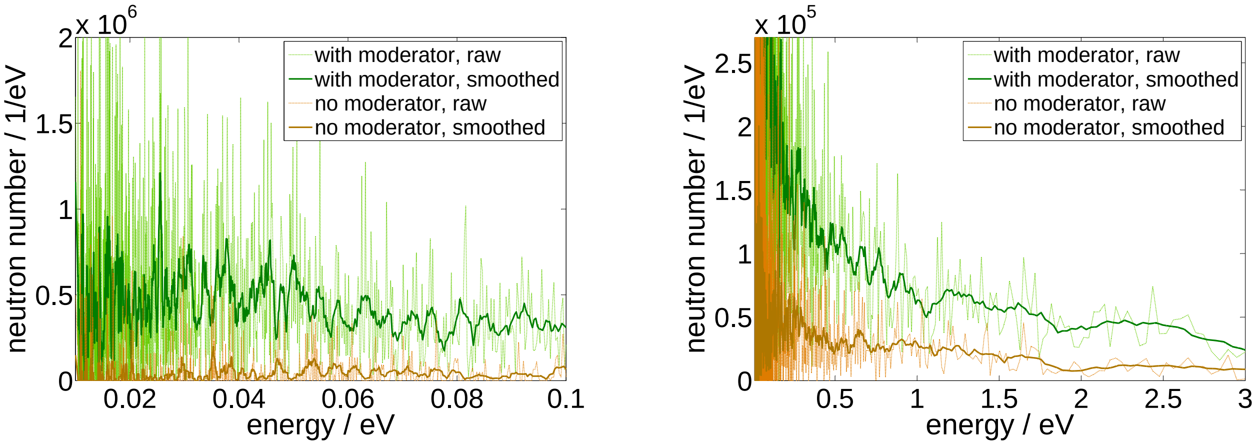

(a) **(b)**

Figure 6.5.: Comparison of exemplary measurements with (green) and without (brown) a moderator displayed for (a) thermal energies and (b) an energy range around the indium resonance at 1.46 eV. The data was obtained with the boron-doped MCP detector from Nova Scientific [146, 163]. Dotted lines show the raw signal, which was smoothed with a moving average over 10 data points (solid lines).

The neutron spectra with and without moderator obtained with the Nova Scientific MCP are shown in Figure 6.5 for the two different energy intervals of interest, namely thermal

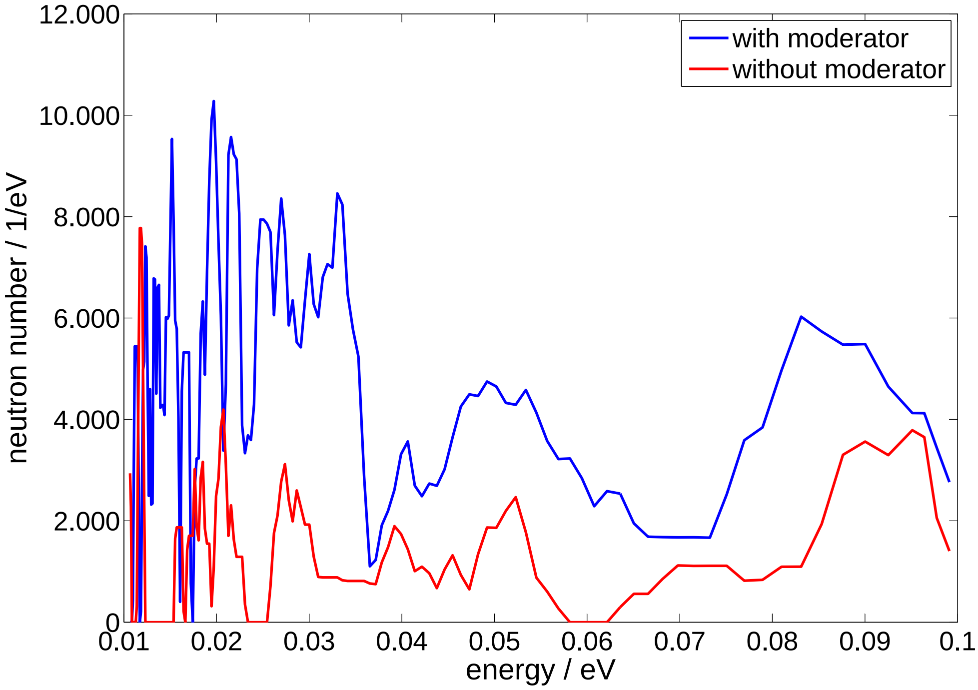

Figure 6.6.: Comparison of the neutron yield in the thermal energy range with (blue) and without (red) a moderator for the same shots as displayed in Figure 6.5. The data was obtained with the ProxiVision MCP detector.

neutrons (a) and neutrons with energies around the indium resonance at 1.46 eV (b). Dotted lines represent the raw data that is considerably fluctuating, which is why a moving average over 10 data points (solid line) was applied as smoothing. The effect of the moderator in both energy regions is clearly visible. At 1.5 eV the difference amounts to a factor 3 more neutrons with the moderator. At the thermal energy of 25 meV the moderator yields one order of magnitude more neutrons compared to a sole catcher.

As a comparison to these results, Figure 6.6 displays a measurement within the thermal energy range obtained with the ProxiVision detector placed at -67.5 °. The resolution was set to 5 µs. The neutron yield around the thermal energy of 25 meV shows an increase from a factor 2 up to one order of magnitude with a moderator in the setup. These values are consistent with the ones obtained with the Nova Scientific MCP.

Regarding neutron numbers, measurements with the HIPPO detector and the rhodium counters provide an independent comparison to the results obtained with the two MCP detectors. Without moderator, the HIPPO detector yielded 2878 counts integrated over all energies, whereas the yield for the measurement with moderator was 4099 counts, which is an increase of a factor of more than 1.4. The neutron numbers obtained with the rhodium counters at the time of the shot are summarized in table 6.1. Detectors #2 and #3 were additionally shielded with cadmium and thus were only sensitive to moderate (a few 100 keV) and fast (>1 MeV) neutrons. A comparison of the ratio of detector #1 without cadmium shielding with #2 and #3, respectively, shows an increase of the low-energy neutron number for the setup with a moderator.

moderator	counts #1	counts #2	counts #3	$\frac{\#1}{\#2}$	$\frac{\#1}{\#3}$
yes	8091	6814	19316	1.19	0.42
no	7869	10339	21196	0.76	0.37

Table 6.1.: Summary of the Rh counter measurements starting at the time of the laser shot. The measurement time was 60 s. The counters are labeled the same as in Figure 6.3. Detector #1 had no Cd shielding and was thus additionally sensitive to the low-energy component of the neutron spectrum.

With an increased neutron yield in the epithermal range, the neutron resonance spectroscopy on an indium sample could be conducted. The results presented in the following all were obtained with the MCP detector placed at 90 °. The readout system of the ProxiVision detector was not adapted to measurements in the energy range of the indium resonance, which prevents a comparison of transmission spectra from the two detectors.

As a reference for the NRS measurements, open beam measurements with otherwise identical experimental conditions were conducted. An example of a single shot neutron spectrum is shown in Figure 6.7. The raw signal (dotted line) was smoothed with a moving average over 10 data points (solid line). The neutron numbers are rapidly decreasing with energy up to approximately 1 eV. After that, the slope starts to flatten. The curve progression shows a continuous exponential decreasing behavior.

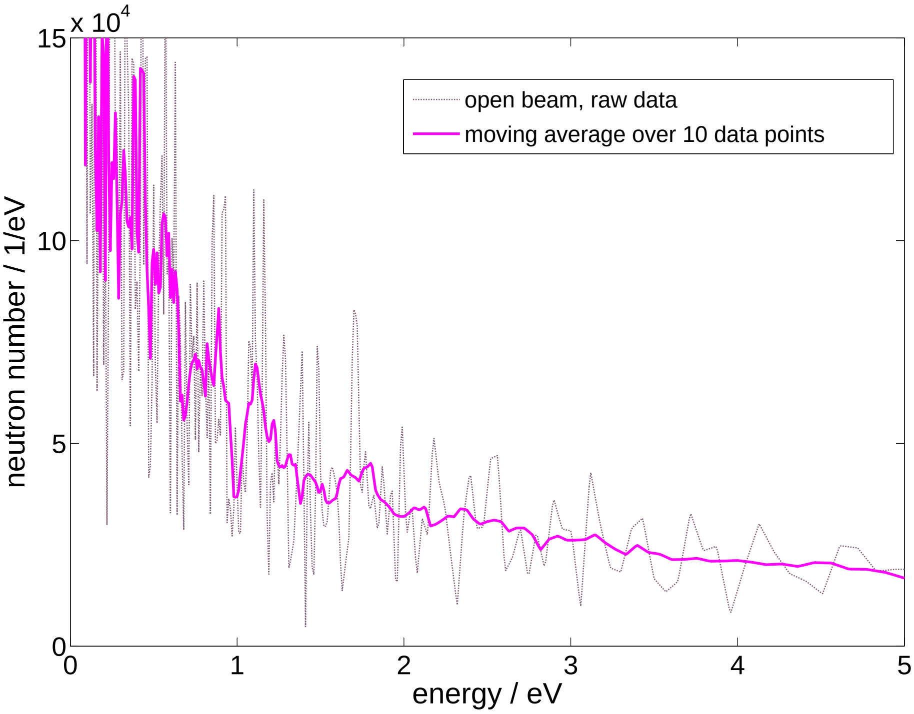

Figure 6.7.: Energy spectrum of an open beam measurement (dotted line). The signal was smoothed by applying a moving average over 10 data points (solid line).

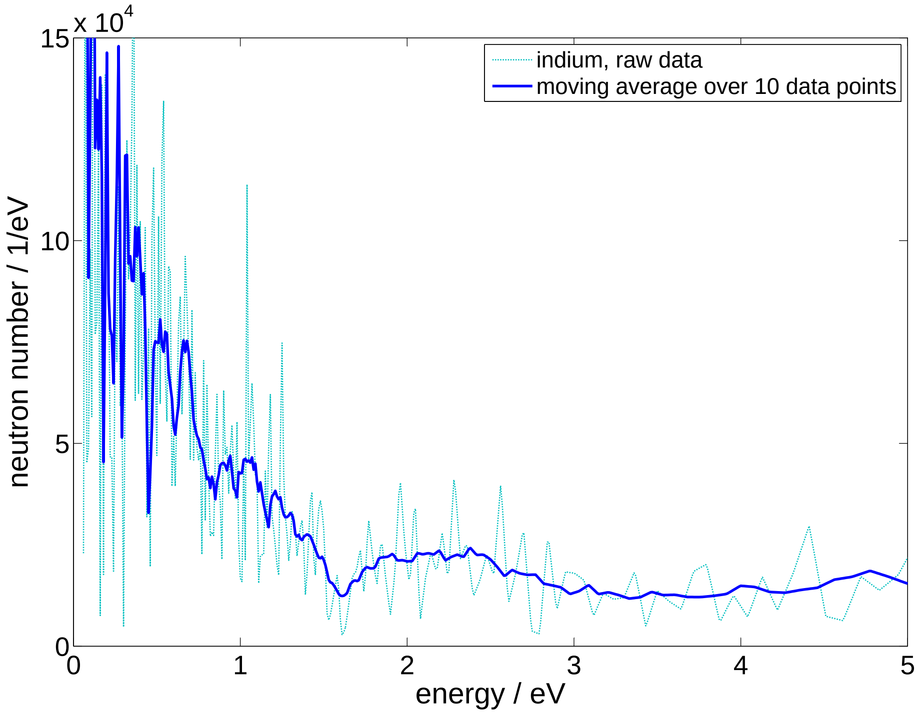

Figure 6.8.: Single shot measurement of the neutron spectrum (dotted line) conducted with the boron-doped MCP detector placed at 90 ° with a 5 mm ^{115}In sample directly in front of the detector. The solid line represents a smoothing of the dotted curve by a moving average over 10 data points.

Figure 6.8 displays the result of a single shot measurement with a 5 mm thick indium sample placed directly in front of the detector, which was shielded with 3 mm of lead. The transmission spectrum is exponentially decaying up to an energy of 0.7 eV. Afterwards, in contrast to the behavior in Figure 6.7, the neutron yield starts to decrease into a distinct negative peak, before rising again with increasing energy and merging into the exponential behavior. The negative peak has a central energy of (1.61 ± 0.19) eV and a full width half maximum (FWHM) of (0.25 ± 0.16) eV. A discussion of these values will be given in the following passages.

The width and position of the peak were determined by a Breit-Wigner (or Lorentzian) fit function. As explained in section 3.6, this is the theoretical form of a resonance in a scattering or capture reaction cross section. The resonance in a measured transmission spectrum is broadened by several effects. However, due to the low signal to noise ratio in the data, a determination of the width including all these effects would exceed the accuracy of the measurement. For that reason, the width is only calculated with the theoretical approach and the different causes for broadening are included in the uncertainty calculation.

The Lorentzian fit function is defined as

$$f(E) = \frac{a}{(E-b)^2 + c^2/4} + d. \tag{6.2}$$

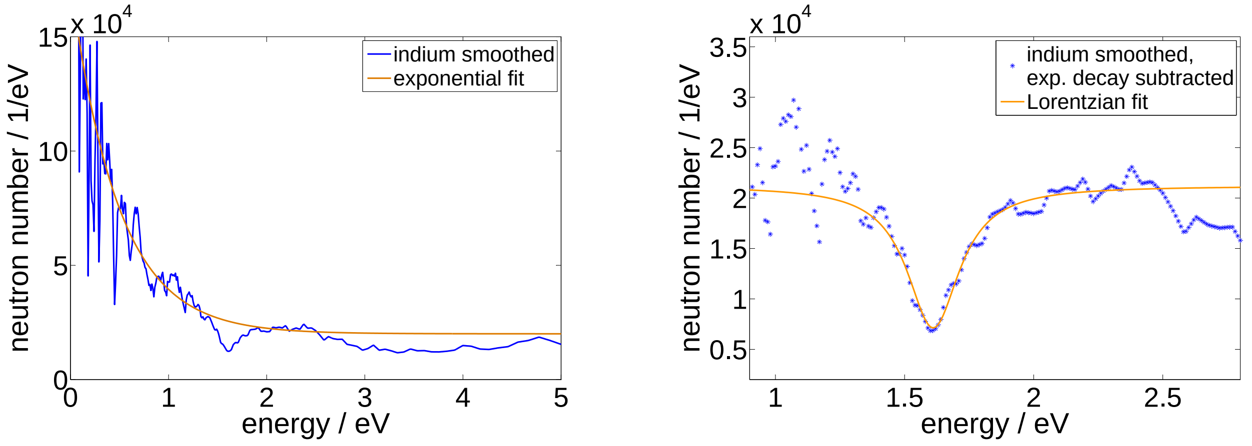

(a) **(b)**

Figure 6.9.: (a) Exponential fit to the neutron spectrum $f_{\text{exp}}(E) = A \cdot e^{-BE} + C$ with parameters $A = (1.541 \pm 0.157) \cdot 10^5\,\text{eV}^{-1}$, $B = (2.070 \pm 0.234)\,\text{eV}^{-1}$, and $C = (2.003 \pm 0.205) \cdot 10^4\,\text{eV}^{-1}$. (b) Enlargement of the negative peak shown in Figure 6.8 with subtracted fit of the exponential decay and shift by C as it is described in the text. The dots show the smoothed data of the result. The resonance was fitted with the Lorentzian function given in equation (6.2) (solid line).

To eliminate the influence of the exponential decay on the parameters, it was excluded by subtraction of an exponential fit $f_{\text{exp}}(E) = A \cdot e^{-BE} + C$ to the spectrum, which can be seen in Figure 6.9a. Afterwards, the resulting neutron numbers were shifted by the offset C of the fit function.

The application of a Lorentzian fit to the result yields the following fit parameters:

$$\begin{aligned} a &= -(217.5 \pm 41.0)\ \text{eV} \\ b &= (1.611 \pm 0.005)\ \text{eV} \\ c &= (0.2485 \pm 0.0235)\ \text{eV} \\ d &= (2.121 \pm 0.046) \cdot 10^4\ \text{eV}^{-1}. \end{aligned} \tag{6.3}$$

The parameters b and c represent the position and the width of the negative peak. Figure 6.9b displays an enlarged energy range around the negative peak including the subtraction of the exponential fit and the shift due to the offset parameter C (dots). The Lorentzian fit is represented by the solid line.

The position of the central energy has an uncertainty which on the one hand is determined by the uncertainty of the distance measurement from the detector to the source. As can be deduced from Figure 6.3, the setup was quite complicated with tightly packed components leading to the necessity of a sectional distance measurement. As a result, the uncertainty of the distance was estimated to be 10 cm corresponding to an energy uncertainty of $u_{\text{d,E}} = 0.18\,\text{eV}$. On the other hand, the time resolution of the detector system, which yields 640 ns, leads to an additional energy uncertainty of $u_{\text{t}} = 0.04\,\text{eV}$. These two factors yield a total systematic position error of $u_{\text{sys,pos}} = \sqrt{u_{\text{d,E}}^2 + u_{\text{t}}^2} = 0.18\,\text{eV}$.

causes	width	position
distance source to detector	0.01 eV	0.18 eV
time resolution of detector	0.04 eV	0.04 eV
moderator thickness	0.11 eV	-
Doppler effect	0.08 eV	-
uncertainty of fit parameters	0.02 eV	0.01 eV
total uncertainty	0.16 eV	0.19 eV

Table 6.2.: List of uncertainties for width and position of the negative peak in the measured neutron spectrum. The first 4 uncertainties are systematic errors. The total uncertainty was calculated by summation of the total systematic error and the fit uncertainty.

The uncertainty of the width also splits in several components. The first one is the energy spread resulting from the thickness of the moderator in line of sight to the detector of 0.11 eV specified in section 6.2. The second one originates from the temporal resolution of the detector system given above. The third one is caused by the measurement uncertainty of the distance from the source to the detector, which also has an influence on the temporal spread of the pulse yielding 0.01 eV. These three effects lead to resolution broadening as it was described in section 3.6. The other reason for a broadening discussed in the same section is the Doppler effect. Using equation (3.10) with the indium mass m=115 u, the resonance position at 1.46 eV and room temperature T=293.15 K, this leads to a Doppler width of $\mathrm{FWHM} = 2\sqrt{2\ln(2)}\Gamma_\mathrm{D} = 0.08\,\mathrm{eV}$. A summary of the uncertainties is given in table 6.2.

The central energy and width of the negative peak in the measured neutron spectrum shown in Figure 6.8 are (1.61 ± 0.19) eV and (0.25 ± 0.16) eV, respectively. An evaluation of these values can be undertaken by their comparison with published theoretical and experimental values. A comparison with the experimental results obtained by McDaniel in 1946 [177], which are $E = (1.44 \pm 0.03)$ eV and $\Gamma = (0.085 \pm 0.001)$ eV, leads to a good agreement within the uncertainty limits. In addition to reference [177], the central energy and width of the resonance can also be obtained from the total neutron reaction cross section of ^{115}In displayed in Figure 3.7 [102] in chapter 3. A Lorentzian fit to the graph results in a central energy of (1.456 ± 0.001) eV with a width of (0.1011 ± 0.002) eV. The accordance of the parameters of the indium resonance with the experimental results obtained by McDaniel and within the framework of this thesis leads to the conclusion that a neutron resonance spectroscopy on a static indium sample with a laser-driven neutron source could successfully be shown.

To increase statistics and reduce the noise level of the data, which effects the measurement results, several shots with identical experimental conditions in open beam configuration as well as with indium in the beam path were averaged and are displayed in Figure 6.10. As expected, due to the additional material in the neutron beam path, the averaged indium measurements (blue) show lower neutron numbers than the open beam measurements (violet). It is also noticeable, that the amplitude of the high frequency oscillations is reduced compared to the data shown in Figures 6.8 and 6.7, namely approximately by a factor of 3 to 4. A Lorentzian fit to the resonance results in a central energy of (1.61 ± 0.19) eV and a FWHM of (0.27 ± 0.17) eV. These values are in agreement with the ones obtained from the single shot measurement and

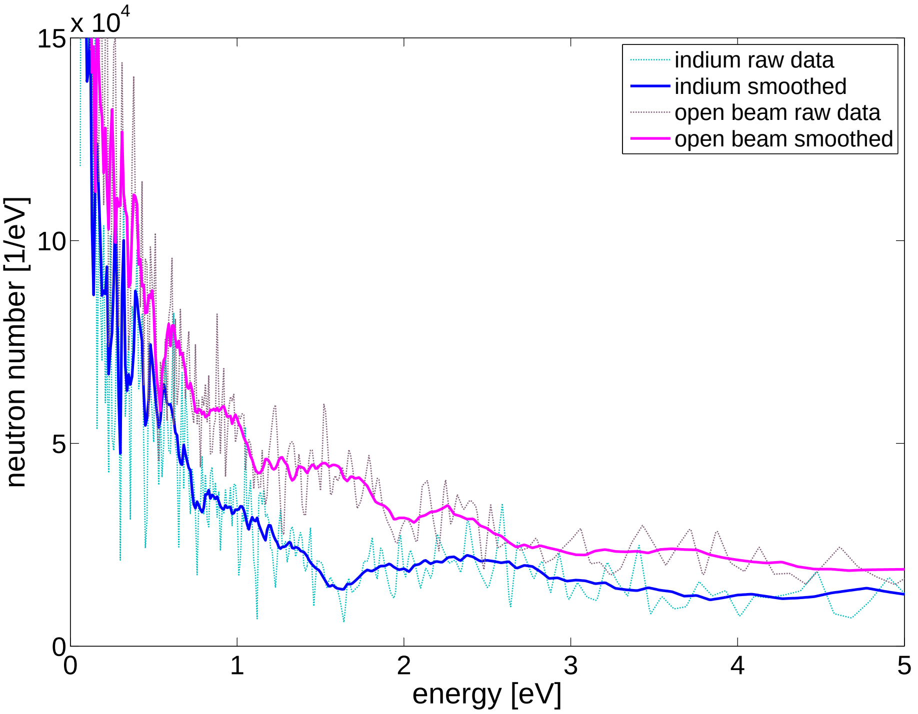

Figure 6.10.: Comparison of open beam measurements averaged over five shots (violet) and measurements with a 5 mm indium sample averaged over three shots (blue). The dotted and solid lines are the raw data and a smoothing by a moving average over 10 data points, respectively.

the other references. The slightly higher uncertainty of the width originates from the higher fit uncertainty of the shot-averaged data compared to the single shot data.

The results from the indium measurements are very promising in many aspects. As mentioned above, they demonstrate that a single shot of a laser-driven neutron source is potentially sufficient to perform neutron resonance spectroscopy on a static sample. By integration over several measurements, the quality is increased as the noise of the signal can be reduced significantly. The presence of the resonance in the integrated results of the indium measurements underlines that the single shot resonance is not a product of the data oscillations, but a reproducable characteristic of the neutron spectrum. These proof of principle results are the basis for future experiments with improved diagnostics as well as high repetition rate laser systems.

7 Summary and conclusions

The goal of this thesis was to optimize a laser-driven neutron source for the utilization of different high- as well as low-energy neutron applications. In addition to the verification of the reproducability and an increased neutron yield, the moderation of the neutron spectrum and the demonstration of the applicibility to neutron resonance spectroscopy were the two key aspects.

During the first experimental campaign at the PHELIX laser at GSI, the for applications indispensable reproducability of the emitted neutron yield and its maximization for the high-energy part of the spectrum were investigated and improved. For the realization of a continuous and high neutron yield, a stable and reproducable ion source is required as a basis. Constant maximum proton energies between 50 and 70 MeV with a mean energy of (62.6 ± 7.9) MeV could be shown with RCF measurements. In the next step, the utilization of a tungsten cylinder around the beryllium catcher contributed to an increased neutron yield in the forward direction by reflection of sidewards propagating neutrons back into the catcher. The bubble detector measurements demonstrated constant maximum neutron numbers of $(5.25 \pm 0.77) \cdot 10^{10}$ per shot with a maximum yield of $(1.42 \pm 0.25) \cdot 10^{10}$ n/sr in the forward direction, which is an increase of 40 % compared to the highest neutron yield found in literature [25]. In addition, with the use of up to 30 bubble detectors simultaneously, the most detailed measurement of the angular distribution published so far could be achieved. This allowed for the determination of an opening angle $\vartheta = (100 \pm 2)^\circ$ of the forward directed neutron beam.

The experiments on moderation and neutron resonance spectroscopy were conducted at the Trident laser facility at LANL. For the design of the moderator, which was optimized for the NRS measurements, amongst others, the following criteria had to be considered: first, moderated neutrons are scattered out to the sideward directions and second, the moderator dimension in line of sight to the detector has to be as small as possible because the moderator thickness is the main cause for a temporal spread of the neutron pulse. An optimized beryllium catcher with a cylindrical hole in the direction of the incoming ion beam was placed inside the HDPE moderator with a total length of 138 mm and a width of 70 mm in line of sight to the boron-doped MCP detector. A collimator was additionally placed between the source and the detector.

The moderated neutrons were measured with a set of low-energy neutron detectors including rhodium counters, an array of ^{3}He tubes, and two boron-doped MCP detectors. The two first diagnostics showed an increase of the low-energy neutron yield in the range of 10 to 40 % integrated over all energies when compared to a shot without moderator. An energetically resolved spectrum could be obtained with the MCP detectors. As the readout electronics of the ProxiVision detector was not adapted to a measurement in the energy range around the indium resonance, only the measurement with the Nova Scientific MCP yielded a factor 3 more neutrons at 1.5 eV. However, the results of both detectors are in agreement in the thermal energy range, showing one order of magnitude more neutrons at 25 meV.

For the NRS measurement, the broad ^{115}In resonance at 1.46 eV was chosen for its high neutron reaction cross section and its low central energy. The latter is important, because of the detection efficiency of the boron-doped MCP, which rapidly decreases with increasing neutron energy. The experiments resulted in a single shot measurement of the indium resonance with a central energy of (1.61 ± 0.19) eV and a width of (0.25 ± 0.16) eV. These values were obtained with a Lorentzian fit to the resonance and are in good agreement with the calculated values from reference [102] and the experimental results of reference [177]. However, although the resonance width of the single shot measurement was determined, the accuracy of this result considered by itself is not dependable because the high noise level in the data effects the resonance shape. The low signal to noise ratio of the single shot measurement could be improved by averaging several shots. The resonance parameters of this analysis are consistent with those of the single shot measurement.

During the framework of this thesis, it could be shown that a laser-based neutron source can be operated with a steady angular distribution and a constantly high neutron yield, which allows reproducible and significant measurements in applications. The succesful moderation of the laser-driven neutrons and the verification of their feasibility for neutron resonance spectroscopy are powerful proof of principle results that demonstrate the potential of a laser-based neutron source. They are a representative example of the characteristics necessary for a possible extension of laser-driven neutrons to a wide field of applications. With further research and development in the following years, these sources will be able to complement conventional reactors or accelerator-based spallation sources regarding certain applications.

8 Future prospects

The following chapter introduces several approaches for further development of laser-based neutron sources regarding different applications. The first section will discuss optimization possibilities for high-energy neutron applications. Improvements on the experimental setup on laser-based neutron resonance spectroscopy and possible next steps for future experiments will be given in the second section. As detector development is essential for reliable measurements in future applications, a few concepts for detector improvement will be presented at the end of this chapter.

8.1 High-energy neutron applications

A reproducable and stable laser-driven neutron source is the fundament for applications. However, further research and optimization as well as characterization is required to improve the usability of a laser-driven neutron source. The different aspects will be introduced on a specific example of laser-based fast neutron radiography (FNR).

During one of the experimental campaigns at Trident, a neutron imager for fast neutron radiography was placed in the laser forward direction. The detector consisted of 1 cm polyethylene and a copper-doped ZnS converter. Different materials with varying thicknesses were placed in front of the detector, as can be seen in Figure 8.1a. An image from a single shot fast neutron radiography is shown in Figure 8.1b.

The visibility of different thicknesses of polyethylene strongly indicates, that the main contribution to the image originates from neutrons. Nevertheless, a laser-driven neutron source also emits gamma radiation, that overlays the neutron signal. Thus, a detailed study on the gamma spectrum of such a source is of great importance not only for FNR, but also for other applications and detection systems that do not provide an internal discrimination of gamma rays and neutrons. This investigation should be attempted with a dedicated gamma detector which is insensitive to neutrons. Possible approaches are an internal discrimination of gamma rays and neutrons, for instance by pulse-shape, and activation measurements with appropriate materials.

Compared to the highest fluxes from accelerator-based spallation sources, the maximum neutron yield from a laser-driven neutron source is a few orders of magnitude less, which in the example given here is reflected in the resolution of the image. A further increase of the maximum neutron numbers or a less divergent neutron beam would improve the single shot resolution of the measurement. Another option to achieve an increase of the resolution is the integration over several shots. However, at laser systems like PHELIX or Trident this requires many days of beamtime, since their repetition rate is 90 minutes. In this regard, experiments at high repetition rate systems like the BELLA laser at Lawrence Berkeley National Laboratory (LBNL), which

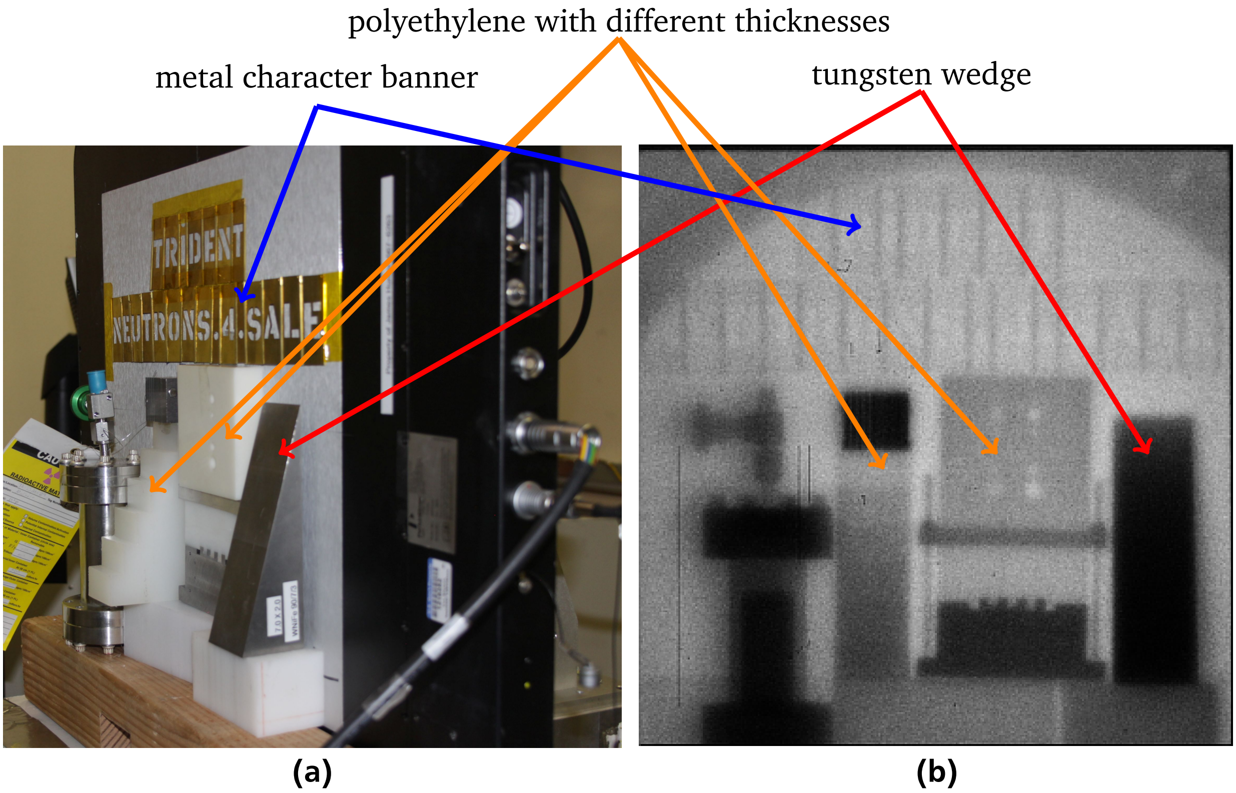

Figure 8.1.: (a) Photograph of the materials placed in front of the detector. (b) Result from a single shot FNR measurement. LA-UR-16-28283, Courtesy of Ronald Nelson.

operates at 1 Hz, hold a great advantage and should be preferred for future application-oriented laser-based neutron experiments.

8.2 Improvement of the NRS setup and its application for temperature measurements and neutron imaging

The introduced experiment on NRS at the Trident laser facility represents a first successful proof of principle measurement with a laser-based neutron source. Nevertheless, the experimental conditions should be improved and optimized to gain a better signal to noise ratio as well as a more pronounced resonance.

A first point is the optimization of the catcher-moderator configuration to further increase the neutron number with epithermal energies. This could be achieved by a reflector material such as tungsten or beryllium, that scatters fast neutrons back into the moderator, as it is used in reactors or at accelerator-based spallation sources (cf. section 3.6). An expansion of the moderator material in the direction of the incoming ion beam would increase the number of moderated neutrons which are emitted in the backward direction. A sketch of the proposed geometry is shown in Figure 8.2. Additionally, a reduction of the moderator dimension in line of sight to the detector could increase the resolution of the measurement and permit a more accurate determination of the resonance width.

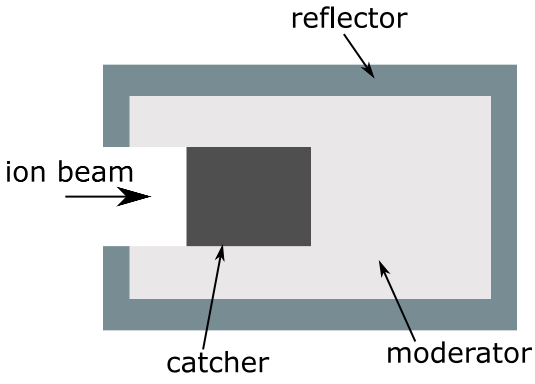

Figure 8.2.: Scheme of an optimized moderator geometry.

Further improvement is also possible on the NRS sample itself and the lead sheet in front of the detector. The thickness of both materials can have a great effect on the resonance measurement. During the experiment, a lead sheet with 3 mm thickness was used. This layer not only shields the detector from the gamma radiation produced during the interaction of the sample material with neutrons, but also reduces the neutron flux. If the lead sheet is too thin, the shielding from gamma rays will not be sufficient. However, if it is too thick, its effect on the penetrating neutrons could be significant. The optimum between these two cases should be calculated by undertaking a parameter study with codes such as FLUKA [182, 183] or GEANT [184] and is very important for an improved measurement.

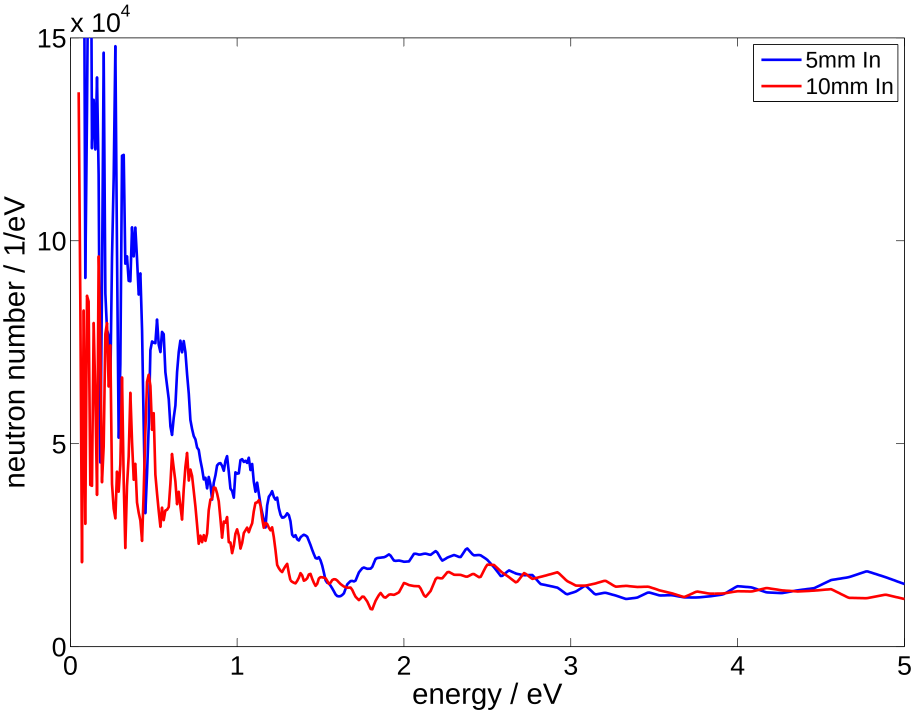

Figure 8.3.: Comparison of two single shot measurments of the indium resonance with a 5 mm (blue) and a 10 mm (red) sample.

The influence of the indium thickness on the neutron spectrum is shown in Figure 8.3. It compares two smoothed single shot resonance measurements with a 5 mm (blue) and a 10 mm (red) thick indium sample. It is clearly visible, that the resonance of the 10 mm sheet is much broader and flatter than that of the 5 mm sheet. This is caused by scattering inside the indium sample, which results in a broadening of the neutron pulse. In addition, it is apparent that the total neutron yield is reduced the more the thicker the sample. Thus, on the one hand a thin sample would be preferable, but on the other hand it has to be thick enough for neutron reactions to take place to a degree for a significant signal in the measurement. The optimum sample thickness should again be simulated with appropriate codes.

In addition, NRS experiments with a laser-driven neutron source can greatly be improved by their conduction at a high repetition rate laser system. This enables integration over many shots in a short time, which is essential for the necessary reduction of the signal to noise ratio.

When the optimization of a laser-driven NRS source has been completed, it can be tested for applications, for instance temperature measurements on shocked or heated samples. This is obtained by measurement of the Doppler broadening of the materials resonances. The more pronounced the broadening of the measured resonance, the easier it is to extract a reliable width from the data. To achieve that, strong heating of the material is required. Therefore, for a first verification of the feasibility, it would be benefitial to choose a sample that remains its solid state when significantly heated. Materials with high melting points at normal pressure are for instance carbon (graphite: 3948 K, diamond: 3820 K), tungsten (3695 K), tantalum (3290 K), molybdenum (2896 K), boron (2349 K), and platinum (2047 K). However, to perform NRS measurements the chosen sample needs to have a broad resonance with a high reaction cross section in the epithermal range. These requirements are fulfilled by tungsten, molybdenum, and tantalum. Their total cross sections are displayed in Figure 8.4(a). ^{195}Pt has a resonance at 12 eV with a cross section of 1000 b, which is one order of magnitude below that of tungsten and tantalum. Carbon could be used for fast neutron resonance spectroscopy as it has several resonances in the range of a few MeV, but with cross sections of only a few barn.

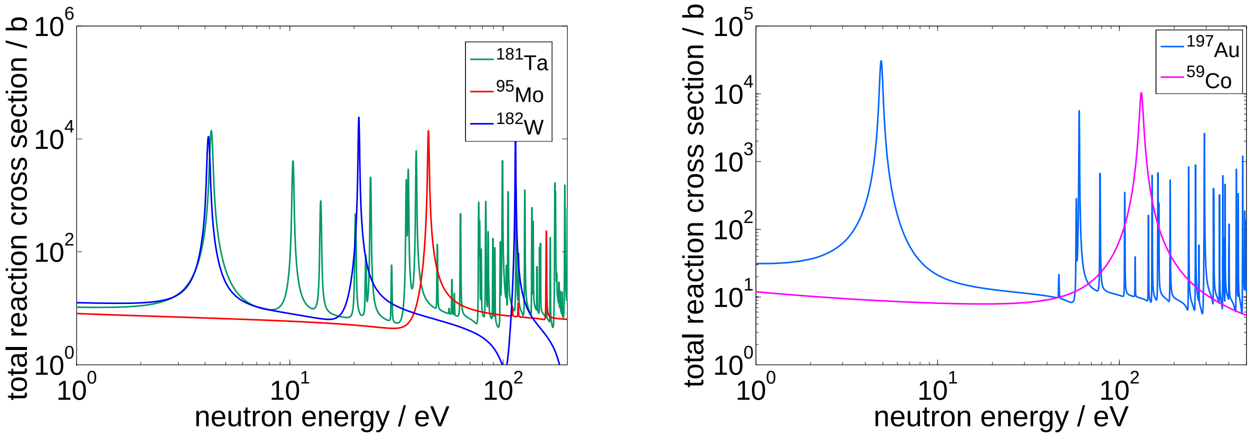

(a)

(b)

Figure 8.4.: Total reaction cross sections of neutrons with different materials proposed for (a) temperature measurements and (b) imaging experiments with a laser-driven neutron source.

Another application for NRS is neutron imaging. This method uses a transmission spectrum of the sample to identify energy intervals with resonances and the contained materials. Based on this information, several imaging measurements in the determined energy regions are conducted. This enables the visualization of structures of different materials in a bulk sample.

In practice, the advantage of imaging compared to temperature measurements is the lower required neutron flux. Schillebeecks *et al.* [26] performed a NRS image with an epithermal neutron flux between 10 and $10^4\,\mathrm{eV}^{-1}\mathrm{cm}^{-2}\mathrm{s}^{-1}$ on target and achieved a very good resolution. During the experiment at Trident presented in the framework of this thesis, the measured epithermal neutron yield was of the order of 10^4 to $10^5\,\mathrm{eV}^{-1}$ per pulse (cf. e.g. Figure 6.8). This corresponds to 10^3 to $10^4\,\mathrm{eV}^{-1}\mathrm{cm}^{-2}$ per pulse on the sample for the given setup, which is sufficient for a NRS imaging measurement. For the realization of a laser-driven neutron experiment, the resonances of the chosen materials should be at least several 10 eV apart from each other to avoid an overlap in the transmission spectrum that could be caused by broadening due to the moderator thickness or the low signal to noise ratio. In addition, this simplifies the determination of the energy interval for the specific measurements. A suitable material combination would for instance be gold and cobalt whose cross sections are displayed in Figure 8.4(b).

8.3 Detector improvements

As mentioned in chapter 4, the environment of a laser-driven neutron source represents a great challenge for the detection methods. Electromagnetic pulses can couple into electronic systems and generate noise which overlays with the signal preventing its identification in the worst case. In addition, the high gamma flux can saturate the detection systems and cause an overlap of the gamma signal with the neutron signal in a way that both are not distinguishable anymore (cf. Figure 4.5).

In the framework of a supervised bachelor's thesis, Simone Aumüller investigated possible improvements on the time of flight detectors for high-energy neutrons [161]. Her work focused on the analysis of the time response of different scintillators (NE-102, NE-110) and photomultiplier tubes. Because measurements with the Hamamatsu PMT R1250 partly used for the experiments at Trident resulted in an overlap of the gamma and neutron signals, the Photonis XP4362B with only six dynodes and a new Photek PMT240/Q/BI were used for this purpose. To further increase the separability of gamma rays and neutrons in the future, two promising alternative scintillators could be used in combination with the mentioned existing PMTs: PilotU and NE-111A. The important overlap of the emission spectrum of the scintillators and the spectral sensitivity of the PMTs shows that NE-111A can best be combined with the Photek PMT240/Q/BI, but does not match the spectral sensitivity of XP4362B. In contrast, PilotU can be coupled to both available PMTs and additionally has shorter rise and decay times resulting in a smaller overlap of the gamma signal with the neutron signal. A comparison of the theoretical response functions of the previously used scintillator NE-102 with the proposed PilotU coupled to a Photonis XP4362B PMT is shown in Figure 8.5. The overlap with the neutron signal (displayed for different energies) is clearly smaller for the new scintillator PilotU.

To improve the quality of the NRS measurement and expand the set of possible materials, an increase of the detector efficiency in the epithermal energy range would be of great benefit. One the one hand, the number of detected neutrons and thus the signal to noise ratio would

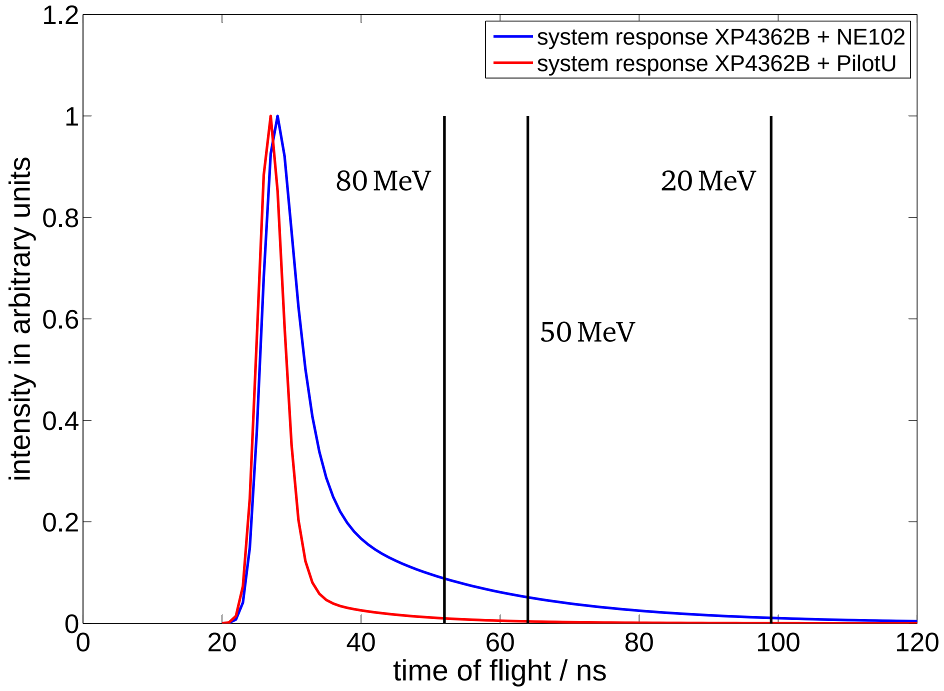

Figure 8.5.: Temporal system response calculated by convolution of the time response of the scintillators NE102 (blue) and PilotU (red) with a Photonis XP4362B PMT. The temporal characteristics of the components were obtained from references [159, 161, 185–187]. The black lines mark arrival times for neutrons with different energies. The calculation is based on the experimental setup of the Trident experiment introduced in section 6.1 for a detector at a distance of 6 m from the neutron source. $t = 0$ s is defined as the time of the laser shot.

be increased. On the other hand, a higher detection efficiency at energies up to a few 10 eV or a few 100 eV would include possible studies on materials like gold ($E = 4.9$ eV, $\sigma = 30$ kb), tantalum ($E = 4.5$ eV, $\sigma = 10$ kb), tungsten ($E_1 = 4.15$ eV, $\sigma_1 = 11$ kb, $E_2 = 21$ eV, $\sigma_2 = 25$ kb), and cobalt ($E_1 = 132$ eV, $\sigma_1 = 10$ kb, $E_2 = 5$ keV, $\sigma_2 = 300$ b). Especially tungsten and tantalum are interesting materials for temperature measurements due to their high melting points. A higher detection efficiency in the energy regime of several 100 eV could be obtained by coupling a lithium glass scintillator (e.g. GS20 from Saint Gobain [188]) to a PMT.

Acknowledgements

Zuerst möchte ich mich bei **Prof. Dr. Markus Roth** für die freundliche Aufnahme in eine tolle Arbeitsgruppe bedanken. Er hat mir die Möglichkeit gegeben im Rahmen meiner Masterarbeit an einem aktuellen und sehr interessanten Thema zu arbeiten und dieses im Rahmen meiner Promotion zu vertiefen und voranzutreiben. Während der Zeit in dieser Arbeitsgruppe konnte ich einige Strahlzeiten im Ausland durchführen. Markus hat viel dazu beigetragen, dass ich nicht nur mit Erinnerungen an die Experimente nach Deutschland zurück gekommen bin. Vielen Dank dafür!

Mein besonderer Dank gilt außerdem **Oliver Deppert**, der mich seit Beginn meiner Masterarbeit begleitet und "groß gezogen" hat. Im Laufe unserer gemeinsamen Zeit in dieser Arbeitsgruppe hat er mich immer wieder unterstützt, mir vieles beigebracht und mich auf den Boden der Tatsachen zurückgeholt, wenn es nötig war.

Ich möchte mich an dieser Stelle auch bei meinen ersten Bürokollegen **Jan Helfrich** und **Simon Frydrych** für zwei wundervolle Jahre voller konstruktiver Arbeit, Scherze und Weltherrschaftsentwürfe bedanken. Auch mit **Diana Jahn** und **Victor Schanz** hatte ich ein Jahr lang sehr viel Spaß und dank ihnen viele Anregungen für meine Datenauswertung und Thesis.

Außerdem gilt mein Dank dem gesamten PHELIX Team **Vincent Bagnoud**, **Stefan Götte**, **Bernhard Zielbauer**, **Udo Eisenbarth**, **Dirk Reemts**, **Christian Brabetz** und **Sabine Kunzer**, die mir die erfolgreiche Durchführung und einen reibungslosen Ablauf des PHELIX Experimentes ermöglicht haben.

Furthermore, I would like to thank the Trident team **Randy Johnson**, **Cort Gautier**, **Ray Leeper**, **Tom Shimada**, **Sha-Marie Reid**, and **Russell Mortensen** as well as **Glen Wurden** and **Andrea Favalli** from LANL for the technical, physical, and mental support during my Trident beamtimes.

Zu einer erfolgreichen Strahlzeit gehört nicht nur das Experiment selbst, sondern auch die Vorbereitung. Dabei ist auch die Herstellung und Charakterisierung der Targets von Bedeutung. In diesem Zusammenhang möchte ich mich bei allen Mitgliedern des Targetlabors am Institut für Kernphysik der TU Darmstadt bedanken. Insbesondere bei **Gabriel Schaumann**, der mich während meiner Promotion immer unterstützt hat, aber auch bei **Johannes Hornung**, der für viele meiner Strahlzeiten fleißig Targets gebastelt und charakterisiert hat.

Die **gesamte Arbeitsgruppe der Laser- und Plasmaphysik** hat dazu beigetragen, dass ich vier tolle Jahre hatte. Ich konnte bei meinen Experimenten und physikalischen Problemen immer auf die Unterstützung der Mitglieder zählen. Insbesondere die Besatzung im Kinderzimmer an der GSI hat auch mit wechselnden Mitgliedern wesentlich zu meiner physikalischen, kulturellen und sozialen Weiterbildung beigetragen.

Nicht zuletzt möchte ich mich bei all denen bedanken, die sich die Mühe gemacht haben meine Arbeit zu lesen und wertvolle Tipps und Anregungen beizutragen. Dies sind im Besonderen

Diana Jahn, **Philippe Poth**, **Dr. Dennis Schumacher**, **Alexandra Tebartz**, **Dr. Sven Vogel**, **Dr. Florian Wagner**, **Marc Zimmer** und **Yannik Zobus**.

Mein ganz besonderer Dank gilt aber meinen Eltern **Dr. Rüdiger** und **Gabriele Kleinschmidt**, die mein ganzes Leben für mich da waren und mich unterstützt haben. Zu ihnen konnte ich immer mit meinen kleinen und großen Problemen kommen und fand Rat und geduldige Zuhörer, auch wenn ich bestimmt nicht immer einfach gewesen bin. Ihnen verdanke ich die Möglichkeit, dass ich studieren und meine Promotion machen konnte. Vielen Dank für all die kleinen und großen Dinge, die ihr für mich getan habt und auch für die, die ihr noch tun werdet!

A Appendix

A.1 Effects of the pulse shape at high-intensity short-pulse laser systems on the target

The CPA technique introduced by Strickland and Mourou [30] in 1985 marked a breakthrough in modern laser physics. This method is based on stretching a short pulse prior to amplification and afterwards compressing it to its final pulse length as shown in Figure A.1.

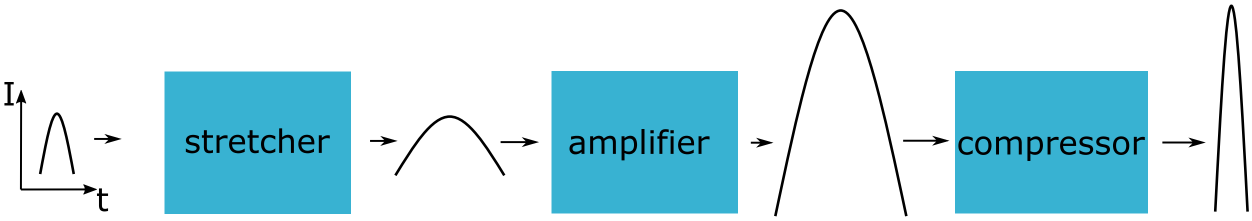

Figure A.1.: Simplified sketch of the CPA method.

However, in a real laser system undesirable effects such as amplified spontaneous emission (ASE) [189], modulations of the pulse spectrum in one of the optical components of the CPA chain (stretcher, amplifier, compressor), and reflections at optical components can occur. ASE is one effect that leads to a pedestal, which is arriving at the target front side a few hundred picoseconds prior to the main pulse. Modulations of the pulse spectrum for instance influence the rising edge of the laser pulse in a way that it becomes broader, which leads to a longer rise time. Reflections in the system or postpulses can result in prepulses [190], which occur as spikes on the ASE level.

Spectral modulations and other influencing factors on the rising edge of the pulse as well as prepulses can partly be overcome by optimizing the laser system, although these effects are very complex and not fully understood to this day. In contrast to that, ASE is one of the effects that always occur and can not be avoided. Nevertheless, its influence on the target can be lessened by improving the contrast of the system, which can roughly be described as the intensity level of the main pulse relative to a certian time prior to the maximum of the main pulse. Still it should be mentioned that the point in time, to which the contrast of a laser is measured, is not specified.

Figure A.2(a) shows the pulse shape of the PHELIX system [191] with a flat rising edge starting to increase from the ASE level at about 150 ps prior to the maximum of the main pulse. In comparison, the Trident pulse displayed in Figure A.2(b) has a much steeper rising edge. The intensity starts to increase from the ASE level at about -40 ps. However, the contrast of the Trident laser is at least one order of magnitude less compared to the one at PHELIX. But it has to be mentioned, that the ASE level of Trident can not be determined from the graph in

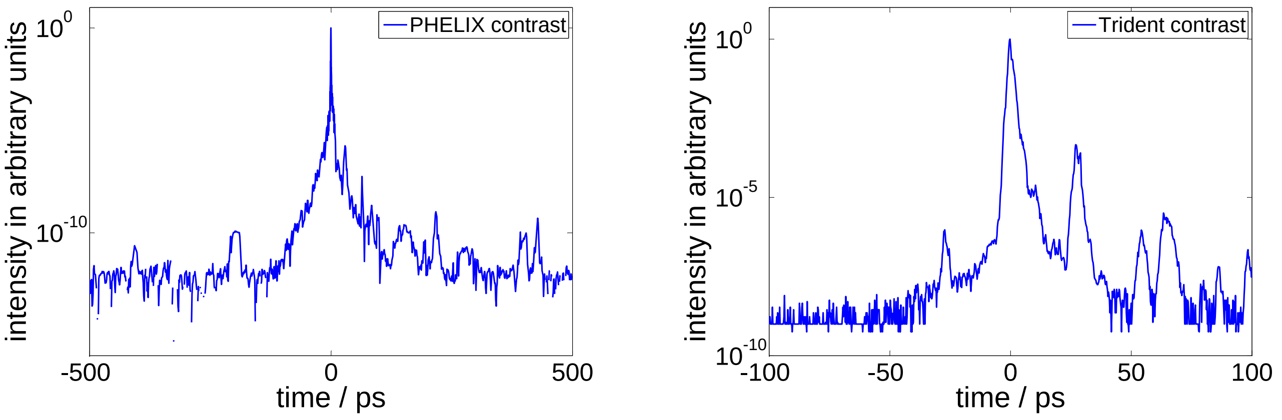

(a) **(b)**

Figure A.2.: Contrast of (a) the PHELIX system ([191], courtesy of Victor Schanz) compared to (b) the one of the Trident laser (LA-UR-10-02758, courtesy of Randall Johnson).

Figure A.2(b), as the constant behavior at 10^{-9} most likely originates from the detection limit of the measurement.

Todays laser systems provide peak intensities above 10^{21} W/cm^2 [59]. As mentioned in chapter 2, ionization of a solid target irradiated by a high-intensity short-pulse laser starts to set in at intensities of the order of 10^9 W/cm^2 [31]. Consequently, the ASE level is near or above the ionization threshold, which means, that the prepulse of the laser can ionize the target frontside several 100 ps before the main pulse arrives. Depending on the slope of the rising edge, this can cause a significant pre-expansion of the target.

For more detailed information on CPA, pulse-shaping in laser systems, and studies of the interaction of the prepulse with the target surface, the reader is referred to the literature [30, 166, 189, 190, 192–194].

Bibliography

[1] N. A. Tahir, D. H. H. Hoffmann, J. A. Maruhn, K.-J. Lutz, and R. Bock. Creation of metallic hydrogen in imploding cylindrical targets with intense heavy ion beams to be produced at the GSI Darmstadt SIS Facility. *Phys. Lett. A*, 249:489–494, 1998.

[2] N. Takenaka, H. Asano, T. Fujii, M. Mizubata, and K. Yoshii. Application of fast neutron radiography to three-dimensional visualization of steady two-phase flow in a rod bundle. *Nucl. Instr. Meth. Phys. Res. A*, 424(73), 1999.

[3] A. Wiedenmann, U. Keiderling, K. Habicht, M. Russina, and R. Gähler. Dynamics of field-induced ordering in magnetic colloids studied by new time-resolved small-angle neutron-scattering techniques. *Phys. Rev. Lett.*, 97(057202), 2006.

[4] F. Fiori, A. Hilger, N. Kardjilov, and G. Albertini. Crack detection in Al alloy using phase-contrast neutron radiography and tomography. *Meas. Sci. Technol.*, 17(9):2479–2487, 2008.

[5] Oliver J. Weiß, Ermile Gagandize, and Jarir Aktaa. Quantitative characterizaton of microstructural defects in up to 32 dpa neutron irradiated EUROFER97. *J. Nucl. Mater.*, 426:52–58, 2012.

[6] G. Zaccai. How soft is a protein? a protein dynamics force constant measured by neutron scattering. *Science*, 288(1604), 2000.

[7] R. L. Morgan. Fast neutron therapy. *AIP Conf. Proc.*, (562), 1972.

[8] L. H. Gray and J. Read. Treatment of cancer by fast neutrons. *Nature*, 152(53), 1943.

[9] W. Kockelmann, A. Kirfel, S. Siano, and C. D. Frost. Illuminating the past: the neutron as a tool in archaeology. *Phys. Educ.*, 39(2), 2004.

[10] Nikolay Kardjilov, Fabrizio Fiori, Giuseppe Giunta, André Hilger, Franco Rustichelli, Markus Strobl, Roberto Triolo, and John Banhart. Neutron tomography for archaeological investigations. *J. Neutron Res.*, 14:29–36, 2006.

[11] A. M. Weinberg and E. P. Wigner. *The physical theory of neutron chain reactors*. The University of Chicago Press, third edition, 1972.

[12] B. C. Reed. *The Physics of the Manhatten Project*. Springer Verlag Berlin-Heidelberg, 2011.

[13] S. C. Vogel and H.-G. Priesmeyer. Neutron Production, Neutron Facilities and Neutron Instrumentation. *Rev. Mineral. Geochem.*, 63:27–57, 2006.

[14] G. J. Russell. Spallation sources - an overview. In *ICANS-XI International Collaboration on Advanced Neutron Sources*, 1990.

[15] M. N. H. Comsan. Spallation neutron sources for science and technology. Proceedings of the 8^{th} Conference on Nuclear and Particle Physics, 2011.

[16] B. M. Hegelich, B. Albright, P. Audebert, A. Blazevic, E. Brambrink, J. Cobble, T. Cowan, J. Fuchs, J. C. Gauthier, C. Gautier, M. Geissel, D. Habs, R. Johnson, S. Karsch, A. Kemp, S. Letzring, M. Roth, J. Schreiber U. Schramm, K. J. Witte, and J. C. Fernández. Spectral properties of laser-accelerated mid-Z MeV/u ion beams. *Phys. Plasmas*, 12(056314), 2005.

[17] E. L. Clark, K. Krushelnick, M. Zepf, F. N. Beg, M. Tatarakis, A. Machacek, M. I. K. Santala, I. Watts, P. A. Norreys, and A. E. Dangor. Energetic heavy-ion and proton generation from ultraintense laser-plasma interactions with solids. *Phys. Rev. Lett*, 85(8), 2000.

[18] P. McKenna, K. W. D. Ledingham, T. McCanny, R. P. Singhal, I. Spencer, M. I. K. Santala, F. N. Beg, K. Krushelnick, M. Tatarakis, M. S. Wei, E. L. Clark, R. J. Clarke, K. L. Lancaster, P. A. Norreys, K. Spohr, R. Chapman, and M. Zepf. Demonstration of fusion-evaporation and direct-interaction nuclear reactions using high-intensity laser-plasma-accelerated ion beams. *Phys. Rev. Lett*, 91(7), 2003.

[19] R. A. Snavely, M. H. Key, S. P. Hatchett, T. E. Cowan, M. Roth, T. W. Phillips, M. A. Stoyer, E. A. Henry, T. C. Sangster, M. S. Singh, S. C. Wilks, A. MacKinnon, A. Offenberger, D. M. Pennington, K. Yasuike, A. B. Langdon, B. F. Lasinski, J. Johnson, M. D. Perry, and E. M. Campbell. Intense high-energy proton beams from petawatt-laser irradiation of solids. *Phys. Rev. Lett.*, 85(14), 2000.

[20] F. Wagner, O. Deppert, C. Brabetz, P. Fiala, A. Kleinschmidt, P. Poth, V. A. Schanz, A. Tebartz, B. Zielbauer, M. Roth, T. Stöhlker, and V. Bagnoud. Maximum proton energy above 85 MeV from relativistic interaction of laser pulses with micrometer thick CH_2 targets. *Phys. Rev. Lett.*, 116(205002), 2016.

[21] D. Jung, L. Yin, B. J. Albright, D. C. Gautier, S. Letzring, B. Dromey, M. Yeung, R. Hörlein, R. Shah, S. Palaniyappan, K. Allinger, J. Schreiber, K. J. Bowers, H-C. Wu, J. C. Fernández, D. Habs, and B. M. Hegelich. Efficient carbon ion beam generation from laser-driven volume acceleration. *New J. Phys.*, 15(023007), 2013.

[22] B. M. Hegelich, D. Jung, B. J. Albright, J. C. Fernández, D. C. Gautier, C. Huang, T. J. Kwan, S. Letzring, S. Palaniyappan, R. C. Shah, H.-C. Wu, L. Yin, A. Henig, R. Hörlein, D. Kiefer, J. Schreiber, X. Q. Yan, T. Tajima, D. Habs, B. Dromey, and J. J. Honrubia. Experimental demonstration of particle energy, conversion efficiency and spectral shape required for ion-based fast ignition. *Nucl. Fusion*, 51(083011), 2011.

[23] S. C. Wilks, A. B. Langdon, T. E. Cowan, M. Roth, M. Singh, S. Hatchett, M. H. Key, D. Pennington, A. MacKinnon, and R. A. Snavely. Energetic proton generation in ultra-intense laser-solid interactions. *Phys. Plasmas*, 8(542), 2001.

[24] L. Yin, B. J. Albright, B. M. Hegelich, and J. C. Fernández. GeV laser ion acceleration from ultrathin targets: The laser break-out afterburner. *Laser and Particle Beams*, 24:291–298, 2006.

[25] M. Roth, D. Jung, K. Falk, N. Guler, O. Deppert, M. Devlin, A. Favalli, J. Fernández, D. Gautier, M. Geissel, R. Haight, C. E. Hamilton, B. M. Hegelich, R. P. Johnson, F. Merrill, G. Schaumann, K. Schoenberg, M. Schollmeier, T. Shimada, T. Taddeucci, J. L. Tybo, F. Wagner, S. A. Wender, C. H. Wilde, and G. A. Wurden. Bright laser-driven neutron

source based on the relativistic transparency of solids. *Phys. Rev. Lett.*, 110(044802), 2013.

[26] P. Schillebeeckx, A. Borella, F. Emiliani, G. Gorini, W. Kockelmann, S. Kopecky, C. Lampoudis, M. Moxon, E. Perelli Cippo, H. Postma, N. J. Rhodes, E. M. Schooneveldd, and C. Van Bevereng. Neutron resonance spectroscopy for the characterization of materials and objects. *J. Instrum.*, 7(C03009), 2012.

[27] S. Kar, A. Green, H. Ahmed, A. Alejo, A. P. L. Robinson, M. Cerchez, R. Clarke, D. Doria, S. Dorkings, J. Fernández, S. R. Mirfayzi, P. McKenna, K. Naughton, D. Neely, P. Norreys, C. Peth, H. Powell, J. A. Ruiz, J. Swain, O. Willi, and M. Borghesi. Beamed neutron emission driven by laser accelerated light ions. *New J. Phys.*, 18(053002), 2016.

[28] P. Rinard. Neutron Interactions with Matter. In Doug Reilly, Norbert Ensslin, Jr. Hastings Smith, and Sarah Kreiner, editors, *Passive Nondestructive Assay of Nuclear Materials*. 1991.

[29] V. Bagnoud, B. Aurand, A. Blazevic, S. Borneis, C. Bruske, B. Ecker, U. Eisenbarth, J. Fils, A. Frank, E. Gaul, S. Goette, C. Haefner, T. Hahn, K. Harres, H.-M. Heuck, D. Hochhaus, D. H. H. Hoffmann, D. Javorková, H.-J. Kluge, T. Kuehl, S. Kunzer, M. Kreutz, T. Merz-Mantwill, P. Neumayer, E. Onkels, D. Reemts, O. Rosmej, M. Roth, T. Stoehlker, A. Tauschwitz, B. Zielbauer, D. Zimmer, and K. Witte. Commissioning and early experiments of the PHELIX facility. *Appl. Phys. B*, 100:137–150, 2010.

[30] D. Strickland and G. Mourou. Compression of amplified chirped optical pulses. *Optics Communications*, 55:447–449, 1985.

[31] R. W. Boyd. *Nonlinear Optics*. Academic Press, third edition, 2008.

[32] P. Gibbon. *Short Pulse Laser Interactions with Matter: An Introduction*. Imperial College Press, 2005.

[33] P. Mulser and D. Bauer. *High Power Laser-Matter Interaction*. Springer-Verlag, 2010.

[34] D. Bauer, P. Mulser, and W.-H. Steeb. Relativistic Ponderomotive Force, Uphill Acceleration, and Transition to Chaos. *Phys. Rev. Lett.*, 75(25), 1995.

[35] A. Piel. *Plasma Physics: An Introduction to Laboratory, Space, and Fusion Plasmas*. Springer Verlag, 2010.

[36] F. F. Chen. *Introduction to plasma physics and controlled fusion: Volume 1: Plasma Physics*. 2. Aufl. Plenum Press, New York and London, 1984.

[37] S. Eliezer. *The Interaction of High-Power Lasers with Plasmas*. Institute of Physics Publishing Bristol and Philadelphia, 2002.

[38] P. Mulser, S. M. Weng, and Tatyana Liseykina. Analysis of the brunel model and resulting hot electron spectra. *Phys. Plasmas*, 19(043301), 2012.

[39] J. R. Davies. Laser absorption by overdense plasmas in the relativistic regime. *Plasma Phys. Control. Fusion*, 51(014006), 2009.

[40] L. M. Chen, J. Zhang, Q. L. Dong, H. Teng, T. J. Liang, L. Z. Zhao, and Z. Y. Wei. Hot electron generation via vacuum heating process in femtosecond laser–solid interactions. *Phys. Plasmas*, 8(2925), 2001.

[41] T.-Y. B. Yang, E. L. Kruer, R. M. More, and A. B. Langdon. Absorption of laser light in overdense plasmas by sheath inverse bremsstrahlung. *Phys. Plasmas*, 2(3146), 1995.

[42] W. L. Kruer and Kent Estabrook. J×B heating by very intense laser light. *Phys. Fluids*, 28(430), 1985.

[43] W. Rozmus and V.T. Tikhonchuk. Skin effect and interaction of short laser pulses with dense plasmas. *Phys. Rev. A*, 42(7401), 1990.

[44] P. Gibbon and A. R. Bell. Collisionless Absorption in Sharp-Edged Plasmas. *Phys. Rev. Lett.*, 68(1535), 1992.

[45] D. Umstadter. Relativistic laser-plasma interactions. *J. Phys. D*, 36(R151), 2003.

[46] D. F. Zaretsky *et al.* Landau damping in thin films irradiated by a strong laser field. *J. Phys. B*, 37(4817), 2004.

[47] V. S. Rastunkov and V. P. Krainov. Electron Stochastic Heating in the Interaction of a Short Pulse with *Laser Phys.*, 15(262), 2005.

[48] Y. Sentoku, V. Y. Bychenkov, K. Flippo, A. Maksimchuk, K. Mima, G. Mourou, Z. M. Sheng, and D. Umstadter. High-energy ion generation in interaction of short laser pulse with high-density plasma. *Appl. Phys. B*, 74(207), 2002.

[49] A. Macchi, F. Cornolti, F. Pegoraro, T. V. Liseikina, H. Ruhl, and V. A. Vshivkov. Surface Oscillations in Overdense Plasmas Irradiated by Ultrashort Laser Pulses. *Phys. Rev. Lett.*, 87(20), 2001.

[50] A. Macchi, F. Coronolti, and F. Peforaro. Two-surface wave decay. *Phys. Plasmas*, 9(5), 2002.

[51] S. Kahaly, S. K. Yadav, W. M. Wang, S. Sengupta, Z. M. Sheng, A. Das, P. K. Kaw, and G. R. Kumar. Near-Complete Absorption of Intense, Ultrashort Laser Light by Sub-λ Gratings. *Phys. Rev. Lett*, 101(145001), 2008.

[52] K .G. Estabrook, E. J. Valeo, and W. L. Kruer. Two-dimensional relativistic simulations of resonance absorption. *Phys. Fluids*, 18(1151), 1975.

[53] T. Liseykina, P. Mulser, and M. Murakami. Collisionless absorption, hot electron generation, and energy scaling in intense laser-target interaction. *Phys. Plasmas*, 22(033302), 2015.

[54] F. Brunel. Not-so-resonant, resonant absorption. *Phys. Rev. Lett*, 59(1), 1987.

[55] S. Wilks, W. L. Kruer, M. Tabak, and A. B. Langdon. Absorption of ultra-intense laser pulses. *Phys. Rev. Lett.*, 69(9):1383–1386, 1992.

[56] G. Malka and J. L. Miquel. Experimental Confirmation of Ponderomotive-Force Electrons Produced by an ultrarelativistic Laser Pulse on a Solid Target. *Phys. Rev. Lett*, 77(75), 1996.

[57] Hong bo Cai, Wei Yu, Shao ping Zhu, and Chun yang Zheng. Short-pulse laser absorption via J×B heating in ultrahigh intensity laser plasma interaction. *Phys. Plasmas*, 13(113105), 2006.

[58] A. Macchi, Marco Borghesi, and Matteo Passoni. Ion acceleration by superintense laser-plasma interaction. *Rev. Mod. Phys.*, 85(751), 2013.

[59] S.-W. Bahk, P. Rousseau, T. A. Planchon, V. Chvykov, G. Kalintchenko, A. Maksimchuk, G. A. Mourou, and V. Yanovsky. Characterization of focal field formed by a large numerical aperture paraboloidal mirror and generation of ultra-high intensity (10^{22} W/cm^2). *Appl. Phys. B*, 80:823–832, 2005.

[60] P. E. Young, G. Guethlein, S. C. Wilks, J. H. Hammer, W. L. Kruer, and K. G. Estabrook. Fast ion production by laser filamentation in laser-produced plasmas. *Phys. Rev. Lett.*, 76(17), 1996.

[61] A. P. Fews, P. A. Norreys, F. N. Beg, A. R. Bell, A. E. Dangor, C. N. Danson, P. Lee, and S. J. Rose. Plasma ion emission from high intensity picosecond laser pulse interactions with solid targets. *Phys. Rev. Lett.*, 73(13), 1994.

[62] F. N. Beg, A. R. Bell, A. E. Dangor, C. N. Danson, A. P. Fews, M. E. Glinsky, B. A. Hammel, P. Lee, P. A. Norreys, and M. Tatarakis. A study of picosecond laser–solid interactions up to $10^{19}\,\mathrm{W\,cm^{-2}}$. *Phys. Plasmas*, 4(447), 1997.

[63] A. Maksimchuk, S. Gu, K. Flippo, and D. Umstadter. Forward ion acceleration in thin films driven by a high-intensity laser. *Phys. Rev. Lett.*, 84(18), 2000.

[64] M. Passoni, V. T. Tikhonchuk, M. Lontano, and V. Yu. Bychenkov. Charge separation effects in solid targets and ion acceleration with a two-temperature electron distribution. *Phys. Rev. E*, 69(026411), 2004.

[65] J. R. Davies, A. R. Bell, M. G. Haines, and S. M. Guérin. Short-pulse high-intensity laser-generated fast electron transport into thick solid targets. *Phys. Rev. E*, 59(6):7193, 1997.

[66] A. Henig, D. Kiefer, K. Markey, D. C. Gautier, K. A. Flippo, S. Letzring, R. P. Johnson, T. Shimada, L. Yin, B. J. Albright, K. J. Bowers, J. C. Fernández, S. G. Rykovanov, H.-C. Wu, M. Zepf, D. Jung, V. Kh. Liechtenstein, J. Schreiber, D. Habs, and B. M. Hegelich. Enhanced laser-driven ion acceleration in the relativistic transparency regime. *Phys. Rev. Lett.*, 103(045002), 2009.

[67] D. Batani, R. Jafer, M. Veltcheva, R. Dezulian, O. Lundh, F. Lindau, A. Persson, K. Osvay, C.-G. Wahlström, D. C. Carroll, P. McKenna, A. Flacco, and V. Malka. Effects of laser prepulses on laser-induced proton generation. *New J. Phys.*, 12(4):045018, 2010.

[68] A. J. Mackinnon, Y. Sentoku, P. K. Patel, D. W. Price, S. Hatchett, M. H. Key, C. Andersen, R. Snavely, and R. R. Freeman. Enhancement of proton acceleration by hot-electron recirculation in thin foils irradiated by ultraintense laser pulses. *Phys. Rev. Lett.*, 88(21), 2002.

[69] S. P. Hatchett, C. G. Brown, T. E. Cowan, E. A. Henry, J. S. Johnson, M. H. Key, J. A. Koch, A. B. Langdon, B. F. Lasinski, R. W. Lee, A. J. Mackinnon, D. M. Pennington, M. D. Perry, T. W. Phillips, M. Roth, T. C. Sangster, M. S. Singh, R. A. Snavely, M. A. Stoyer, S. C. Wilks, and K. Yasuike. Electron, photon and ion beams from the relativistic interaction of petawatt laser pulses with solid targets. *Phys. Plasmas*, 7(2076), 2000.

[70] J. Fuchs, P. Antici, E. d'Humières, E. Lefebvre, M. Borghesi, E. Brambrink, C. Cecchetti, T. Toncian, H. Pépin, and P. Audebert. Ion acceleration using high-contrast ultra-intense lasers. *J. Phys. IV France*, 133:1151–1153, 2006.

[71] J. Fuchs, P. Antici, E. d'Humières, E. Lefebvre, M. Borghesi, E. Brambrink, C. A. Cecchetti, M. Kaluza, V. Malka, M. Manclossi, S. Meyroneinc, P. Mora, J. Schreiber, T. Toncian, H. Pépin, and P. Audebert. Laser-driven proton scaling laws and new paths towards energy increase. *Nat. Phys.*, 2:48–54, 2006.

[72] J. Fuchs, J. C. Adam, F. Amiranoff, S. D. Baton, P. Gallant, L. Gremillet, A. H'eron, J. C. Kieffer, G. Laval, G. Malka, J. L. Miquel, P. Mora, H. Pépin, and C. Rousseaux. Transmission through highly overdense plasma slabs with a subpicosecond relativistic laser pulse. *Phys. Rev. Lett.*, 80(11), 1989.

[73] B. J. Albright, L. Yin, Kevin J. Bowers, B. M. Hegelich, K. A. Flippo, T. J. T. Kwan, and J. C. Fernández. Relativistic buneman instability in the laser breakout afterburner. *Phys. Plasmas*, 14(094502), 2007.

[74] L. Yin, B. J. Albright, K. J. Bowers, D. Jung, J. C. Fernández, and B. M. Hegelich. Three-dimensional dynamics of breakout afterburner ion acceleration using high-contrast short-pulse laser and nanoscale targets. *Phys. Rev. Lett.*, 107(045003), 2011.

[75] L. Yin, B. J. Albright, D. Jung, R. C. Shah, S. Palaniyappan, K. J. Bowers, A. Henig, J. C. Fernández, and B. M. Hegelich. Break-out afterburner ion acceleration in the longer laser pulse length regime. *Phys. Plasmas*, 18(063103), 2011.

[76] S. Steinke, A. Henig, M. Schnürer, T. Sokollik, P.V. Nickles, D. Jung, D. Kiefer, R. Hörlein, J. Schreiber, T. Tajima, X. Q. Yan, M. Hegelich, J. Meyer ter Vehn, W. Sandner, and D. Habs. Efficient ion acceleration by collective laser-driven electron dynamics with ultra-thin foil targets. *Laser Part. Beams*, 28(1):215–221, 2010.

[77] C.-K. Huang, B. J. Albright, L. Yin, H.-C. Wu, K. J. Bowers, B. M. Hegelich, and J. C. Fernández. Improving beam spectral and spatial quality by double-foil target in laser ion acceleration. *Phys. Rev. ST Accel. Beams*, 14(031301), 2011.

[78] C.-K. Huang, B. J. Albright, L. Yin, H.-C. Wu, K. J. Bowers, B. M. Hegelich, and J. C. Fernándes. A double-foil target for improving beam quality in laser ion acceleration with thin foils. *Phys. Plasmas*, 18(056707), 2011.

[79] B. M. Hegelich, I. Pomerantz, L. Yin, H.-C. Wu, D. Jung, B. J. Albright, D. C. Gautier, S. Letzring, S. Palaniyappan, R. Shah, K. Allinger, R. Hörlein, J. Schreiber, D. Habs, J. Blakeney, G. Dyer, L. Fuller, E. Gaul, E. Mccary, A. R. Meadows, C. Wang, T. Ditmire, and J. C. Fernández. Laser-driven ion acceleration from relativistically transparent nanotargets. *New J. Phys.*, 15(085015), 2013.

[80] F. Floux, D. Cognard, L-G. Denoeud, G. Piar, D. Parisot, J. L. Bobin, F. Delobeau, and C. Fauquignon. Nuclear fusion reactions in solid-deuterium laser-produced plasma. *Phys. Rev. A*, 1(3), 1970.

[81] N. Izumi, Y. Sentoku, H. Habara, K. Takahashi, F. Ohtani, T. Sonomoto, R. Kodama, T. Norimatsu, H. Fujita, Y. Kitagawa, K. Mima, K. A. Tanaka, and T. Yamanaka. Observation of neutron spectrum produced by fast deuterons via ultraintense laser plasma interactions. *Phys. Rev. E*, 65(036413), 2002.

[82] L. Disdier, J-P. Garçonnet, G. Malka, and J-L. Miquel. Fast neutron emission from a high-energy ion beam produced by a high-intensity subpicosecond laser pulse. *Phys. Rev. Lett*, 82(7), 1999.

[83] P. A. Norreys, A. P. Fews, F. N. Beg, A. R. Bell, A. E. Dangor, P. Lee, M. B. Nelson, H. Schmidt, M. Tatarakis, and M. D. Cable. Neutron production from picosecond laser irradiation of deuterated targets at intensities of 10^{19} Wcm^{-2}. *Plasma Phys. Control. Fusion*, 40:175–182, 1998.

[84] D. Hilscher, O. Berndt, M. Enke, U. Jahnke, P.V. Nickels, H. Ruhl, and W. Sandner. Neutron energy spectra from the laser-induced D(d,n)^{3}He reaction. *Phys. Rev. E*, 64(016414), 2001.

[85] J. Davis and G.M. Petrov. Angular distribution of neutrons from high-intensity laser–target interactions. *Plasma Phys. Control. Fusion*, 50(065016), 2008.

[86] G. M. Petrov, D. P. Higginson, J. Davis, Tz. B. Petrova, C. McGuffey, B. Qiao, and F. N. Beg. Generation of energetic (>15 MeV) neutron beams from proton- and deuteron-driven nuclear reactions using short pulse lasers. *Plasma Phys. Control. Fusion*, 55(105009), 2013.

[87] L. Willingale, G. M. Petrov, A. Maksimchuk, J. Davis, R. R. Freeman, A. S. Joglekar, T. Matsuoka, C. D. Murphy, V. M. Ovchinnikov, A. G. R. Thomas, L. Van Woerkom, and K. Krushelnick. Comparison of bulk and pitcher-catcher targets for laser-driven neutron production. *Phys. Plasmas*, 18(083106), 2011.

[88] T. Mayer-Kuckuck. *Kernphysik: Eine Einführung*. Teubner Verlag, 2002.

[89] J. J. Griffin. Statistical model of intermediate structure. *Phys. Rev. Lett.*, 17(9), 1966.

[90] M. Blann. Extensions of griffin's statistical model for medium-energy nuclear reactions. *Phys. Rev. Lett.*, 21(18), 1968.

[91] E. Gadioli and E. Gadioli Erba. Pre-equilibrium emission. *Nucl. Instrum. Methods*, 146:265–277, 1977.

[92] J. Randrup and R. Vandenbosch. Pre-equilibrium neutron emission in the nucleon exchange transport model. *Nucl. Phys. A*, 474:219–239, 1987.

[93] J. R. Oppenheimer and M. Phillips. Note on the transmutation function for deuterons. *Phys. Rev.*, 48(500), 1935.

[94] C. L. Fink, B. L. Cohen, J. C. van der Weerd, and R. J. Petty. Nemets effect in deuteron breakup by heavy nuclei. *Phys. Rev.*, 185(4), 1969.

[95] E. W. Hamburger, B. L. Cohen, and R. E. Price. Low-energy protons produced in the deuteron bombardment of nuclei. *Phys. Rev.*, 121(4), 1961.

[96] E. C. Mar, B. L. Cohen, and T. M. O'Keefe. Deuteron disintegration by Au, Rh, Cu, and C from 8 to 15 MeV. *Phys. Rev.*, 164(4), 1967.

[97] R. Serber. The production of high energy neutrons by stripping. *Phys. Rev.*, 72(11), 1947.

[98] T. Ye, Y. Watanabe, and K. Ogata. Analysis of deuteron breakup reactions on ^{7}Li for energies up to 100 MeV. *Phys. Rev. C*, 80(014604), 2009.

[99] B. V. Carlson, R. Capote, and M. Sin. Elastic and inelastic breakup of deuterons with energy below 100 MeV. 14th International Conference on Nuclear Reaction Mechanisms, 2015.

[100] W. Petry. Neutrns for industry. *EPJ Web Conf.*, 104(01001), 2015.

[101] NEA nuclear data base. http://www.oecd-nea.org/janisweb/index.html, access 2016.

[102] OECD NEA Data Bank. JANIS Books. `http://www.oecd-nea.org/janis/book/`, Access: 10/2016.

[103] D. P. Higginson, J. M. McNaney, D. C. Swift, G. M. Petrov, J. Davis, J. A. Frenje, L. C. Jarrott, R. Kodama, K. L. Lancaster, A. J. Mackinnon, H. Nakamura, P. K. Patel, G. Tynan, and F. N. Beg. Production of neutrons up to 18 MeV in high-intensity, short-pulse laser matter interactions. *Phys. Plasmas*, 18(100703), 2011.

[104] J. Davis, G. M. Petrov, Tz. Petrova, L. Willingale, A. Maksimchuk, and K. Krushelnick. Neutron production from ^{7}Li(d,xn) nuclear fusion reactions driven by high-intensity laser–target interactions. *Plasma Phys. Control. Fusion*, 52(045015), 2010.

[105] C. L. Lee and X.-L. Zhou. Thick target neutron yields for the ^{7}Li(p,n)^{7}Be reaction near threshold. *Nucl. Instr. Meth. Phys. Res. B*, 152:1–11, 1999.

[106] K. L. Lancaster, S. Karsch, H. Habara, F. N. Beg, E. L. Clark, R. Freeman, M. H. Key, J. A. King, R. Kodama, K. Krushelnick, K. W. D. Ledingham, P. McKenna, C. D. Murphy, P. A. Norreys, R. Stephens, C. Stöeckl, Y. Toyama, M. S. Wei, and M. Zepf. Characterization of ^{7}Li(p,n)^{7}Be neutron yields from laser produced ion beams for fast neutron radiography. *Phys. Plasmas*, 11(7), 2004.

[107] J. P. Meulders, P. Leleux, P. C. Macq, and C. Pirart. Fast neutron yields and spectra from targets of varying atomic number bombarded with deuterons from 16 to 50 MeV. *Phys. Med. Biol.*, 20(2):235–243, 1975.

[108] M. A. Lone. Intense fast neutron source reactions. In M.R. Bhat and S. Pearlstein, editors, *Symposium on neutron cross-sections from 10 to 40 MeV, BNL-NCS-50681*, pages 79–116. 1977.

[109] D. Jung, K. Falk, N. Guler, O. Deppert, M. Devlin, A. Favalli, J. C. Fernández, D. C. Gautier, M. Geissel, R. Haight, C. E. Hamilton, B. M. Hegelich, R. P. Johnson, F. Merrill, G. Schaumann, K. Schoenberg, M. Schollmeier, T. Shimada, T. Taddeucci, J. L. Tybo, S. A. Wender, C. H. Wilde, G. A. Wurden, and M. Roth. Characterization of a novel, short pulse laser-driven neutron source. *Phys. Plasmas*, 20(056706), 2013.

[110] G. M. Petrov, D. P. Higginson, J. Davis, Tz. B. Petrova, J. M. McNaney, C. McGuffey, B. Qiao, and F. N. Beg. Generation of high-energy (>15 MeV) neutrons using short pulse high intensity lasers. *Phys. Plasmas*, 19(093106), 2012.

[111] A. Maksimchuk, A. Raymond, F. Yu, G. M. Petrov, F. Dollar, L. Willingale, C. Zulick, J. Davis, and K. Krushelnick. Dominant deuteron acceleration with a high-intensity laser for isotope production and neutron generation. *Appl. Phys. Lett.*, 102(191117), 2013.

[112] C. Zulick, F. Dollar, V. Chvykov, J. Davis, G. Kalinchenko, A. Maksimchuk, G. M. Petrov, A. Raymond, A. G. R. Thomas, L. Willingale, V. Yanovsky, and K. Krushelnick. Energetic neutron beams generated from femtosecond laser plasma interactions. *Appl. Phys. Lett.*, 102(124101), 2013.

[113] J. M. Yang, P. McKenna, K. W. D. Ledingham, T. McCanny, L. Robson, S. Shimizu, R. P. Singhal, M. S. Wei, K. Krushelnick, R. J. Clarke, D. Neely, and P. A. Norreys. Neutron production by fast protons from ultraintense laser-plasma interactions. *J. Appl. Phys.*, 96(11), 2004.

[114] D. P. Higginson, J. M. McNaney, D. C. Swift, T. Bartal, D. S. Hey, R. Kodama, S. Le Pape, A. Mackinnon, D. Mariscal, H. Nakamura, N. Nakanii, K. A. Tanaka, and F. N. Beg. Laser generated neutron source for neutron resonance spectroscopy. *Phys. Plasmas*, 17(100701), 2010.

[115] C. L. Ellison and J. Fuchs. Optimizing laser-accelerated ion beams for a collimated neutron source. *Phys. Plasmas*, 17(113105), 2010.

[116] T. Toncian, M. Borghesi, J. Fuchs, E. D'Humiéres, P. Antici, P. Audebert, E. Brambrink, C. A. Cecchetti, A. Pipahl, L. Romagnani, and O. Willi. Ultrafast Laser-Driven Microlens to Focus and Energy-Select Mega-Electron Volt Protons. *Science*, 312:410, 2006.

[117] G. A. Mourou, C. L. Labaune, M. Dunne, N. Naumova, and V. T. Tikhonchuk. Relativistic laser-matter interaction: from attosecond pulse generation to fast ignition. *Plasma Phys. Control. Fusion*, 49:B667–B675, 2007.

[118] W. M. Stacey. *Fusion Plasma Physics*. WILEY-VCH Verlag GmbH &Co. KGaA, Weinheim, 2005.

[119] W. M. Stacey. *Fusion: an introduction to the physics and technology of magnetic confinement fusion*. WILEY-VCH Verlag GmbH &Co. KGaA, Weinheim, 2010.

[120] J. Nuckolls, L. Wood, A. Thiessen, and G. Zimmerman. Laser Compression of Matter to Super-High Densities: Thermonuclear (CTR) Applications. *Nature*, 239:139–142, 1972.

[121] R. Betti and O. A. Hurricane. Inertial-confinement fusion with lasers. *Nat. Phys.*, 12:435–448, 2016.

[122] M. Tabak, J. Hammer, M. E. Glinsky, W. L. Kruer, S. C. Wilks, J. Woodworth, E. M. Campbell, M. D. Perry, and R. J. Mason. Ignition and high gain with ultrapowerful lasers. *Phys. Plasmas*, 1(1626), 1994.

[123] M. Roth, T. E. Cowan, M. H. Key, S. P. Hatchett, C. Brown, W. Fountain, J. Johnson, D. M. Pennington, R. A. Snavely, S. C. Wilks, K. Yasuike, H. Ruhl, F. Pegoraro, S.V. Bulanov, E. M. Campbell, M. D. Perry, and H. Powell. Fast Ignition by Intense Laser-Accelerated Proton Beams. *Phys. Rev. Lett.*, 86(2), 2001.

[124] J. M. Carpenter and C.-K. Loong. *Elements of slow-neutron scattering: Basics, Techniques and Applications*. Cambridge University Press, 2015.

[125] B. Blau, K. N. Clausen, S. Gvasaliya, M. Janoschek, S. Janssen, L. Keller, B. Roessli, J. Schefer, P. Tregenna-Piggott, W. Wagner, and O. Zaharko. The Swiss Spallation Neutron Source SINQ at Paul Scherrer Institut. *Neutron News*, 20(3):5–8, 2009.

[126] V. W. Yuan, J. David Bowman, D. J. Funk, G. L. Morgan, R. L. Rabie, C. E. Ragan, J. P. Quintana, and H. L. Stacy. Shock Temperature Measurement Using Neutron Resonance Spectroscopy. *Phys. Rev. Lett.*, 94(125504), 2005.

[127] A. Benuzzi-Mounaix, M. Koenig, G. Huser, B. Faral, D. Batani, E. Henry, M. Tomasini, B. Marchet, T. A. Hall, M. Boustie, Th. De Rességuier, M. Hallouin, F. Guyot, D. Andrault, and Th. Charpin. Absolute equation of state measurements of iron using laser driven shocks. *Phys. Plasmas*, 9(2466), 2002.

[128] D. Batani, H. Stabile, A. Ravasio, G. Lucchini, F. Strati, T. Desai, J. Ullschmied, E. Krousky, J. Skala, L. Juha, B. Kralikova, M. Pfeifer, Ch. Kadlec, T. Mocek, A. Präg, H. Nishimura, and Y. Ochi. Ablation pressure scaling at short laser wavelength. *Phys. Rev. E*, 68(067403), 2003.

[129] D. Kraus, A. Ravasio, M. Gauthier, D. O. Gericke, J. Vorberger, S. Frydrych, J. Helfrich, L. B. Fletcher, G. Schaumann, B. Nagler, B. Barbrel, B. Bachmann, E. J. Gamboa, S. Göde, E. Granados, G. Gregori, H. J. Lee, P. Neumayer, W. Schumaker, T. Döppner, R. W. Falcone, S. H. Glenzer, and M. Roth. Nanosecond formation of diamond and lonsdaleite by shock compression of graphite. *Nat. Commun.*, 7(10970), 2016.

[130] D. L. Smith, R. G. Clemmer, S. D. Harkness, J. Jung, J. L. Krazinski, R. F. Mattas, H. C. Stevens, C. K. Youngdahl, C. Trachsel, D. Bowers, B. Cramer, J. Davis, G. Fuller, and D. Morgan. Fusion reactor blanket/shield design study. ANL/FPP-79-1, 1979.

[131] J. Alvarez, J. Fernández-Tobiasa, K. Mimaa, S. Nakaib, S. Karc, Y. Katob, and J. M. Perladoa. Laser driven neutron sources: Characteristics, applications and prospects. *Physics Procedia*, 60:29–38, 2014.

[132] D. C. Cutforth. Neutron Sources for Radiography and Gaging. In H. Berger, editor, *Practical Applications of Neutron Radiography and Gaging*. American Society for Testing and Materials, 1976.

[133] J. I. W. Watterson and R. M. Ambrosi. Some fundamental considerations in resonance imaging using fast neutrons. *Nucl. Instr. Meth. Phys. Res. A*, 513:367–373, 2003.

[134] S. Nakai, K. Mima, Y. Kato, K. Tanaka, Y. Ikeda, H. Azechi, K. Miyanaga, M. Nakai, M. Perlado, and R. Gonzalez Arrabal. Industrial Applications of Laser Neutron Source. *J. Phys. Conf. Ser.*, 244(042027), 2010.

[135] V. V. Balashov. *Interaction of Particles and Radiation with Matter*. Springer-Verlag Berlin Heidelberg, 1997.

[136] D. J. Griffiths. *Quantenmechanik: Lehr- und Übungsbuch*. Pearson Deutschland, second edition, 2012.

[137] G. Muhrer. Urban legends of thermal moderator design. *Nucl. Instr. Meth. Phys. Res. A*, 664:38–47, 2012.

[138] V. Skoy, Y. S. Lee, H. S. Kang, M.-H. Cho, I. S. Ko, and W. Namkung. Measurement of Total Cross-Sections of Natural In and Cu at the Pohang Neutron Facility. *J. Korean Phys. Soc.*, 41(3):314–321, 2002.

[139] G. Breit and E. Wigner. Capture of slow neutrons. *Phys. Rev.*, 49:519, 1936.

[140] P. Reuss. *Neutron Physics*. EDP Sciences, 2008.

[141] F. Gunsing. Neutron Resonance Spectroscopy, postdoctoral lecture qualification Université Paris, 2005.

[142] W. E. Lamb. Capture of Neutrons by Atoms in a Crystal. *Phys. Rev.*, 55:190–197, 1939.

[143] J. A. Harvey, editor. *Experimental Neutron Resonance Spectroscopy*. Academic Press New York and London, 1970.

[144] C. E. Ragan III, M. G. Silbert, and B. C. Diven. Shock compression of molybdenum to 2.0 TPa by means of a nuclear explosion. *J. Appl. Phys.*, 48:2860, 1977.

[145] H. J. Stone, M. G. Tucker, Y. Le Godec, F. N. Méducin, E. R. Cope, S. A. Hayward, G. P. J. Ferlat, W. G. Marshall, S. Manololpulos, S. A. T. Redfern, and M. T. Dove. Remote determination of sample temperature by neutron resonance spectroscopy. *Nucl. Instr. Meth. Phys. Res. A*, 547:601–615, 2005.

[146] A. S. Tremsin, S. C. Vogel, M. Mocko, M. A. M. Bourke, V. Yuan, R. O. Nelson, D. W. Brown, and W. B. Feller. Non-destructive studies of fuel pellets by neutron resonance absorption radiography and thermal neutron radiography. *J. Nucl. Mater.*, 440(633), 2013.

[147] F. Gunsing, A. Leprêtre, C. Mounier, and C. Raepsaet. Neutron resonance spectroscopy of ^{99}Tc from 3 ev to 150 kev. *Phys. Rev. C*, 61(054608), 2000.

[148] Yi-Fen Yen, J. D. Bowman, R. D. Bolton, B. E. Crawford, P. P. J. Delheij, G. W. Hart, T. Haseyama, C. M. Frankle, M. Iinuma, J. N. Knudson, A. Masaike, Y. Masuda, Y. Matsuda, G. E. Mitchell, S. I. Penttilä, N. R. Roberson, S. J. Seestrom, E. Sharapov, H. M. Shimizu, D. A. Smith, S. L. Stephenson, J. J. Szymanski, S. H. Yoo, and V. W. Yuan. A high-rate ^{10}B-loaded liquid scintillation detector for parity-violation studies in neutron resonances. *Nucl. Instr. Meth. Phys. Res. A*, 447:476–489, 2000.

[149] G. F. Knoll. *Radiation detection and measurement*. John Wiley & Sons, Inc., third edition, 2000.

[150] ENDF data base. https://www-nds.iaea.org/exfor/endf.htm, access: 02/2017.

[151] R. H. Olsher, T. D. McLean, M. W. Mallett, L. L. Romero, R. T. Devine, and J. M. Hoffmann. High-energy response of passive dosemeters in use at LANL. *Radiat. Prot. Dosim.*, 126:326–332, 2007.

[152] F. Smecka and M. Hajek. Neutronendosimetrie mit Bubbledetektoren, 2007. AIAU 27607.

[153] F. Seitz. On the Theory of the Bubble Chamber. *Phys. Fluids*, 1(1):2–13, 1958.

[154] R. E. Apfel. The superheated drop detector. *Nucl. Instrum. Meth.*, 162:603–608, 1979.

[155] BTI. Bubble Technology Industries, http://www.bubbletech.ca, access 2015.

[156] W. R. Leo. *Techniques for Nuclear and Particle Physics Experiments*. Springer Verlag, second edition, 1994.

[157] K. Kleinknecht. *Detektoren für Teilchenstrahlung*. Teubner Verlag, fourth edition, 2005.

[158] C. Grupen and B. Shwartz. *Particle Detectors*. Cambridge University Press, second edition, 2008.

[159] Photomultiplier Tubes Catalogue Photonis.
https://hallcweb.jlab.org/DocDB/0008/000809/001/PhotonisCatalog.pdf,
access: 2016.

[160] Hamamatsu, Photomultiplier tube R1250.
https://www.hamamatsu.com/eu/en/R1250.html, access: 2016.

[161] S. Aumüller. Untersuchung von Szintillatoren auf Zeitauflösung und deren Einsatz als Teilchendetektoren. Bachelor's Thesis, Technische Universität Darmstadt, 2016.

[162] J. L. Wiza. Microchannel plate detectors. *Nucl. Instrum. Methods*, 162:587, 1979.

[163] A. S. Tremsin, W. B. Feller, and R. G. Downing. Efficiency optimization of microchannel plate (MCP) neutron imaging detectors. I. Square channels with ^{10}B doping. *Nucl. Instr. Meth. Phys. Res. A*, 593:278, 2005.

[164] P. B. Price R. L. Fleischer and R. M. Walker. Track Registration in Various Solid-State Nuclear Track Detectors. *Phys. Rev.*, 133(5A):A1443, 1964.

[165] H. B. Lück. Energy spectrometry of protons by means of a dielectric track detector. *Nucl. Instrum. Meth.*, 11:403–404, 1974.

[166] F. Wagner, C. Brabetz, O. Deppert, M. Roth, T. Stöhlker, An. Tauschwitz, A. Tebartz, B. Zielbauer, and V. Bagnoud. Accelerating ions with high-energy short laser pulse from submicrometer thick targets. *High Power Laser Sci. Eng.*, 4(e45), 2016.

[167] F. Nürnberg, M. Schollmeier, E. Brambrink, A. Blažević, D. C. Carroll, K. Flippo, D. C. Gautier, M. Geißel, K. Harres, B. M. Hegelich, O. Lundh, K. Markey, P. McKenna, D. Neely, J. Schreiber, and M. Roth. Radiochromic film imaging spectroscopy of laser-accelerated proton beams. *Rev. Sci. Instrum.*, 80(3), 2009. 033301.

[168] D. E. González Trotter, F. Salinas Meneses, W. Tornow, A. S. Crowell, C. R. Howell, D. Schmidt, and R. L. Walter. Neutron detection efficiency determinations for the TUNL neutron-neutron and neutron-proton scattering length measurements. *Nucl. Instum. Meth. Phys. Res. A*, 599:234–242, 2009.

[169] A. Tebartz, S. Bedacht, G. Schaumann, and M. Roth. Fabrication and characterization of thin polymer targets for laser-driven ion acceleration. *J. Phys.: Conf. Ser.*, 713(012005), 2016.

[170] A. Tebartz. Entwicklung von dünnen Polymerfolien zur Laser-Ionenbeschleunigung an PHELIX. Master's thesis, Technische Universität Darmstadt, 2014.

[171] J. Hornung. Herstellung und Charakterisierung von deuterierten Kunststofftargets zur Neutronenerzeugung mit Kurzpulslasern. Bachelor's Thesis, Technische Universität Darmstadt, 2015.

[172] F. Wagner, S. Bedacht, V. Bagnoud, O. Deppert, S. Geschwind, R. Jaeger, A. Ortner, A. Tebartz, B. Zielbauer, D. H. H. Hoffmann, and M. Roth. Simultaneous observation of angularly separated laser-driven proton beams accelerated via two different mechanisms. *Phys. Plasmas*, 22(063110), 2015.

[173] M. M. Guenther, A. Britz, R.J. Clarke, K. Harres, G. Hoffmeister, F. Nürnberg, A. Otten, A. Pelka, M. Roth, and K. Vogt. Nais: Nuclear acivation-based imaging spectroscopy. *Rev. Sci. Instrum.*, 84(073305), 2013.

[174] W. Demtröder. *Experimenttalphysik 4: Kern-, Teilchen- und Astrophysik*. Springer Verlag Berlin Heidelberg, fourth edition, 2014.

[175] J. Schreiber. *Ion Acceleration driven by High-Intensity Laser Pulses*. PhD thesis, Ludwig-Maximilians-Universität München, 2006.

[176] Oliver Merle. personal conversation, 2016.

[177] B. D. McDaniel. Slow Neutron Resonance in Indium. *Phys. Rev.*, 70:832–841, 1946.

[178] Nova Scientific. http://www.novascientific.com/, access: 03/2017.

[179] A. Tartaglione, J. J. Blosteinand, and R .E. Mayer. Prompt gamma emissions in the reaction ^{115}In(n,γ)^{116}In for neutrons around the 1.45 eV absorption resonance. *Appl. Radiat. Isot.*, 67:1711–1715, 2009.

[180] ProxiVision GmbH. http://www.proxivision.de/, access: 01/2017.

[181] C. A. Ekdahl. Neutron diagnostics for pulsed high density thermonuclear plasmas. *Rev. Sci. Instrum.*, 50(941), 1979.

[182] A. Ferrari, P. R. Sala, A. Fasso, and J. Ranft. FLUKA: a multi-particle transport code. CERN-2005-10, INFN/TC_05/11, SLAC-R-773, 2005.

[183] T. T. Böhlen, M. P. W. Chin F. Cerutti, A. Fasso, A. Ferrari, P. G. Ortega, A. Mairani, P. R. Sala, G. Smirnov, and V. Vlachoudis. The FLUKA Code: Developments and Challenges for High Energy and Medical Applications. *Nucl. Data Sheets*, 120:211–214, 2014.

[184] S. Agostinelli *et al.* GEANT4 - a simulation toolkit. *Nucl. Instr. Meth. Phys. A*, 506(3):250–303, 2003.

[185] Nuclear Enterprises Scintillators. https://wwwusers.ts.infn.it/~rui/univ/Acquisizione_Dati/Manuals/NuclearEnterprisesScintillators.pdf, access: 04/2017.

[186] P. G. Sjölin. The scintillation decay of some commercial organic scintillators. *Nucl. Instrum. Methods*, 37:45–50, 1965.

[187] T. M. Kelly, J. A. Merrigan, and R. M. Lambrecht. Comparison of plastic scintillators with nanosecond lifetimes. *Nucl. Instrum. Methods*, 109:233–235, 1973.

[188] Saint Gobain Crystals. http://www.crystals.saint-gobain.com/, access 03/2017.

[189] S. Keppler, A. Sävert, J. Körner, M. Hornung, H. Liebetrau, J. Hein, and M. C. Kaluza. The generation of amplified spontaneous emission in high-power CPA laser sytsems. *Laser Photonics Rev.*, 10(2):264–277, 2016.

[190] N. V. Didenko, A. V. Konyashchenko, A. P. Lutsenko, and S. Yu. Tenyakov. Contrast degradation in a chirped-pulse amplifier due to generation of prepulses by postpulses. *Opt. Express*, 16(5), 2008.

[191] V. A. Schanz, F. Wagner, M. Roth, and V. Bagnoud. Noise reduction in third order cross-correlation by angle optimization of the interacting beams. *Opt. Express*, 25(8), 2017.

[192] F. Wagner, C.P. Jo*ã*o, J. Fils, T. Gottschall, J. Hein, J. Körner, J. Limpert, M. Roth, T. Stöhlker, and V. Bagnoud. Temporal contrast control at the PHELIX petawatt laser facility by means of tunable sub-picosecond optical parametric amplification. *Appl. Phys. B*, 116:429–435, 2014.

[193] A. Monmayrant, S. Weber, and B. Chatel. A newcomer's guide to ultrashort pulse shaping and characterization. *J. Phys. B*, 43(103001), 2010.

[194] T. Zh. Esirkepov, J. K. Koga, A. Sunahara, T. Morita, M. Nishikino, K. Kageyama, H. Nagatomo, K. Nishihara, A. Sagisaka, H. Kotaki, T. Nakamura, Y. Fukuda, H. Okada, A. S. Pirozhkov, A. Yogo, M. Nishiuchi amd H. Kiriyama, K. Kondo, M. Kando, and S. V. Bulanov. Prepulse and amplified spontaneous emission effects on the interaction of a petawatt class laser with thin solid targets. *Nucl. Instr. Meth. Phys. Res. A*, 745:150–163, 2014.

List of Abbreviations

BOA	Break-Out Afterburner
B-PE	Boron-treated Polyethylene
CM	Center of Mass
CPA	Chirped Pulse Amplification
EMP	Electromagnetic Pulse
FNR	Fast Neutron Radiography
FWHM	Full Width Half Maximum
GSI	GSI Helmholtzzentrum für Schwerionenforschung GmbH
HDPE	High Density Polyethylene
LANL	Los Alamos National Laboratory
LBNL	Lawrence Berkeley National Laboratory
MCP	Microchannel Plate
NAIS	Nuclear Activation-based Imaging Spectroscopy
NM	New Mexico
NRS	Neutron Resonance Spectroscopy
nToF	neutron Time of Flight
PIC	Particle in Cell
PMT	Photomultiplier Tube
RCF	Radiochromic Film
TA North	Target Area North
TNSA	Target Normal Sheath Acceleration
ToF	Time of Flight

List of Figures

List of Tables

List of Publications

- A. Alejo and A. G. Krygier and H. Ahmed and J. T. Morrison and R. J. Clarke and J. Fuchs and A. Green and J. S. Green and D. Jung and **A. Kleinschmidt** and Z. Najmudin and H. Nakamura and P. Norreys and M. Notley and M. Oliver and M. Roth and L. Vassura and M. Zepf and M. Borghesi and R. R. Freeman and S. Kar. High flux, beamed neutron source using deuteron-rich ion beams from D_2O-ice layered targets. *Plasma Phys. Control. Fusion*, 59(6), 2017
- F. Wagner and O. Deppert and C. Brabetz and P. Fiala and **A. Kleinschmidt** and P. Poth and V. A. Schanz and A. Tebartz and B. Zielbauer and M. Roth and T. Stöhlker and V. Bagnoud. Maximum proton energy above 85 MeV from relativistic interaction of laser pulses with micrometer thick CH_2 targets. *Phys. Rev. Lett.*, 116(205002), 2016
- A. G. Krygier and J. T. Morrison and S. Kar and H. Ahmed and A. Alejo and R. Clarke and J. Fuchs and A. Green and D. Jung and **A. Kleinschmidt** and Z. Najmudin and H. Nakamura and P. Norreys and M. Notley and M. Oliver and M. Roth and L. Vassura and M. Zepf and M. Borghesi and R. R. Freeman. Selective deuterium ion acceleration using the Vulcan petawatt laser. *Phys. Plasmas*, 22(053102), 2015
- S. R. Mirfayzi and S. Kar and H. Ahmed and A. G. Krygier and A. Green and A. Alejo and R. Clarke and R. R. Freeman and J. Fuchs and D. Jung and **A. Kleinschmidt** and J. T. Morrison and Z. Najmudin and H. Nakamura and P. Norreys and M. Oliver and M. Roth and L. Vassura and M. Zepf and M. Borghesi. Calibration of time of flight detectors using laser-driven neutron source. *Rev. Sci. Instrum*, 86(073308), 2015
- A. Alejo and S. Kar and H. Ahmed and A. G. Krygier and R. Clarke and R. R. Freeman and J. Fuchs and A. Green and J. S. Green and D. Jung and **A. Kleinschmidt** and J. T. Morrison and Z. Najmudin and H. Nakamura and P. Norreys and M. Notley and M. Oliver and M. Roth and L. Vassura and M. Zepf and M. Borghesi. Generation of High-Flux Neutron Beam from Radiation Pressure driven Deuterium Ion Bunches. *Proceedings of the 42nd European Physical Society Conference on Plasma Physics, EPS*, 2015
- I. Engin and M. Büscher and O. Deppert and L. Di Lucchio and R. Engels and S. Frydrych and P. Gibbon and **A. Kleinschmidt** and A. Lehrach and M. Roth and F. Schlüter and K. Strathmann and F. Wagner. Towards a Laser-driven polarized ^{3}He Ion–Beam Source. *PoS*, PSTP2015(002), 2015

- A. Alejo and S. Kar and H. Ahmed and A. G. Krygier and D. Doria and R. Clarke and J. Fernandez and R. R. Freeman and J. Fuchs and A. Green and J. S. Green and D. Jung and **A. Kleinschmidt** and C. L. S. Lewis and J. T. Morrison and Z. Najmudin and H. Nakamura and G. Nersisyan and P. Norreys and M. Notley and M. Oliver and M. Roth and J. A. Ruiz and L. Vassura and M. Zepf and M. Borghesi. Characterisation of deuterium spectra from laser driven multi-species sources by employing differentially filtered image plate detectors in Thomson spectrometers. *Rev. Sci. Instrum.*, 85(093303), 2014

First-author non-reviewed publications

- **A. Kleinschmidt** and V. Bagnoud and O. Deppert and A. Favalli and S. Frydrych ans J. Hornung and D. Jahn and G. Schaumann and A. Tebartz and F. Wagner and G. Wurden and M. Roth. A laser-driven neutron source at PHELIX. In *GSI Scientific Report 2015*
- **A. Kleinschmidt** and A. Favalli and J. Hornung and A. Tebartz and G. Wurden and V. A. Schanz and M. Roth. Resonance spectroscopy with a laser-driven neutron source. Submitted to *GSI Scientific Report 2016*

Talks

- 37th International Workshop on High Energy Density Physics with Intense Ion and Laser Beams, Hirschegg, Austria, Feb 2017
- 34th European Conference on Laser Interaction with Matter (ECLIM), Moscow, Russia, Sep 2016
- 36th International Workshop on High Energy Density Physics with Intense Ion and Laser Beams, Hirschegg, Austria, Feb 2016

Curriculum vitae

Personal data

Name	Annika Kleinschmidt
Date, place of birth	26.10.1989, Erfurt
Nationality	German

Education

Oct 2011 - Mar 2014	Technische Universität Darmstadt M.Sc. in Physics, Ø1.7 Master's thesis: Spatial characterization of a laser driven neutron source
Oct 2008 - Sep 2011	Universität Potsdam B.Sc. in Physics, Ø2.0 Bachelor's thesis: Distribution of cosmic ray sources in the galaxy
Sep 2000 - Jul 2008	Edith-Stein-Gymnasium Erfurt Abitur, Ø2.0

Professional experience

Aug 2013 - Jul 2016	participation in eleven experimental campaigns, thereof three as experiment coordinator and four abroad
Oct 2010 - Jun 2016	tutor for the physical laboratory training (Grundpraktikum) at Universität Potsdam and Technische Universität Darmstadt

Awards

Feb 2017	Young Scientist Prize of Laser and Particle Beams for "Moderation of neutrons generated by a laser-driven neutron source"